



PADERBORN UNIVERSITY
The University for the Information Society

Nonlinear optical properties in structured plasmonic nanomaterials and their application in hybrid metasurfaces

Dissertation zur Erlangung des akademischen Titels

doctor rerum naturalium

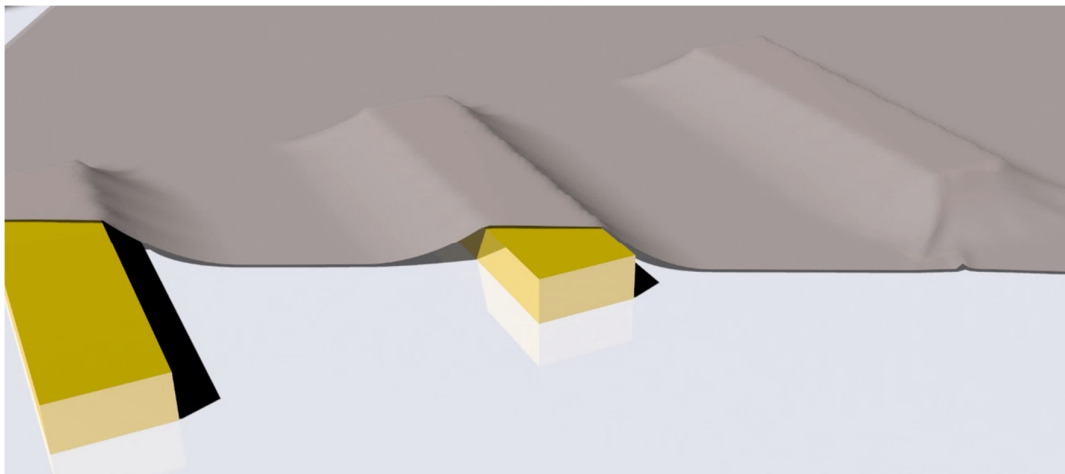
(Dr. rer. nat.)

vorgelegt

der Fakultät für Naturwissenschaften der Universität Paderborn

von M. Sc. Florian Spreyer

Dezember 2021



ERKLÄRUNG DER SELBSTSTÄNDIGKEIT

Ich versichere hiermit an Eides statt, dass ich die vorliegende Arbeit mit dem Titel „Nonlinear optical properties in structured plasmonic nanomaterials and their application in hybrid metasurfaces“ selbstständig und ohne unzulässige fremde Hilfe erbracht habe. Ich habe keine anderen als die angegebenen Quellen und Hilfsmittel benutzt sowie wörtliche und sinngemäße Zitate kenntlich gemacht. Die Arbeit hat in gleicher oder ähnlicher Form noch keiner Prüfungsbehörde vorgelegen.

Paderborn, den

Florian Spreyer

ABSTRACT

The presented work investigates the second-harmonic generation (SHG) arising from hybrid metasurfaces consisting of metallic nanoantenna arrays and a two-dimensional layer of WS_2 for near-infrared excitation wavelengths and illustrates the potential for tailored nonlinear optical applications.

In a fundamental study, the influence of several parameters on the SHG in hybrid metasurfaces is investigated. Therefore, metallic nanoantenna arrays are fabricated by electron-beam lithography onto a bare glass substrate, where a mechanically exfoliated monolayer of WS_2 is transferred on top of them subsequently. The experimental investigations on these hybrid metasurfaces are performed by optical spectroscopy techniques and are done in the linear and nonlinear regime. The experimental results lead to a simplified model describing the coupling between metallic nanoantennas and a monolayer WS_2 for the process of SHG.

This coupling is further utilized to implement a phase modulation induced by the plasmonic nanoantenna array. Hereby, the fabrication process is reversed and the metallic nanoantennas are fabricated onto monolayers of WS_2 , which were fabricated by chemical vapor deposition and transferred onto a glass substrate in the first place. Linear optical characterizations prove, that the monolayer WS_2 remains intact. It is shown, that the nonlinear response can be tailored by a local phase change induced by changing the relative rotation angle of the individual metallic nanoantennas.

KURZFASSUNG

Die vorliegende Arbeit untersucht die Erzeugung der zweiten Harmonischen in hybriden Metaoberflächen, die aus metallischen Nanoantennenarrays und einer zweidimensionalen WS_2 -Schicht bestehen und zeigt dabei das Potenzial für maßgeschneiderte nichtlineare optische Anwendungen auf.

In einer Grundlagenstudie wird der Einfluss verschiedener Parameter auf die Erzeugung der zweiten Harmonischen in hybriden Metaoberflächen untersucht. Dazu werden metallische Nanoantennenarrays mittels Elektronenstrahlolithographie auf einem Glassubstrat hergestellt, auf die anschließend eine exfolierte Monolage WS_2 transferiert wird. Die experimentellen Untersuchungen dieser hybriden Metaoberflächen werden mit optischen Spektroskopieverfahren durchgeführt. Auf Basis experimentellen Ergebnisse wird ein vereinfachtes Modell vorgestellt, das die Kopplung zwischen metallischen Nanoantennen und einer WS_2 -Monolage beschreibt.

Diese Kopplung wird daraufhin ausgenutzt, um eine Phasenmodulation zu realisieren. Dabei wird der Herstellungsprozess umgekehrt, sodass die metallischen Nanoantennen auf WS_2 -Monolagen hergestellt werden, die zuvor durch chemische Gasphasenabscheidung auf ein Glassubstrat transferiert wurden. Anschließende optische Charakterisierungen zeigen, dass die WS_2 -Monolagen unbeschädigt bleiben. Es wird gezeigt, dass die Erzeugung der zweiten Harmonischen durch eine lokale Phasenänderung, die durch Änderung des relativen Drehwinkels der einzelnen metallischen Nanoantennen induziert wird, maßgeschneidert werden kann.

CONTENT

Erklärung der Selbstständigkeit.....	i
Abstract.....	iii
Kurzfassung	v
Content	vii
1. Introduction	1
2. Fundamental Theory	5
2.1. Optical properties of gold	5
2.1.1. Dielectric function of gold.....	5
2.1.2. Localized surface plasmon polaritons	8
2.1.3. Near-field enhancement of plasmonic nanostructures	11
2.2. Nonlinear plasmonics.....	15
2.2.1. Harmonic generation in general	15
2.2.2. Harmonic generation in plasmonics.....	19
2.3. Monolayer WS ₂ – transition metal dichalcogenides	20
2.3.1. Fabrication of 1L-WS ₂	21
2.3.2. Band and lattice structure of WS ₂	23
2.4. Optical properties of 1L-WS ₂	25
2.4.1. Photoluminescence in 1L-WS ₂	26
2.4.2. Second-harmonic generation in 1L-WS ₂	28
3. Influence of plasmon resonances on SHG in hybrid metasurfaces	33
3.1. SHG in hybrid metasurfaces	34
3.2. Fabrication process	35

3.3.	Polarization-dependent SHG in hybrid metasurfaces	37
3.3.1.	Design concept.....	37
3.3.2.	Linear optical characterization	38
3.3.3.	Nonlinear optical characterization	41
3.3.4.	Symmetry effects on nonlinear harmonic generation.....	43
3.3.5.	Linear polarization dependency	47
3.3.6.	Modeling the SHG of hybrid metasurfaces	49
3.3.7.	Enhanced second-harmonic generation	53
3.4.	Tuning the plasmon resonances	54
3.5.	Impact of different symmetries	58
3.6.	Conclusion.....	62
4.	Phase modulation in hybrid metasurfaces	63
4.1.	The Pancharatnam-Berry phase.....	64
4.2.	Fabrication process	67
4.3.	Linear optical characterization.....	68
4.4.	Nonlinear optical imaging.....	71
4.4.1.	Visualization of optical selection rules for SHG	72
4.4.2.	Wavelength dependency.....	75
4.4.3.	Power dependency	77
4.5.	Spatial phase modulation	80
4.6.	Hologram encoded in hybrid metasurfaces	83
4.6.1.	Pancharatnam-Berry phase in nonlinear harmonic generation.	83
4.6.2.	Fresnel-approximation of diffraction.....	86
4.6.3.	Computer-generated holograms	89
4.6.4.	Theoretical reconstruction of holographic images.....	93
4.6.5.	Linear optical characterization	94
4.6.6.	Experimental reconstruction of holographic images.....	95
4.7.	Conclusion.....	98
5.	Summary and Outlook	101
6.	References.....	105
	Appendix.....	115
	Acknowledgements.....	119

1.INTRODUCTION

Similar to the downsizing of transistors in computer chips, the field of photonics is dedicated to reducing the size of optical elements, which can manipulate light on small scales. In conventional optics, light is controlled by bulky optical elements, which are much larger than the scale of a wavelength, such as lenses, mirrors, filters, polarizers, wave plates and many more. The manipulation of light in such optics is based on the interaction of matter with the light on a scale of up to several millimeters. Although the optical properties of such optical elements are well-known and led to a rigorous implementation in countless optical setups, their large dimensions make them not suitable for the deployment in tailoring light on subwavelength scales. In contrast to bulky optical elements, so-called metamaterials make use of the progress made in nanofabrication in the last decades in order to manipulate light in miniaturized photonic devices.

Metasurfaces are a quasi-two-dimensional type of metamaterials that consist of arrays of nanostructures with an individual size smaller than the wavelength of light. These planar surfaces open up the possibility to shape incident light on scales two orders of magnitude below its wavelength. Nowadays, researchers around the globe report countless designs for these very thin metasurfaces for a variety of applications, e.g. mimicking a conventional lens, beam-shaping and holography [1-3]. This great number of applications makes them highly attractive while maintaining a manageable complex manufacturing process, which can be even expanded to great sizes and numbers cost-efficiently [4]. The high flexibility of metasurfaces arises from their individual nanostructures, which can be designed freely, to match them to different light properties, e.g. a certain wavelength range or polarization state [5, 6]. Compared to classical bulky optical elements, where the light manipulation is achieved along the optical path of the light through the medium, metasurfaces abruptly induce changes in the electromagnetic properties in the scale of several nanometers.

Besides the possibility to manipulate light on subwavelength scale, additional properties increase the value of metasurfaces as optical elements based on the material they are made of. In general, they can be classified into two distinct categories, either metallic or dielectric materials. While dielectric metasurfaces manipulate light on scales close to the wavelength of the visible light, metallic metasurfaces are even thinner. A sufficient light-matter interaction can be maintained down to a fraction of the excitation wavelength due to their large scattering cross-section. In the past decades, many applications for plasmonic metasurfaces were reported, where they are utilized for different tasks. While some of these tasks try to copy the functionality of conventional bulky elements, such as achromatic lenses or broadband wave plates [7, 8], others introduce a complex phase manipulation to the light to implement a beam deflection or the encoding of high efficient and broadband holographic images [9-12]. Although metallic metasurfaces provide a high light-matter interaction, one drawback is their limited polarization conversion efficiency, which is part of the phase modulation many applications rely on. However, recent research tries to solve this problem with the help of new designs [13].

The high flexibility and large scattering cross-section of metallic metasurfaces is also utilized in the research field of nonlinear optics. In this field, the generation of higher harmonic orders, such as second- and third-harmonic generation, leads to the emission of photons with an energy equal to the energy of two or more photons. Although metal plasmonic metasurfaces can provide a nonlinear response by themselves, their usability in nonlinear optics is limited due to low damage thresholds [14]. An approach to further increase the nonlinear response is the combination of metallic metasurfaces with other materials, forming so-called hybrid metasurfaces. In such hybrid systems, often the strong near-fields which are present in metallic nanostructures are utilized, which arise from the excitation of so-called plasmon modes. These modes provide strongly enhanced electromagnetic fields in the proximity of each nanostructure [15, 16]. By combining plasmonic metasurfaces with materials with a high nonlinearity, the nonlinear frequency conversion efficiency can be enhanced and therefore boost the emission of certain nonlinear harmonic orders or make the emission of additional nonlinear harmonic orders possible, which are otherwise forbidden [17, 18].

In the past decade, a new material group became a focal point in the field of photonics. Since the discovery of graphene in 2005 [19, 20], the emerging field of two-dimensional materials provide promising new applications in the linear and nonlinear optical regime. Although graphene provides unique properties, like a high mechanical resilience, the lack of a band gap limits its usability in the field of optics, which is utilized in many applications, e.g. photodetectors [21]. However, the discovery of graphene and the awarding of the Nobel prize to the researchers K.S. Novoselov and A.K. Geim in 2010

encouraged further research on different materials leading to the discovery of two-dimensional transition-metal dichalcogenides (TMDC) as an alternative to graphene for optical applications [22, 23]. Similar to graphene, transition metal dichalcogenides usually occur as bulk materials consisting of stacked layers held together by van-der-Waals forces. In bulk form, TMDC materials have an indirect band gap, which changes if they are scaled down to the size of a single atomic layer, exhibiting a direct band gap with energies ranging from 1-2 eV [24, 25]. A unique characteristic of transition metal dichalcogenides is the high light-matter interaction for single-crystalline monolayers, which reaches absorbance values up to 15% for a typical thickness below 1 nm [26].

As monolayers of TMDC provide an optical band gap in the visible regime, an even stronger light-matter interaction can be realized if they are combined with plasmonic metasurfaces. Recent research on such hybrid metasurfaces has shown, that the already high light-matter interaction is enhanced due to the strong near-fields of the plasmonic nanostructures [27, 28]. In addition, TMDC's also provide the possibility of frequency conversion by second-harmonic generation (SHG) if they are scaled down to the two-dimensional state [29, 30]. It was reported, that the strong near-fields of the plasmonic nanostructures can also enhance the nonlinear response in a hybrid metasurface and further be utilized to manipulate the nonlinear harmonic generation in various ways [31, 32]. However, these studies have shown an enhanced SHG process for excitation wavelengths in the visible regime [31-33], although plasmonic metasurfaces suffer from substantial absorption losses at these excitation wavelengths [34]. Therefore, it is more practical, that the excitation wavelengths are located in the near-infrared (NIR) regime. Thus, the excitation of hybrid metasurfaces with NIR wavelengths leads to an emission of SHG in the visible regime, where studies have shown, that a strong SHG can be observed for these wavelengths [35-37].

Although most recent studies report an enhancement of SHG for photon energies close to half of the band gap energy of the TMDC-material WS_2 [38], the coupling mechanism in plasmonic/TMDC hybrid metasurfaces at these wavelengths still needs to be unraveled. Therefore, this thesis investigates the optical properties of hybrid metasurfaces consisting of plasmonic metasurfaces and a monolayer TMDC focusing on the nonlinear response of second-order for excitation wavelengths around half of the band gap energy of a monolayer TMDC. As a representative of the transition metal dichalcogenide family, the material WS_2 is chosen, providing a band gap energy of around 2 eV. Thus, this thesis investigates the second harmonic generation in plasmonic/ WS_2 hybrid metasurfaces for excitation wavelengths in the near-infrared regime with photon energies around 1 eV.

This thesis is structured in the following way. At first, the theoretical fundamentals of plasmonic nanostructures are discussed in chapter 2, including basic concepts of the description of the light-matter interaction. In addition, the nonlinear harmonic generation and its dependency on the nanostructures' symmetry are highlighted. Subsequently, fabrication methods of monolayer WS_2 as well as fundamental nonlinear optical properties are explained. It is further shown, that the hexagonal lattice structure of the WS_2 symmetry also plays a key role in the second-harmonic generation, where the polarization of the excitation light is of special interest.

The second part of this thesis deals with the characterization of the second harmonic generation arising from hybrid metasurfaces. In this context, the nonlinear signal of the second order is measured for a set of various parameters, such as excitation wavelength, polarization state, plasmon resonance and different symmetries. In chapter 3 it is shown, that the second-harmonic generation is strongly influenced by the plasmon resonance of the metallic nanoantennas, which is supported by a theoretical model describing the nonlinear response of these hybrid metasurfaces.

In chapter 4, several applications in hybrid metasurfaces are presented to illustrate the potential lying within plasmonic/TMDC hybrid metasurfaces. Therefore, the linear Pancharatnam-Berry phase is utilized to manipulate the excitation light on scales lower than the wavelength. In particular, a phase profile is introduced to show, that local constructive and destructive interference can be transferred into the far-field emission of second harmonic generation. Further, this concept of phase modulation in plasmonic metasurfaces is expanded to the encoding of several holographic images into a single phase pattern, which can be implemented into a plasmonic metasurface. Therefore, a Gerchberg-Saxton algorithm is expanded to calculate the phase profile needed for the hologram encoding utilizing the nonlinear Pancharatnam-Berry phase.

The last chapter of this work finally summarizes the results of this work with regard to the nonlinear response of hybrid metasurfaces and gives an outlook on possible future research and applications.

2.FUNDAMENTAL THEORY

This chapter covers the theoretical concept of nonlinear optics in plasmonics and monolayer transition-metal-dichalcogenides (TMDC's) to provide fundamental knowledge, necessary for the investigation of the hybrid metasurfaces discussed in this thesis. These hybrid metasurfaces consist of plasmonic nanoantenna arrays made of gold and a monolayer (1L) TMDC, which combines the well-studied field of plasmonics and the novel area of two-dimensional materials. First, the dielectric function of gold and the resulting localized plasmonic resonances appearing in subwavelength scale gold nanostructures are discussed. As these resonances provide linear and nonlinear optical responses to gold nanoparticles, the dependence of shape and size is highlighted. Subsequently, we focus on the discussion of 1L-TMDC as the second part of the hybrid metasurface and the fabrication process of single layer WS_2 with atomic thickness is illustrated. When scaling down bulk TMDC to the scale of a single atomic layer, the impact on the band structure is significant. Thus, a discussion of the nonlinear optical response in 1L-TMDC, resulting from the changed band structure, and its properties conclude this chapter.

2.1. Optical properties of gold

2.1.1. Dielectric function of gold

As this thesis handles electromagnetic waves and their interaction with matter, a basic description of the optical properties of the matter used in this thesis is required. This can be done with the help of the dielectric function ϵ_r , which is the optical material property describing the light-matter interaction in the linear regime. For this work,

harmonic time-dependent electric fields with a frequency ω are considered. As the response of a material generally depends on the frequency, ε_r is written as a complex frequency-dependent term

$$\varepsilon_r(\omega) = \varepsilon_1(\omega) + i\varepsilon_2(\omega). \quad (2.1)$$

Here, ε_1 and ε_2 represent the real and imaginary part of the dielectric function. ε_1 describe the materials interaction with an electric field through material polarization, while ε_2 determines the permanent loss of energy due to absorption in it [39]. For gold material, which plays an important role in this work, ε_r is independent of electric field (E-field) strength, position or propagation direction but yet frequency-dependent. A common approach for the description of the light-matter interaction of noble metals is the Drude-Sommerfeld model, in which the electrons in the outer electron shell of the atom are viewed as quasi-free. Gold as a noble metal has only one electron located in the outer shell. Meanwhile, the remaining electrons, which are bound in the lower electron shells, cover up the charge of the atomic nucleus, so that the quasi-free electrons in a macroscopic gold medium form an electron gas and can move freely inside of the metal. These electrons can be accelerated by external electric fields and the differential equation of motion describing a single electron in the metal is given per

$$m_e \frac{\partial^2 \vec{x}}{\partial t^2} + m_e \gamma \frac{\partial \vec{x}}{\partial t} = -e \vec{E}, \quad (2.2)$$

with m_e being the effective electron mass and e the electric charge [39]. The parameter γ describes a damping term, characterizing the scattering of the electron due to collisions by the mean time $\tau = \gamma^{-1}$ between two scattering events. τ is estimated by the Fermi velocity of the electron v_F and the mean free path l via $\gamma = v_F/l$. For harmonic time-dependent electric fields, expressed as $\vec{E}(t) = \vec{E}_0 \cdot e^{-i\omega t}$, the differential equation can be solved by the ansatz $\vec{x}(t) = \vec{x}_0 \cdot e^{-i\omega t}$, leading to the solution

$$\vec{x}(t) = \frac{e}{m_e(\omega^2 + i\gamma\omega)} \vec{E}(t). \quad (2.3)$$

Equation (2.3) implies a periodic displacement of the electron, induced by the external electric field and is dependent on its strength and frequency of the E-field. Since displaced charges generate a local dipole moment, a polarization \vec{P} along this dipole is formed. In a macroscopic system it can be expressed based on the electron density n by

$$\vec{P}(t) = -ne\vec{x}(t). \quad (2.4)$$

After applying the solution (2.3), the macroscopic polarization is given by

$$\vec{P}(t) = -\frac{ne^2}{m_e(\omega^2 + i\gamma\omega)} \vec{E}(t), \quad (2.5)$$

introducing the common definition of plasma frequency ω_p

$$\omega_p = \sqrt{\frac{ne^2}{\epsilon_0 m_e}}, \quad (2.6)$$

which is a constant specified by the medium [39]. Using this definition, the polarization can be converted and simplified by introducing the electrical susceptibility χ

$$\vec{P}(t) = -\epsilon_0 \frac{\omega_p^2}{\omega^2 + i\gamma\omega} \vec{E} = \epsilon_0 \chi \vec{E}(t). \quad (2.7)$$

It is connected with the dielectric function by $\epsilon_r = 1 + \chi$ and therefore, the dielectric function can be expressed depending on the frequency of the electric field by

$$\epsilon_r(\omega) = 1 - \frac{\omega_p^2}{\omega^2 + i\gamma\omega}. \quad (2.8)$$

For nanostructures made of gold, this term is viable for wavelengths in the infrared wavelength regime but has its limits in the visible region due to interband transitions in the gold material, which are not considered by the Drude-Sommerfeld theory. In this work, we focus on illumination with near-infrared wavelengths and therefore, abstain from a modification of the differential equation in motion and only consider (2.8) splitting it into the real and imaginary parts [40]

$$\epsilon_r(\omega) = 1 - \frac{\omega_p^2}{\omega^2 + \gamma^2} + i \frac{\gamma\omega_p^2}{\omega^3 + \omega\gamma^2}. \quad (2.9)$$

Figure 2.1 shows the real and imaginary parts of ϵ_R as a function of the wavelength ($\lambda = \frac{2\pi c}{\omega}$, c : speed of light) in the near-infrared (NIR) regime, determined by the Drude-Sommerfeld model as well as experimentally obtained values by Johnson and Christy, which are widely used in scientific research [41, 42]. Note that the real part of the

dielectric function is negative, resulting in a low penetration depth of electromagnetic waves into metals since the refractive index $n = \sqrt{\epsilon}$ becomes strongly imaginary.

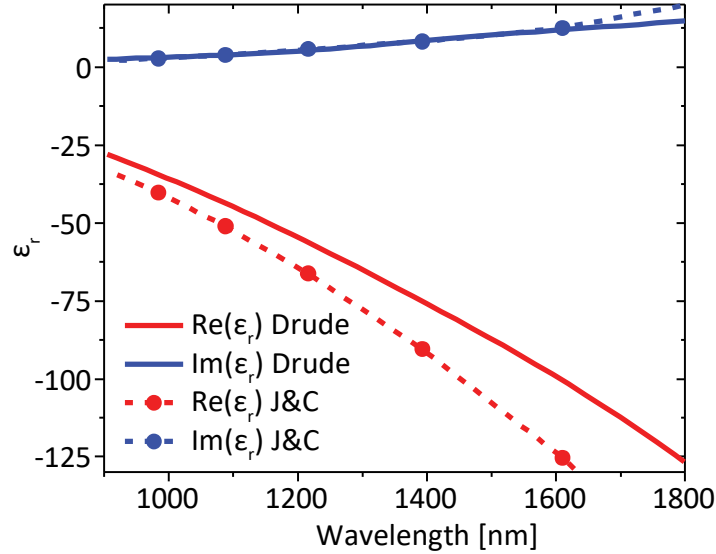


Figure 2.1 Real and imaginary part of the dielectric function of gold, calculated by the Drude-Sommerfeld-model with $\omega_p = 13.7 \cdot 10^{15} \text{ s}^{-1}$ and $\gamma = 0.805 \cdot 10^{14} \text{ s}^{-1}$ well as experimentally obtained values by Johnson and Christy [41, 42].

2.1.2. Localized surface plasmon polaritons

As described above, the excitation of electrons in gold by a periodical electromagnetic field results in a harmonic charge-density oscillation which is called plasmon oscillation. Plasmons are charge-density displacements and sub-classified into volume and surface plasmons. The structures examined in this work are of subwavelength scale and have a low volume to surface ratio. Therefore, their optical properties are mainly determined by surface plasmons and volume plasmons can be neglected. Surface plasmons arise at plane interfaces between two media, where one half-space consists of metal with a complex, frequency-dependent dielectric function, whereas the second medium is non-metallic, with a dielectric function without an imaginary part. The investigated samples in this thesis either have gold/air or gold/fused silica substrate interfaces making surface plasmons the primary source of light-matter interaction.

To further discretize the nature of the plasmons focused on in this work, the distance plasmons can travel on the surface of metals is of special interest. On large plane media at a metal/air interface, plasmons can travel several micrometers [39]. For structures with a subwavelength scale, such high travel distances are not possible for NIR excitation wavelengths of 1000-1600 nm. Thus, the travel distance of plasmons is restricted to the so-called nanostructures. Plasmons, excited in discrete subwavelength small volumes are called localized surface plasmons (LSP's) and are bound to the individual volume of each nanostructure. In confined nanostructures, a dipole is formed when electrons are dislocated by an external electromagnetic field provoking a restoring force. In analogy to the classic dipole, this force depends on the distance between the positive and negative charge of such a dipole and therefore, the restoring force in nanostructures also depends on its size. A schematic illustration of this behavior is shown in Figure 2.2 for a gold sphere nanostructure. The confinement of plasmons leads to an additional behavior of LSP's in nanostructures regarding the excitation wavelength, the frequency-dependent absorption.

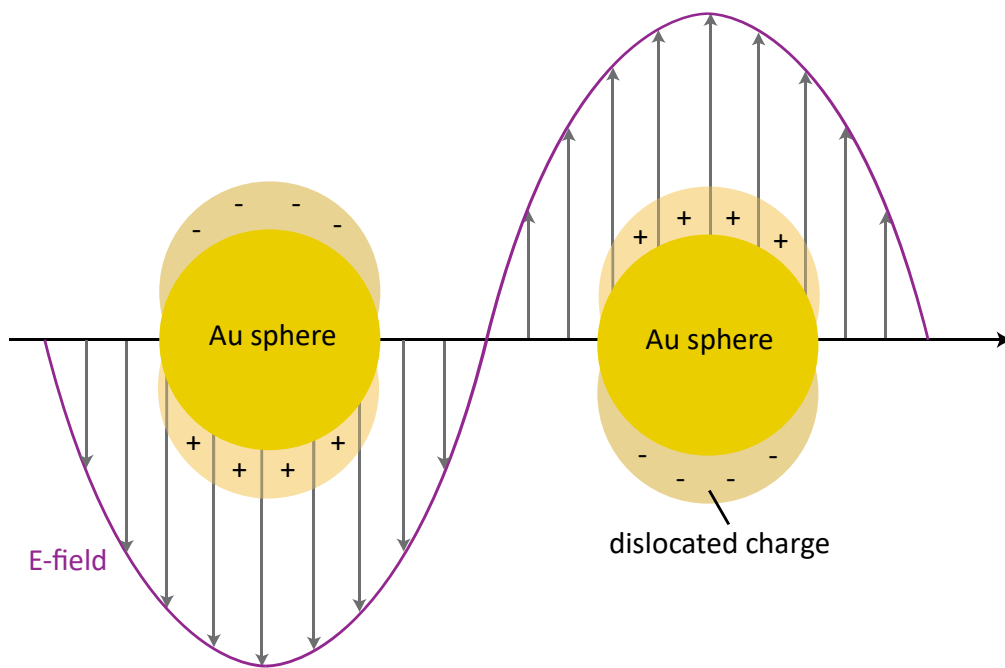


Figure 2.2: Schematic illustration of LSP's on a gold nanosphere excited by an external electric field. The dislocated electrons form a dipole inside the gold sphere.

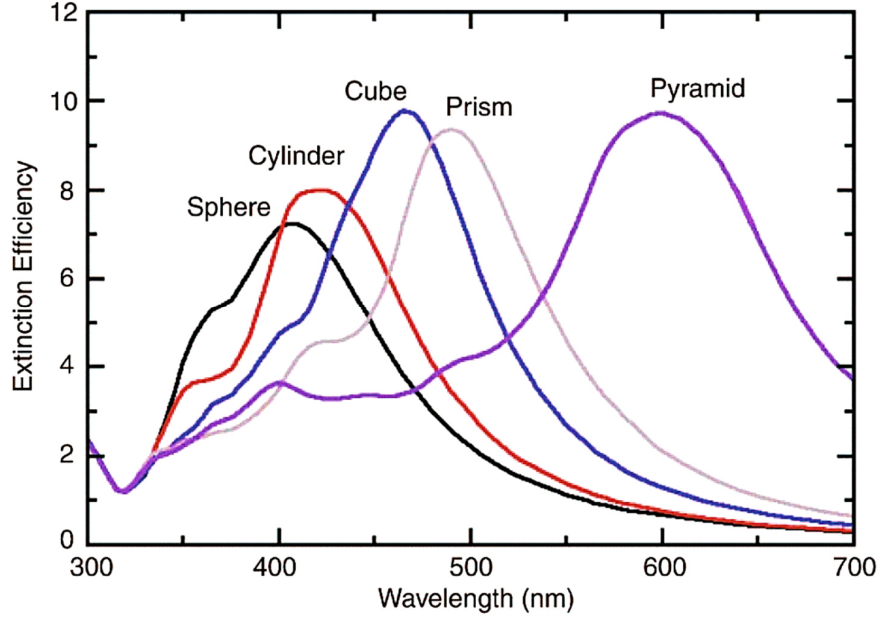


Figure 2.3: Extinction efficiency for different nanostructure shapes with the same volume as a sphere with a radius of 50nm. A similar graph was published in [43].

The eigenvalues of the plasmon oscillation are called localized surface plasmon resonances (LSPR's) and if the frequency of the exciting EM field matches such a resonance frequency, the absorption of the electromagnetic field increases. These resonance frequencies can also be expressed as resonance wavelengths, which are highly dependent on the size and shape of the nanostructure, as well as on the surrounding medium [44, 45]. For spherical gold nanostructures with a radius R , the plasmonic resonance wavelengths can be calculated by the Mie theory [46] and a simplified term to calculate the extinction spectrum is given by

$$E(\lambda) = \frac{24 \pi^2 N R^3 \varepsilon_d}{\lambda \ln(10)} \left[\frac{\varepsilon_{r,2}(\lambda)}{(\varepsilon_{r,1}(\lambda) + \xi \varepsilon_d)^2 + \varepsilon_{r,2}(\lambda)^2} \right], \quad (2.10)$$

where N is the number of polarizable elements in the sphere, ε_d the dielectric constant of the surrounding dielectric medium and $\varepsilon_r(\lambda)$ the wavelength-dependent dielectric complex function of gold introduced in equation (2.1). Of special interest is the parameter ξ , which takes the form of the nanostructure into account and has a value of 2 for the case of a sphere [47]. The values for other forms can reach up to 20 based on their aspect ratio, cannot be calculated analytically anymore and must be approximated.

Figure 2.3 illustrates the extinction efficiency, of different nanostructure shapes with the same volumes. It is shown, that for different shapes, and therefore different values of ξ , the resonance wavelength shifts to longer wavelengths away from a simple sphere. The optical properties of nanostructures with different symmetries are discussed later in this work.

2.1.3. Near-field enhancement of plasmonic nanostructures

The strong localization of surface plasmons in confined nanostructures results in a strong enhancement of the E-fields close to the nanostructure. As the plasmonic nanostructures in this work are of subwavelength scale, the phase of the excitation electromagnetic wave along the volume can be seen as constant and an electrostatic field can be assumed. For the calculation of the local field distributions, this is a common approach, where the time dependency of the electromagnetic wave is added later. Although the nanostructures investigated in this work have various shapes, the calculation of local field distributions is done for a homogeneous sphere for simplicity. Hereby, the sphere has the radius R and is located at the origin and is described by a dielectric constant ε_{sph} . It is present in an isotropic and non-absorbing medium with a dielectric constant ε_m , where a static E-field $\vec{E} = E_0 \vec{e}_z$ is applied. A schematic illustration is shown in Figure 2.4.

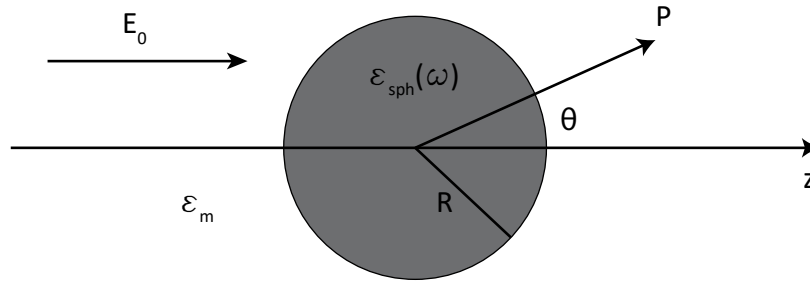


Figure 2.4: Schematic illustration of a metal sphere with dielectric constant ε_{sph} in a homogeneous medium with dielectric constant ε_m and an applied E-field in the z -direction.

For the electrostatic approach, the E-field can be calculated with the help of the Laplace equation $\nabla^2 \phi = 0$, where ϕ represents the potential, resulting in $\vec{E} = -\nabla\phi$. A suitable solution for the potential, considering the azimuthal symmetry of this problem, can be found by

$$\phi(r, \theta) = \sum_{l=0}^{\infty} [A_l r^l + B_l r^{-(l+1)}] P_l(\cos \theta), \quad (2.11)$$

where P_l are the Legendre polynomials of order l and θ the angle between the z-axis and the vector \vec{r} pointing towards point P [48]. As the potentials need to remain finite at the origin, (2.11) can be split into the potentials inside and outside of the sphere [39]

$$\phi_{in}(r, \theta) = \sum_{l=0}^{\infty} A_l r^l P_l(\cos \theta) \quad (2.12)$$

$$\phi_{out}(r, \theta) = \sum_{l=0}^{\infty} [B_l r^l + C_l r^{-(l+1)}] P_l(\cos \theta). \quad (2.13)$$

The coefficients A_l , B_l and C_l can be determined, by considering the boundary conditions $r \rightarrow \infty$ and $r = R$. For $r \rightarrow \infty$, the potential outside of the sphere must be $\phi_{out} \rightarrow -E_0 z = -E_0 r \cos \theta$, which results in $B_1 = -E_0$ and $B_l = 0$ for $l \neq 1$. The coefficients A_l and C_l can be determined at the boundary condition $r = R$, where the tangential components of the E-field must be equal

$$-\frac{1}{R} \frac{\partial \phi_{in}}{\partial \theta} \Big|_{r=R} = -\frac{1}{R} \frac{\partial \phi_{out}}{\partial \theta} \Big|_{r=R}, \quad (2.14)$$

alongside the equality of the normal components of the displacement field

$$-\varepsilon_0 \varepsilon_{sph} \frac{\partial \phi_{in}}{\partial r} \Big|_{r=R} = -\varepsilon_0 \varepsilon_m \frac{\partial \phi_{out}}{\partial r} \Big|_{r=R}. \quad (2.15)$$

Equations (2.14) and (2.15) lead to $A_l = C_l = 0$ for $l \neq 1$, leaving A_1 and C_1 as the only non-zero coefficients of the potentials ϕ_{in} and ϕ_{out} , which are determined to [48]

$$\phi_{in} = -\frac{3\varepsilon_m}{\varepsilon_{sph} + 2\varepsilon_m} E_0 r \cos \theta \quad (2.16)$$

$$\phi_{out} = -E_0 r \cos \theta + \frac{\varepsilon_{sph} - \varepsilon_m}{\varepsilon_{sph} + 2\varepsilon_m} E_0 R^3 \frac{\cos \theta}{r^2}. \quad (2.17)$$

In equation (2.17), ϕ_{out} is a superposition of two E-fields. The first term describes the initially applied E-field whereas the second term describes an E-field of a dipole located at the center of the sphere. ϕ_{out} can be rewritten as

$$\phi_{out} = -E_0 r \cos \theta + \frac{\vec{p} \cdot \vec{r}}{4\pi\varepsilon_0\varepsilon_m r^3}, \quad (2.18)$$

with \vec{p} as the dipole moment defined by

$$\vec{p} = 4\pi\varepsilon_0\varepsilon_m R^3 \frac{\varepsilon_{sph} - \varepsilon_m}{\varepsilon_{sph} + 2\varepsilon_m} \vec{E}_0. \quad (2.19)$$

Equation (2.19) shows, that the applied field induces a dipole moment inside of the metallic sphere with a magnitude proportional to $|\vec{E}_0|$. Subsequently, the polarizability α is introduced, with the help of

$$\alpha = 4\pi R^3 \frac{\varepsilon_{sph} - \varepsilon_m}{\varepsilon_{sph} + 2\varepsilon_m}, \quad (2.20)$$

so that the dipole moment can be written as $\vec{p} = \varepsilon_0\varepsilon_d\alpha\vec{E}_0$. With equations (2.16) and (2.18) the E-fields finally can be evaluated by $\vec{E} = -\nabla\phi$, resulting in [39]

$$\vec{E}_{in} = \frac{3\varepsilon_m}{\varepsilon_{sph} + 2\varepsilon_m} \vec{E}_0 \quad (2.21)$$

$$\vec{E}_{out} = \vec{E}_0 + \frac{3\vec{n}(\vec{n} \cdot \vec{p}) - \vec{p}}{4\pi\varepsilon_0\varepsilon_m r^3}. \quad (2.22)$$

As these equations represent the E-fields of a metal sphere in a quasi-static E-field, the E-field distributions can be calculated analytically. However, for shapes different from the simple sphere, these E-fields cannot be calculated analytically anymore and rather must be calculated numerically, which in modern physics is done by various tools. One of them is CST microwave studio, which is used in this work to calculate E-field

distributions and transmission spectra of various plasmonic nanoparticles arranged in arrays. Figure 2.5A shows the E-field distribution of the previously discussed metal sphere, whereas Figure 2.5B-D illustrates additional metal nanoparticles, so-called nanoantennas, of different rotational symmetries, important for this work. All metal particles presented are made of gold.

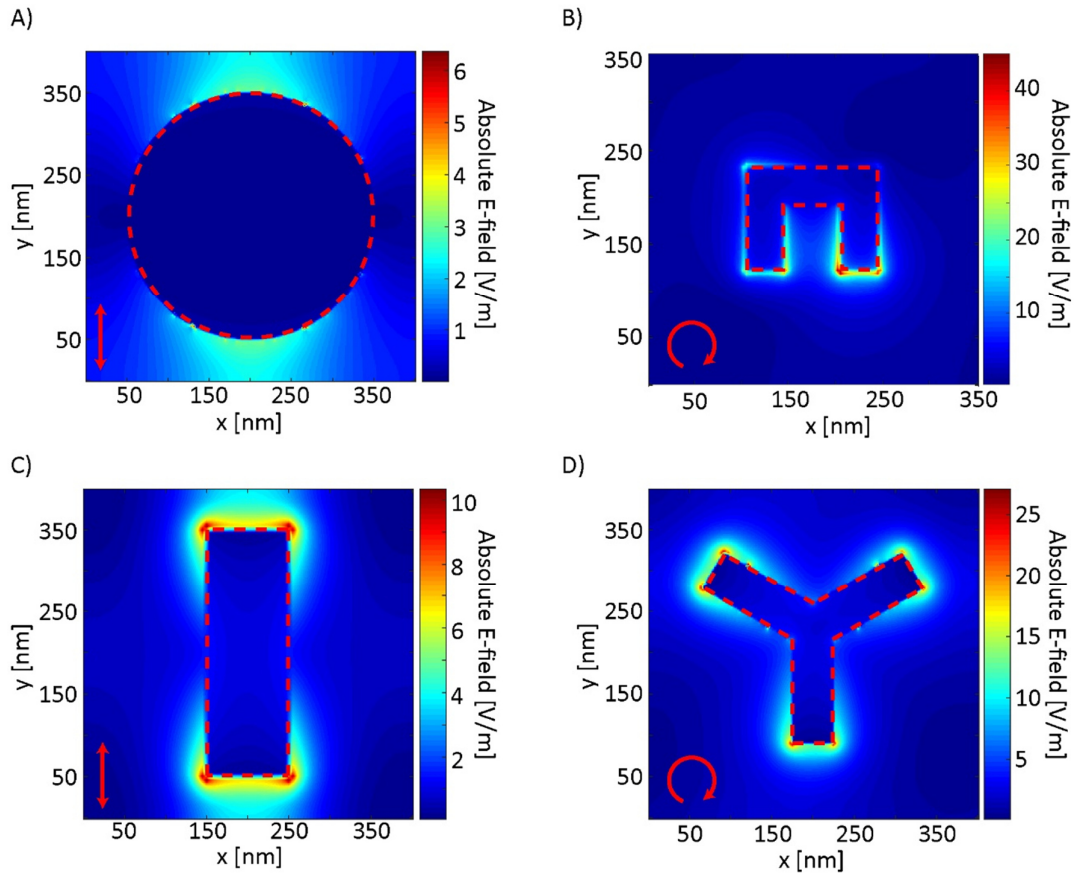


Figure 2.5: Local E-field enhancement of plasmonic gold nanoparticles. Calculated absolute E-fields of (A) a sphere ($R=150$ nm) and plasmonic nanoantennas with a (B) one-fold (C1), (C) two-fold (C2) and (D) three-fold (C3) rotational symmetry. The geometry of each nanostructure is encircled with a dotted red line and the excitation polarization is indicated by a red arrow. Note, that the nanoantennas have a small extent into the third dimension of 30 nm. 3D images are shown later in this work in Table 1.

The simulations were done with a plane wave excitation of the nanoantennas on a quartz substrate by the finite element method (FEM) and an excitation E-field of 1V/m. In the case of the nanosphere, no substrate was added but was considered for the nanoantennas after the nanostructure. The material properties of gold were taken from the publication of Johnson and Christy, which are commonly used in scientific research [42]. It is shown, that in every field distribution, a field enhancement close to each nanoparticle of up to a factor of 40 is visible. In the case of the nanoantennas, the local E-field is enhanced at the edges of the nanostructure at the end of each antenna arm, although each nanostructure is of a different shape. This field enhancement can now be utilized to enhance the emission of second harmonic generation.

2.2. Nonlinear plasmonics

2.2.1. Harmonic generation in general

An electromagnetic field \vec{E} , which excites a plasmonic nanostructure, induces a polarization \vec{P} given by equation (2.7). This remains valid for small electric field values but needs a modification for strong electric fields, which are necessary in the research field of nonlinear optics. This phenomenon of nonlinear harmonic generation is not only present in metallic nanostructures but was first discovered by Franken et. al. in 1961 in quartz substrate [49] and exists for many more materials. In nonlinear optics, the polarization is given by

$$\vec{P}(t) = \varepsilon_0 \chi^{(1)} \vec{E}(t) + \varepsilon_0 [\chi^{(2)} \vec{E}^2(t) + \chi^{(3)} \vec{E}^3(t) + \dots] = \vec{P}_L + \vec{P}_{NL}. \quad (2.23)$$

The first term describes the linear polarization as already introduced in equation (2.7), whereas the second term summarizes the polarization of higher order to a nonlinear polarization [50]. Hereby, the nonlinear susceptibility $\chi^{(n)}$ characterizes the susceptibility of the n -th order and is a $n + 1$ ranked tensor. In principle, multiple nonlinear terms can occur simultaneously, if the strength of the electric field is strong enough. However, the investigations in this work only focus on the nonlinear generation of second- and third-order and neglect higher orders. At this point, the generation of higher nonlinear orders is discussed briefly based on the example of second harmonic generation. For the nonlinear harmonic generation of second-order, $\chi^{(2)}$ as the second-

order susceptibility tensor of the medium must be taken into account for calculating the second-order polarization, given by

$$\vec{P}^{(2)}(t) = \varepsilon_0 \chi^{(2)} \vec{E}(t) \vec{E}(t). \quad (2.24)$$

The second-order polarization becomes non-zero only for certain materials. For centrosymmetric media with an inversion center, an indistinguishable point $(-x, -y, -z)$ for each point (x, y, z) in the unit cell exists. By changing the algebraic sign of the electric field, the polarization also needs to switch its algebraic sign due to the inversion symmetry:

$$\begin{aligned} -\vec{P}_2(t) &= \varepsilon_0 \chi^{(2)} \left(-\vec{E}(t) \right) \left(-\vec{E}(t) \right) \\ &= \varepsilon_0 \chi^{(2)} \vec{E}(t) \vec{E}(t). \end{aligned} \quad (2.25)$$

Comparing the two polarizations of (2.24) and (2.25) with each other, it attracts attention, that $-\vec{P}_2(t) = \vec{P}_2(t)$ is only valid for a vanishing tensor of second-order. Therefore, nonlinear generation of second-order can only exist in non-centrosymmetric media with broken inversion symmetry.

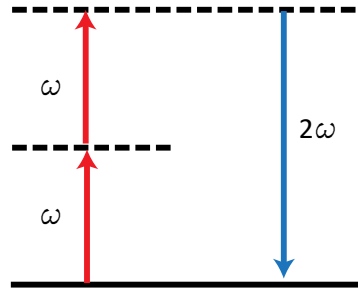


Figure 2.6: Energy level diagram for second-harmonic generation. Two photons with frequency ω are absorbed by the medium and a photon with twice the frequency 2ω is emitted.

There are several kinds of nonlinear processes of second-order and the most prominent example is the second-harmonic generation (SHG), where a photon with frequency 2ω is generated from the absorption of two photons with frequency ω . If an incident electric field, described by

$$\vec{E}(t) = \vec{E} e^{-i\omega t} + c. c. , \quad (2.26)$$

induces a polarization in a medium with a non-zero second-order susceptibility $\chi^{(2)}$, the second-order polarization is calculated with the help of equation (2.24) resulting in [50]

$$\vec{P}^{(2)}(t) = 2 \varepsilon_0 \chi^{(2)} \vec{E} \vec{E}^* + \varepsilon_0 \chi^{(2)} (\vec{E}^2 e^{-i2\omega t} + c.c.). \quad (2.27)$$

Here, the second term describes the polarization of the electric field with the frequency of 2ω . A schematic illustration of the SHG process is given by an energy level diagram in Figure 2.6. During the SHG process, two photons with frequency ω are destroyed and a single photon with twice the frequency 2ω is created simultaneously. The solid line represents the ground state, whereas the dashed lines indicate virtual states.

Another nonlinear process of second-order arises, when two electric fields with different frequencies are considered. In this case, the electric field is written as

$$\vec{E}(t) = \vec{E}_1 e^{-i\omega_1 t} + \vec{E}_2 e^{-i\omega_2 t} + c.c. \quad (2.28)$$

and the polarization of second-order is calculated again with equation (2.24) to

$$\begin{aligned} \vec{P}^{(2)}(t) = \varepsilon_0 \chi^{(2)} [& \vec{E}_1^2 e^{-2i\omega_1 t} + \vec{E}_2^2 e^{-2i\omega_2 t} + 2\vec{E}_1 \vec{E}_2 e^{-i(\omega_1 + \omega_2)t} \\ & + 2\vec{E}_1 \vec{E}_2^* e^{-i(\omega_1 - \omega_2)t} + c.c.] + 2\varepsilon_0 \chi^{(2)} [\vec{E}_1 \vec{E}_1^* + \vec{E}_2 \vec{E}_2^*]. \end{aligned} \quad (2.29)$$

The complex term contains four different optical processes, which are SHG generation for the two exciting electric fields with ω_1 and ω_2 , a sum-frequency generation (SFG) term as well as a difference frequency generation (DFG). The last term is called optical rectification and does not have any time dependency or frequency. The generation process for the two SHG terms is the same as described previously, depicted in Figure 2.6, whereas the SFG and DFG are of a different kind and depicted in Figure 2.7.

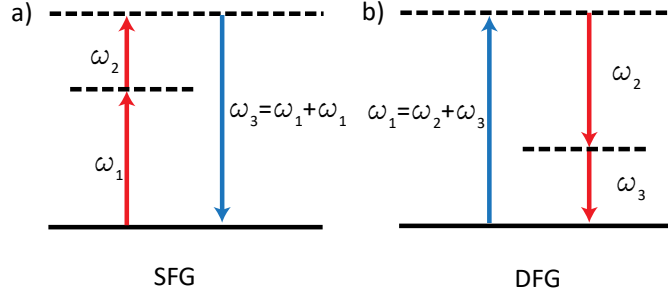


Figure 2.7: Energy level diagram of different types of nonlinear second-order processes. (a) sum-frequency generation (SFG) (b) difference-frequency generation

For SFG, two photons with different frequencies ω_1 and ω_2 are absorbed by a medium with a non-zero $\chi^{(2)}$ and generate a photon of higher frequency $\omega_3 = \omega_1 + \omega_2$, whereas in DFG a photon of higher frequency ω_1 is absorbed in the first place. Subsequent, the excited state decays into two photons of lower frequencies ω_2 and ω_3 . Note that in this case, an electric field with the frequency ω_2 is already present and stimulates the emission of additional photons with the same frequency. This process is also known as optical parametric amplification and is utilized in the laser system used in this work (Coherent Monaco Laser in combination with an Opera-F optical parametric amplifier) to generate short laser pulses of ~ 50 fs in the infrared wavelength range.

As the nonlinear generation of third-order plays a supportive role in this work, a brief discussion is added at this point. Similar to the second-order polarization, given by equation (2.24), the third-order polarization as part of equation (2.23) of the nonlinear polarization is given by

$$\vec{P}_3(t) = \varepsilon_0 \chi^{(3)} \vec{E}(t) \vec{E}(t) \vec{E}(t). \quad (2.30)$$

In analogy to the second-order polarization case, the three participating electric fields can have different frequencies ω_1, ω_2 and ω_3 , resulting in a complex third-order polarization with 44 different frequency components. In this work, we focus on nonlinear harmonics generated by monochromatic electromagnetic fields with the same frequency ω given by equation (2.26), resulting in the less complex third-order polarization

$$\vec{P}_3(t) = \varepsilon_0 \chi^{(3)} \left((\vec{E}^3 e^{-3i\omega t} + c.c.) + 3 \vec{E} \vec{E}^* (\vec{E} + \vec{E}^*) e^{-i\omega t} \right). \quad (2.31)$$

Here, the first term in (2.31) describes an electromagnetic field with a frequency thrice as large as the excitation frequency referring to the process of third-harmonic generation (THG). The corresponding energy level diagram is shown in Figure 2.8 [50].

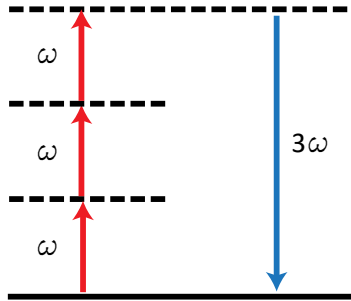


Figure 2.8: Energy level diagram for third-harmonic generation. Three photons with frequency ω are absorbed by the medium and a photon with thrice the frequency (3ω) is emitted.

2.2.2. Harmonic generation in plasmonics

The consideration of symmetry is essential when it comes to nonlinear harmonic generation and this holds true in the case of plasmonic nanoantennas. Since plasmonic nanoantennas can be fabricated in various geometries, different kind of symmetries can be realized. For this work, only three different nanoantenna symmetries are of interest, which are notated by C1, C2 and C3, representing the one-, two- and three-fold rotational symmetry, respectively. A schematic illustration of nanoantennas with each rotational symmetry can be found in Table 1. Recent research in nonlinear optics has shown, that the harmonic generation of the n -th order in plasmonic nanoantennas under circular polarization excitation is described by the selection rule [51]

$$n = l m + \sigma. \quad (2.32)$$

Here, l is an integer with $l \geq 1$ and m characterizes the rotational symmetry ($m = 1, 2, 3$). Further, $\sigma = \pm 1$ corresponds to the co- (+1) or cross- (-1) polarization state of the harmonic generation. Note, that the naming “co-” and “cross-” correspond to the same (co-) and opposite (cross-) circular polarization state as the input polarization. By applying the selection rule on the three different rotational symmetries of the plasmonic nanoantennas, it stands out, that SHG is only allowed for nanoantennas with C1 and C3

rotational symmetry and forbidden for the nanoantenna with C2 symmetry. This is supported by the fact, that the inversion symmetry is broken for nanoantennas with a C1 and C3 rotational symmetry. Table 1 gives an overview of the allowed nonlinear harmonic generations and its helicity σ for the different nanoantenna symmetries.




Harmonic order n	C1 	C2 	C3 
1	σ^-	σ^-	-
2	σ^-/σ^+	-	σ^-
3	σ^-/σ^+	σ^-/σ^+	

Table 1: Allowed harmonic generation of n -th order for the plasmonic nanoantennas with C1, C2 and C3 rotational symmetry. σ represents the helicity of the harmonic generation, where σ^+ and σ^- correspond to the co- and cross-polarization state in respect to the circular input polarization state. A similar table can be found in [2, 51].

2.3. Monolayer WS₂ – transition metal dichalcogenides

In the following, the second part of the hybrid metasurfaces, the two-dimensional transition metal dichalcogenide WS₂ is discussed. As one of the latest research topics, two-dimensional materials have gained interest since the awarding of the Nobel Prize for the discovery of graphene in 2010. Later in that year, researchers have found a similar material group, which is also scalable down to an atomic thickness and called transition metal dichalcogenides (TMDC) [24, 52]. TMDC's are layered materials consisting of one metal atom M and two chalcogen atoms X with the generic formula of MX₂ [53]. These materials are semi-metals usually present as bulk material consisting of stacked layers, similar to graphite. While in bulk form, the band gap in TMDC's is of non-direct character and therefore, optical experiments were limited to transmission and Raman spectroscopy [54, 55]. However, the downscaling of TMDC's to a monolayer thickness changes the indirect band gap to a direct band gap resulting in a greater usability for optical applications than graphene. Such optical applications make use of

the comparatively large light-matter interaction of a monolayer making them highly attractive for various optical applications like photodetectors, transistors, diodes and solar panels [21, 56-59].

2.3.1. Fabrication of 1L-WS₂

Mainly, monolayers of TMDC's are fabricated by either mechanical exfoliation (ME) or chemical vapor deposition (CVD) [60]. The fabrication method of ME (Figure 2.9A) is a top-down method, where a scotch tape is placed onto a bulk of the desired TMDC material. After peeling the scotch tape off the bulk, residuals of the TMDC (MX₂) stick to the scotch tape. At this point, small areas of 1L-TMDC can already be identified on the sticky surface of the scotch tape. Afterward, the scotch tape is placed onto a substrate material of choice and peeled off again. Due to adhesion, the small areas of monolayer TMDC remain on the surface of the substrate. While the fabrication of 1L-WS₂ with ME provides single-crystalline flakes of high quality, their size is usually limited and often residuals of the transfer medium remain on the substrate. Although recently, progress was made with this technique, the fabrication method of CVD provides 1L-TMDC's at larger scales with up to several mm, but with the drawback of not being purely single-crystalline anymore if grown in large scales [61, 62]. Different from the fabrication method of ME, CVD is a bottom-up technique (Figure 2.9C), where a chalcogen gas X (e.g. S) is added to a carrier gas flowing through a reaction chamber. Inside of this chamber, a substrate, coated with a precursor material (e.g. WO₃) of the desired transition metal M, is placed and heated up to certain temperatures, to support the sulfurization process forming TMDC crystals (e.g. WS₂) [63, 64]. This leads to another property the two fabrication methods are separated by. While for CVD grown monolayer TMDC's the flakes have a triangular shape, the 1-WS₂ transferred by ME onto a substrate can have arbitrary shapes, due to the uncontrollable transfer process, where monolayers are ripped off the bulk material. Figure 2.9B&D shows examples of 1L-WS₂ on fused quartz substrate which were transferred by ME and grown via CVD, respectively.

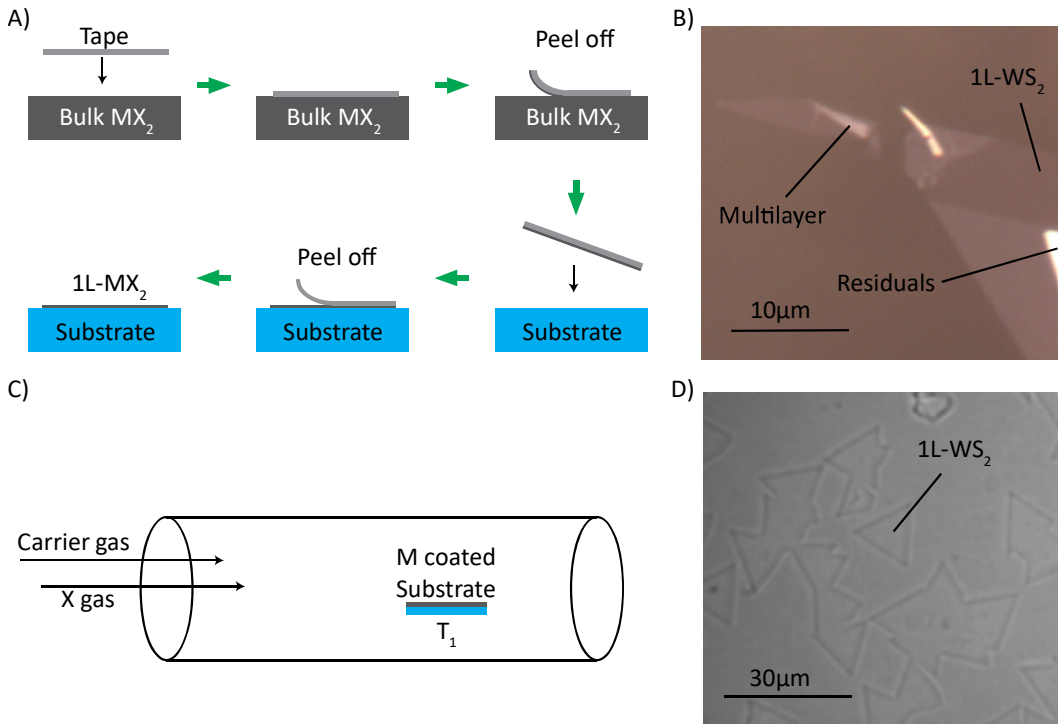


Figure 2.9: Fabrication methods of 1L-TMDC's. (A) Principle of 1L-TMDC fabrication method mechanical exfoliation (ME). (B) White light image of exfoliated 1L- WS_2 . (C) Principle of fabrication method chemical vapor deposition (CVD). (D) White light image of CVD-grown 1L- WS_2 .

It is worth noting, that modifications from this form of CVD exist, where the chalcogen atoms X are present in powder form placed next to the M coated substrate, or where the transition metal M is added in a gaseous form to the carrier gas. Nevertheless, all of these fabrication variations are similar in their growing process. For this work 1L- WS_2 fabricated by both, ME and CVD were used. The fundamental studies, which investigate the coupling of plasmonic nanoantennas to the 1L- WS_2 were done with mechanically exfoliated 1L- WS_2 and transferred onto plasmonic nanoantenna arrays. These are discussed later in this thesis. Due to their single crystalline structure, these monolayers are more suitable for fundamental investigations but are only of small scales. Therefore, the plasmonic nanoantenna arrays (metasurfaces) only have a comparatively small area of around $10 \times 10 \mu\text{m}$. As further different applications discussed in this work need metasurfaces with larger areas, 1L- WS_2 fabricated by CVD was used to reach a greater coverage density for hybrid metasurfaces. Therefore, commercially CVD-grown sample

substrates covered with monolayer WS_2 -flakes were bought from the company “2Dsemiconductors” and processed with plasmonic metasurfaces on top.

2.3.2. Band and lattice structure of WS_2

The monolayers of WS_2 are usually present in the so-called 2H polymorphs, which is a notation originating from its bulk material, describing its hexagonal symmetry present in stacked layers. An illustration of the layered bulk material is shown from a side view in Figure 2.10A. Since the structure of 1L- WS_2 does not differ from its layered bulk form, the notation is kept for the 2D case. By looking at the lattice structure of 1L- WS_2 from a top-down view (xy -plane), a hexagonal lattice structure is visible (Figure 2.10B). Note that the 2D-layer still has an extent into the third dimension (z -direction), although being quite small due to its atomic thickness (see Figure 2.10C). As already mentioned, TMDC's are layered materials and are usually present in bulk material, consisting of stacked layers held together by van der Waals forces. In bulk state, TMDC's have an indirect band gap, which is very unfavorable for optical applications. By scaling them down to the size of monolayer thickness, the indirect band gap transitions to a direct band gap and can reach values of up to 2 eV for 1L- WS_2 [25]. This mechanism can be explained by the decreased influence of neighboring layers on the band structure. For a decreasing number of layers in stacked TMDC's, the indirect band gap, located between the Γ - Q -points in the Brillouin zone (illustrated in Figure 2.10D), increases. This increase is caused by a decreasing energy level of the electron states at the Γ -point in the valence band (VB) and an increased energy level of the electron states at the Q -point in the conduction band (CB), which are a measure of the layer interaction in stacked TMDC's. With fewer layers contributing to this interaction, the difference of these energy levels increases, resulting in an increasing indirect band gap. Simultaneously, the energy levels of the electron states located at the K point in the CB and VB, are widely unchanged, since these states are a measure of the electron interaction in-between one layer. By removing all neighboring layers, no layer interaction is present anymore and the direct band gap located at the K point of the Brillouin zone is smaller than the indirect band gap between the Γ - Q -points [53]. A schematic illustration of the WS_2 band structure transition from bulk to 2D material is shown in Figure 2.10D-E, where the indirect band gap in bulk WS_2 is marked by a red arrow and the direct band gap in 1L- WS_2 is marked by a green arrow.

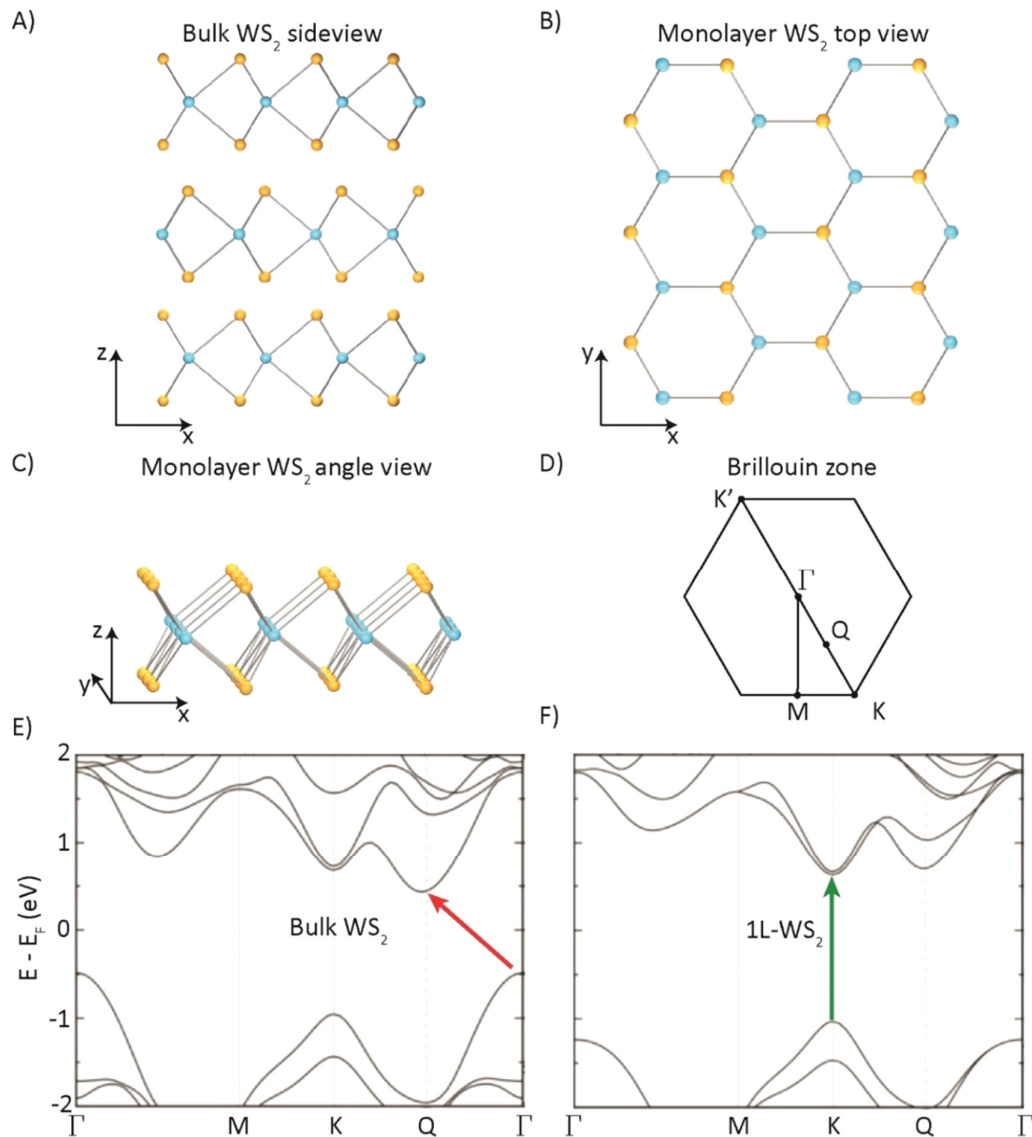


Figure 2.10: Lattice and Band structure of WS₂. (A) Side view of layered WS₂ bulk material present in 2H polymorph. (B) Top view of a monolayer WS₂. (C) Three-dimensional representation of 1L-WS₂. Note, that the W atoms are colored in Blue and the S atoms in yellow. (D) Brillouin zone of 1L-WS₂ and the corresponding high-symmetry points [65]. (E) The indirect band gap in WS₂ bulk material (F) Direct band gap in monolayer WS₂. The arrows indicate the fundamental band gap colored in red (indirect) and green (direct). A similar image of the band structures was published in [66].

2.4. Optical properties of 1L-WS₂

Similar to bulk materials (e.g. gold, presented in Figure 2.1), researchers have tried to determine the dielectric function of monolayers TMDC's. However, it is difficult to describe a quasi 2D-material with a complex dielectric function, since it is usually defined by a light wave traveling through a medium much larger than its wavelength. Although this is not the case for 1L-TMDC's, various results for 1L-WS₂ were obtained by ellipsometry (Ermolaev et. al.), thin-film approximation (Jung et. al.) and micro reflectance spectroscopy (Hsu et. al.) [67-69]. Their results are shown in Figure 2.11.

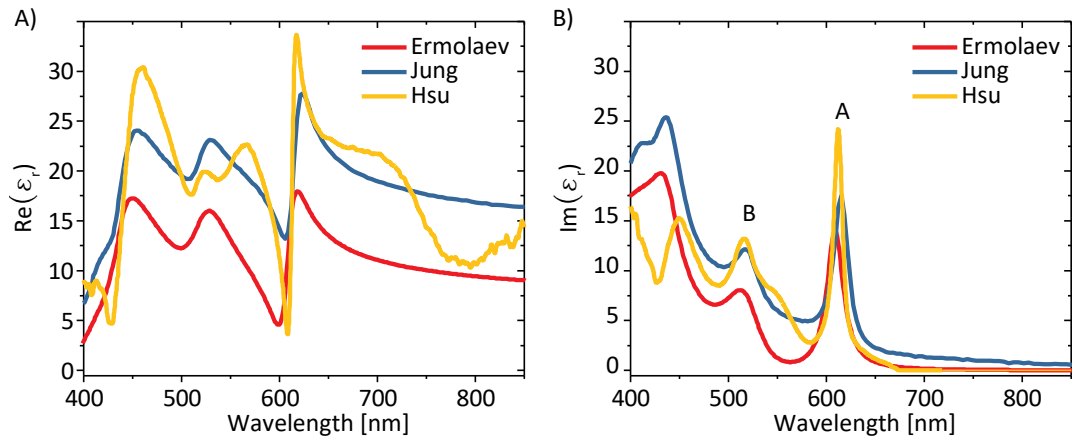


Figure 2.11: Dielectric function of 1L-WS₂. (A) Real and (B) imaginary part of the dielectric function ϵ_r obtained by different experimental approaches. The presented data were published by different authors in [67-69].

Although the different experimental approaches provide varying results for the dielectric function, some key features are present in each data set. First of all, for longer wavelengths greater than 700 nm, the imaginary part of the dielectric function converges against zero, relating to almost no dumping effect for these wavelengths. For the sake of completeness, it should be mentioned, that the data of Ermolaev et. al. supports this observation for wavelengths greater than 850 nm, although it is not shown here. Further, all data sets show a distinct local maximum at around 615 nm for $\text{Im}(\epsilon_r)$, corresponding to a photon energy of ~ 2 eV and the direct band gap of 1L-WS₂, which is illustrated in Figure 2.10F by the green arrow. By exciting an electron present in the electron states located at the K-point of the VB via optical excitation, it transitions into the CB with the lowest energy level electron state, also located at the K-point, and leaves

a positively charged hole in VB behind. The excited electron in the CB and the leftover hole in the VB form an ephemeral quasi-particle, the so-called exciton, bound by the present coulomb forces between the two opposite charged particles. Although excitons usually can be described as either Frenkel- or Wannier-Mott-excitons, the excitons present in 2D-materials exhibit characteristics of both, e.g. a large dilation (Wannier-Mott) while also being strongly bound (Frenkel) [53]. In 2D-TMDC's several excitonic states are present. They are labeled alphabetically and differ from each other by their binding energy depending on the energy levels of the electron and hole. The data sets of the imaginary part of the dielectric function, shown in Figure 2.11B, highlight two local maxima corresponding to the so-called A- and B-exciton in 1L-WS₂. As in this work, the 1L-WS₂ are excited with photon energies with less than 2.4eV (energy of B-exciton), only the optical excitation of the A-exciton is of interest.

2.4.1. Photoluminescence in 1L-WS₂

For the 1L-WS₂ as part of the hybrid metasurfaces, investigated in this work, the monolayer thickness needs to be confirmed. This can be done by photoluminescence (PL) measurements, which is a commonly used method utilizing the direct band gap of the 1L-WS₂. If the 1L-WS₂ is excited at wavelengths with photon energies greater than the band gap energy, an electron in the VB is transitions into the CB. After the excitation, the electron relaxants back to the local minimum in the CB and recombines with the hole, which was left in the VB after the excitation. Subsequently, it releases its energy in form of a photon with an energy as great as the band gap energy of 2 eV. A schematic illustration of this process is illustrated in Figure 2.12B. In the experiments, the 1L-WS₂ is excited by a laser diode emitting a continuous light wave with a wavelength of 532 nm, which equals a photon energy of 2.33 eV. The excitation laser light was focused onto the sample surface by a lens with a focal length of 100 mm. In order to be able to illuminate different area sizes on the sample surface, the lens was mounted onto a stage. In this way, the focus point can be shifted away from the sample surface. The emitted PL-light is collected by a microscope objective (Nikon x20, Numerical Aperture (NA) 0.4) and filtered by a band pass (BP), which absorbs the excitation wavelength and only transmits wavelengths ranging from 590-650 nm. As the band gap energy of 1L-WS₂ is around 2 eV (\approx 615 nm), the PL-light passes the BP. The filtered PL-light is then analyzed by either an sCMOS camera (Andor Zyla camera) or a spectrometer, which consists of a grid monochromator and a CCD camera (Andor iDus camera) with typical integration times

of a few seconds. A schematic illustration of the setup is shown in Figure 2.12A, whereas the experimental results of the PL-measurement are illustrated in Figure 2.12C-D.

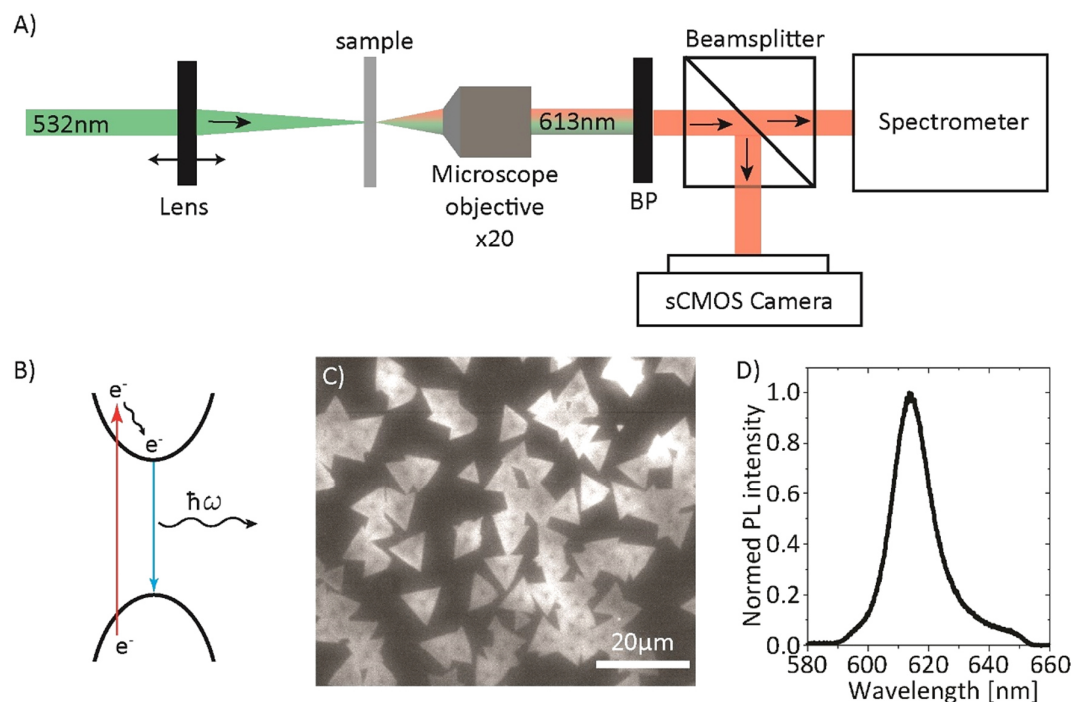


Figure 2.12: Photoluminescence measurement. (A) Schematic illustration of the used PL-setup. (B) Schematic illustration of the PL-process present in 1L- WSe_2 under excitation with photon energies greater than the band gap. (C) PL-image of the 1L- WSe_2 triangle flakes. (D) Normalized PL-spectrum emitted by the 1L- WSe_2 flakes shown in C. The center of the peak is located at 614 nm.

Figure 2.12C shows, that the individual CVD-grown 1L- WSe_2 flakes emit strong PL-light, making them even more visible than under normal white-light illumination (Figure 2.9D). To confirm the monolayer thickness of the flakes, the spectrum of the PL-light is analyzed, where a local maximum at around 615 nm is expected. Previous studies have shown, that the PL-intensity drops dramatically for stacked TMDC consisting of two or more layers by more than two orders of magnitude [70]. In addition to the decreased PL-intensity, an additional local maximum in the PL-spectrum is formed at slightly greater wavelengths for e.g. a bi-layer. In that case, this second peak would partially overlap the first PL-peak, which indicates monolayers, resulting in a double-peaked spectrum. However, this is not the case in the measured PL-spectrum, shown in Figure 2.12D, where a single peak located at 614 nm confirms the monolayer thickness

of the measured flakes within the range of experimental uncertainties. Based on these observations, the presence of predominantly monolayer WS₂ can be assumed. It should be noted, that CVD-grown 1L-WS₂ flakes might not always emit uniform PL-light over their entire monolayer area. This change in emission arises from uncertainties in the fabrication process or due to a presence of grain boundaries or bi- or multilayers [63, 64, 71]. However, if a single peak located at around 614 nm is visible in the PL-spectrum emitted by the investigated WS₂, it can be assumed, that predominantly monolayers of WS₂ are present.

2.4.2. Second-harmonic generation in 1L-WS₂

Due to the presence of two different atoms (W and S) in its unit cell, the hexagonal lattice structure of the 1L-WS₂ has a broken inversion symmetry, which is a fundamental property necessary for second-harmonic generation. As a detailed description of general SHG is given in chapter 2.2.1, the SHG in 1L-WS₂ is of special character. It is restricted by certain selection rules for circular polarization states and possesses certain symmetries when it is generated with linear polarized light. The SHG in 1L-WS₂ discussed in this work is exciton-enhanced, meaning, that the two-photon energy matches the band gap energy of 1L-WS₂ allowing the excitation of excitons by two-photon absorption [35, 72]. Although some of the plasmonic nanostructures as part of the hybrid metasurfaces presented in this work can support the SHG due to their broken inversion symmetry, it will be shown, that the SHG arising from these hybrid metasurfaces is also mostly of exciton-enhanced character. Nevertheless, as part of this chapter, the following fundamental principles are regarding the exciton-enhanced SHG in 1L-WS₂. To fully describe the process of SHG in 1L-WS₂, the second-order polarization, as defined in equation (2.24), needs to be viewed in a more general way of

$$P_i(2\omega) = \varepsilon_0 \sum_{jk} \chi_{ijk}^{(2)} E_j(\omega) E_k(\omega), \quad (2.33)$$

where i, j, k represent the Cartesian components of the E-fields and the second-order susceptibility tensor [50]. Often, the tensor d_{ijk} instead of the second-order susceptibility is used, which is given by

$$d_{ijk} = \frac{1}{2} \chi_{ijk}^{(2)}. \quad (2.34)$$

For the case of SHG, the E-fields $E_j(\omega)$ and $E_k(\omega)$ are exchangeable and therefore, the indices j and k are permutable, which leads to $d_{ijk} = d_{ikj}$. If the indices j and k are permutable, they can be summarized to a new index l by means of $xx = 1, yy = 2, zz = 3, yz = zy = 4, zx = xz = 5$ and $xy = yx = 6$. Then, the susceptibility tensor of second-order can be represented by the 3x6-element matrix

$$d_{il} = \begin{bmatrix} d_{11} & d_{12} & d_{13} & d_{14} & d_{15} & d_{16} \\ d_{21} & d_{22} & d_{23} & d_{24} & d_{25} & d_{26} \\ d_{31} & d_{32} & d_{33} & d_{34} & d_{35} & d_{36} \end{bmatrix}. \quad (2.35)$$

This matrix can further be reduced, if the Kleinman symmetry is applied, which states that the second-order susceptibility is frequency independent and the material responds instantaneously to applied E-fields. Under these conditions, the medium is necessarily lossless [50]. This applies to 1L-WS₂ for NIR-wavelengths, where no dumping effects are visible for these wavelengths (see chapter 2.4). Resulting, the 18 independent elements in d_{il} can be reduced down to 10 elements, so that the second-order polarization is calculated by [50]

$$\begin{pmatrix} P_x(2\omega) \\ P_y(2\omega) \\ P_z(2\omega) \end{pmatrix} = 2\varepsilon_0 \begin{bmatrix} d_{11} & d_{12} & d_{13} & d_{14} & d_{15} & d_{16} \\ d_{16} & d_{22} & d_{23} & d_{24} & d_{14} & d_{12} \\ d_{15} & d_{24} & d_{33} & d_{23} & d_{13} & d_{14} \end{bmatrix} \begin{bmatrix} E_x(\omega)^2 \\ E_y(\omega)^2 \\ E_z(\omega)^2 \\ 2E_y(\omega)E_z(\omega) \\ 2E_x(\omega)E_z(\omega) \\ 2E_x(\omega)E_y(\omega) \end{bmatrix}. \quad (2.36)$$

As d_{il} represents the second-order susceptibility of crystal structures, it contains symmetry properties, which are different for every crystal structure. Since 1L-WS₂ has a hexagonal lattice structure, it belongs to the D_{3h} point-group, which has only a few non-zero d_{il} -elements. They are given by $\chi_{WS_2}^{(2)} = \chi_{xxx}^{(2)} = -\chi_{xyy}^{(2)} = -\chi_{yyx}^{(2)} = -\chi_{yxy}^{(2)}$, where x and y are defined as shown in Figure 2.10B in regard to the hexagonal lattice structure [73]. Note, that these directions are also often labeled with armchair (x-axis) and zigzag (y-axis) direction (see Figure 2.10B). For the excitation of 1L-WS₂ with linear polarized light ($\vec{E} = E_0(\cos\theta \vec{e}_x + \sin\theta \vec{e}_y)$) propagating in z-direction (no E-field z-components), the second-order polarization can be calculated to

$$\vec{P}_{2\omega}^{(2)} = d_{eff} \begin{pmatrix} \cos^2\theta - \sin^2\theta \\ -2\cos\theta \sin\theta \\ 0 \end{pmatrix}. \quad (2.37)$$

Note, that any non-angle dependent parameter (e.g. ϵ_0 or the values of the susceptibility tensor) are considered by d_{eff} . It can be shown, that the component parallel (or perpendicular) to the polarization state of the exciting light depends on the relative angle θ between the input polarization and the x-axis of the hexagonal lattice structure. The resulting E-fields can be written as

$$E_{\parallel}(2\omega) = C \chi_{WS_2}^{(2)} \cdot \cos(3\theta + \theta_0) \text{ and} \quad (2.38)$$

$$E_{\perp}(2\omega) = C \chi_{WS_2}^{(2)} \cdot \sin(3\theta + \theta_0), \quad (2.39)$$

where $E_{\parallel}(2\omega)$ and $E_{\perp}(2\omega)$ are the E-field components parallel and perpendicular to the incident polarization state, respectively. Here, C is a proportional constant containing local-field factors determined by the local dielectric environment and θ_0 is the initial orientation of the hexagonal lattice structure. By only measuring the intensity component parallel (or perpendicular) to the incident polarization state, the SHG signal becomes angle-dependent and has a 6-fold character, described by $I_{2\omega} \propto \cos^2(3\theta + \theta_0)$ [73]. In Figure 2.13 a characteristic intensity distribution dependent on the polarization angle θ is shown. For clarification, the inset illustrates the corresponding hexagonal lattice structure of the unit cell of 1L-WS₂ which is rotated by an angle of $\theta_0 = 46^\circ$. Note, that the collected data can only measure absolute intensity values and does not contain any information about the phase and therefore, an arbitrariness of $\theta = 60^\circ$ is inevitable.

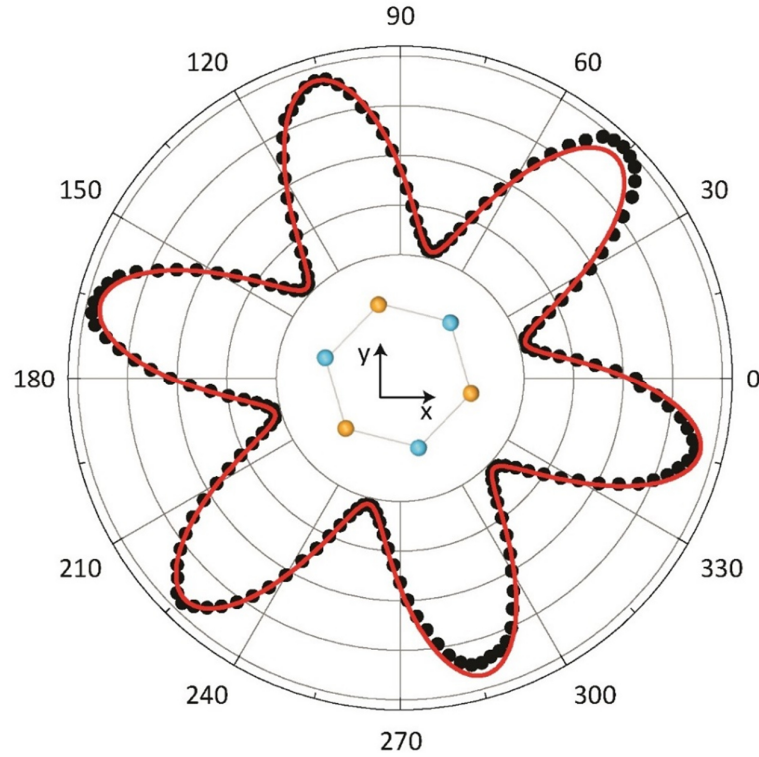


Figure 2.13: Polarization-dependent SHG. The black dots represent the measured SHG signal of 1L-WS₂ obtained by measuring the SHG intensity parallel to the incident polarization $E_{||}(2\omega)$, as defined in (2.38). The red data represents a fit defined by equation (2.38) to calculate the relative orientation angle θ_0 of the hexagonal lattice structure in regard to the x-axis, which is determined to $\theta_0 \approx 46^\circ$.

When 1L-WS₂ is excited with circularly polarized light, the SHG underlies certain selection rules, which can be led back to the K and K' valley-dependent interband transitions in the Brillouin zone (Figure 2.10D), justified by the symmetry of the hexagonal lattice structure. In the following, we denote the right- (left-) circular polarized (RCP/LCP) light with σ^+ (σ^-). The selection rules are illustrated in Figure 2.14A, depicting, that if two photons with a fundamental wavelength λ_{fund} and σ^+ - (σ^- -) polarization state are absorbed by the 1L-WS₂, they excite an electron from the VB into the CB at the K- (K'-) point of the Brillouin zone (Figure 2.10D). After the relaxation of the electron by recombination with the hole in the VB, one photon with a wavelength $\lambda_{\text{SHG}} = \lambda_{\text{fund}}/2$ and the opposite helicity σ^- (σ^+) is emitted.

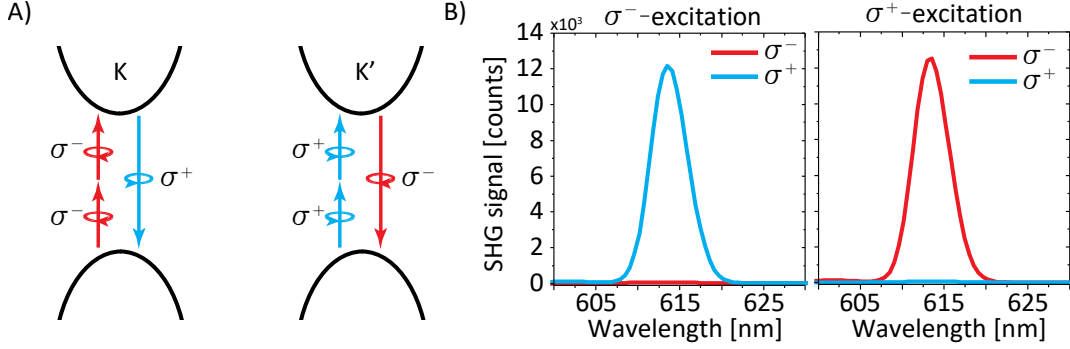


Figure 2.14: Optical selection rules for SHG. (A) Interband valley dependent selection rules for circular polarization **(B)** Circular polarization-resolved SHG spectra for left (σ^-) and right (σ^+) circular polarization excitation.

This selection rule is expected from materials with a 3-fold rotational and broken inversion symmetry, where the angular momentum mismatch of the absorbed and emitted photons is supplied by the lattice [74, 75]. Figure 2.14B shows measured polarization-dependent SHG spectra, confirming the optical selection rules. In analogy to the linear polarized SHG signals, the second-order polarization under excitation with circularly polarized light can be calculated. Therefore, the right- and left-circular polarized E-fields $\vec{E}_{\sigma^+} = 1/\sqrt{2}(\vec{e}_x - i \cdot \vec{e}_y)$ and $\vec{E}_{\sigma^-} = 1/\sqrt{2}(\vec{e}_x + i \cdot \vec{e}_y)$ (no E-field z-component) are inserted into (2.36) alongside the non-zero elements of the matrix d_{il} , providing the second-order polarizations by

$$\vec{P}_{2\omega}^{\sigma^+} = \begin{pmatrix} 1 \\ i \\ 0 \end{pmatrix} \text{ and} \quad (2.40)$$

$$\vec{P}_{2\omega}^{\sigma^-} = \begin{pmatrix} 1 \\ -i \\ 0 \end{pmatrix}.$$

The equations in (2.40) show, that the RCP and LCP second-order polarizations $\vec{P}_{2\omega}^{\sigma^+}$ and $\vec{P}_{2\omega}^{\sigma^-}$ are cross-polarized in regard to their excitation polarization LCP and RCP. This conforms to the selection rules, illustrated in Figure 2.14.

3. INFLUENCE OF PLASMON RESONANCES ON SHG IN HYBRID METASURFACES

It was shown in chapter 2.4.2, that the process of SHG in 1L-WS₂ for excitation with linear polarized light strongly depends on the polarization angle relative to the orientation of the 1L-WS₂ hexagonal lattice structure. A similar behavior can be observed for plasmonic nanoantennas, where its symmetry strongly impacts the absorption and nonlinear response. Researchers have shown, that for different excitation polarizations, different plasmon modes can be excited [76-79]. Taking into account, that the individual parts of the hybrid metasurfaces have individual symmetries on their own, a polarization-dependent behavior of the SHG is expected. If applications are to be developed in the future, the influence of symmetries and other properties on the process of SHG needs to be well-known. Thus, this chapter handles a fundamental study of how various plasmonic nanoantenna arrays with different plasmon modes influence the SHG if they are combined with single-crystalline 1L-WS₂ flakes. Hence, the most important parameters are modified and their impact on the SHG is recorded. In the following, the fundamental idea behind the combination of plasmonic nanoantenna arrays and 1L-TMDC is presented and it is explained, which parameters are of great importance when it comes to SHG in these hybrid metasurfaces. Subsequently, the fabrication process of the plasmonic nanoantenna arrays as well as their linear characterization is described in detail. Afterward, the experimental results of the SHG investigation for various parameters provide fundamental knowledge about the SHG, allowing further applications to be tailored. Note, that parts of this chapter are already published in [80].

3.1. SHG in hybrid metasurfaces

By comparing the two parts of the hybrid metasurface and their optical properties with each other, a few commonalities stand out. Both systems provide interactions with light in the same wavelength range from the visible up to the near-infrared (NIR). On the one hand, the plasmonic nanostructures provide a strong near-field enhancement and large scattering cross-sections and can be tailored for a wide range of applications [81, 82]. Meanwhile, 1L-TMDC, in general, are highly attractive materials for optical applications, since they have a direct band gap of up to 2 eV for 1L-WS₂ and simultaneously offer a high absorption of up to 15% for atomic layers of less than 1 nm thickness [25, 26]. By combining plasmonic nanostructures with 1L-TMDC, the resulting hybrid metasurface can provide an even stronger light-matter interaction, which makes them suitable for tailored light manipulation on subwavelength scales. As this work focuses on the nonlinear harmonic generation of second-order and light manipulation in this regime the coupling between the 1L-WS₂ and the plasmonic metasurface needs to be fully understood. Although some coupling effects are already reported [38, 83-85], the impact of their individual symmetries on the process of SHG is still largely unexplored.

It was shown in chapters 2.4.2 and 2.2.2, that the polarization state of the excitation light is a crucial parameter when it comes to SHG in both, plasmonic nanostructures and 1L-WS₂. This makes the polarization the first parameter as part of a set, which needs to be studied carefully. Further, plasmonic nanostructures provide certain plasmon modes (see chapter 2.1.2), which define the nanostructures' interaction with light, making them the second important parameter investigated in this work. It is expected, that these modes play a key role for the SHG in hybrid metasurfaces. As the SHG only occurs, if the inversion symmetry is broken, the influence of the symmetry of the plasmonic nanoantennas and 1L-WS₂ are of great interest. Since the symmetry of the 1L-WS₂ is fixed, the symmetry of the individual nanoantennas completes the set of the most important parameters and needs to be investigated carefully. Therefore, the fundamental study is sub-classified into three parts. The first part handles the polarization-dependent SHG signal of hybrid metasurfaces consisting of simple nanorods with a rotational C₂ symmetry, where different lattice structures impact the enhancement of SHG. The second part investigates, how shifted plasmonic resonances can enhance or attenuate the SHG signal, arising from hybrid metasurfaces, whereas the last part examines, how different nanoantenna symmetries impact the process of SHG in hybrid metasurfaces.

3.2. Fabrication process

At this point, the fabrication of the hybrid metasurfaces shall be illuminated. All upcoming hybrid metasurfaces investigated in this chapter are fabricated in the same way and only differ by their individual design. Before 1L-WS₂ can be transferred, the plasmonic nanoantennas need to be fabricated, which is done by standard electron beam lithography (EBL). In the first step, a glass substrate is coated with two layers of poly-methyl-methacrylate (PMMA) resist by spin-coating and is then baked at 170 °C on a hotplate for 3 minutes each subsequently. Thereby, the two layers of PMMA possess different electron beam (E-beam) sensitivities to support an easier lift-off process. Further, a conductive layer, named Electra, which is necessary for the electron beam lithography process to avoid charging of the sample, is spin-coated onto the resist layers and backed at 90 °C for 2 minutes. The baking processes are necessary for removing solvents from the PMMA and Electra. After the coating process, the plasmonic nanoantenna arrays are patterned into the resist by EBL. Afterward, the sample is put into a developer, which removes the PMMA of the areas exposed during the EBL process. Subsequently, an adhesion layer of 2 nm chromium is deposited onto the sample, followed by 30 nm of gold, which is done by electron beam evaporation. In the last step, the sample is put into acetone for a lift-off process, in which the PMMA is removed alongside most of the deposited metals, leaving the patterned nanoantenna arrays behind. If necessary, the lift-off process may be supported by a few seconds of ultrasonication. A schematic illustration of the individual steps for the plasmonic nanoantenna fabrication is shown in Figure 3.1.

After the fabrication of the plasmonic nanoantenna arrays, the 1L-WS₂ can be transferred. As it was described in chapter 2.3.1, a monolayer of WS₂ can be fabricated in two ways. Due to the fundamental analysis of the SHG arising from the hybrid metasurfaces in this chapter, the plasmonic nanoantenna arrays are covered with mechanically exfoliated 1L-WS₂. Although the size of the mechanically exfoliated monolayers is limited, their single-crystalline structure is more important than their size. The exfoliation and transfer of 1L-WS₂ onto the plasmonic nanoantenna arrays investigated in this chapter were done by Dr. Claudia Ruppert from the TU Dortmund. In a first step, 1L-WS₂ was exfoliated with commercially bought Nitto tape. To reduce the amount of glue residues from the tape, the 1L-WS₂ stuck to the tape is placed onto a piece of Polydimethylsiloxane (PDMS). This so-called PDMS-stamp then contains small areas of 1L-WS₂, which can be identified in a microscope. After this, the PDMS-stamp is mounted in an x-y-z-stage and placed above the substrate with the plasmonic nanoantenna arrays, which are fixed in its location. Subsequently, the PDMS-stamp is positioned precisely above the nanoantenna array and is until the PDMS-stamp hits the

sample surface. The lowering process is stopped if the monolayer WS_2 is fully in contact with the metasurface. After this, the PDMS-stamp is slowly raised again, to remove the 1L- WS_2 from the PDMS-stamp without introducing any strain or fissures until all of the PDMS-stamp is removed from the substrate. This raising process can be supported by a heating process of the substrate to temperatures of about 80-100 °C to facilitate the separating of the 1L- WS_2 from the stamp [86].

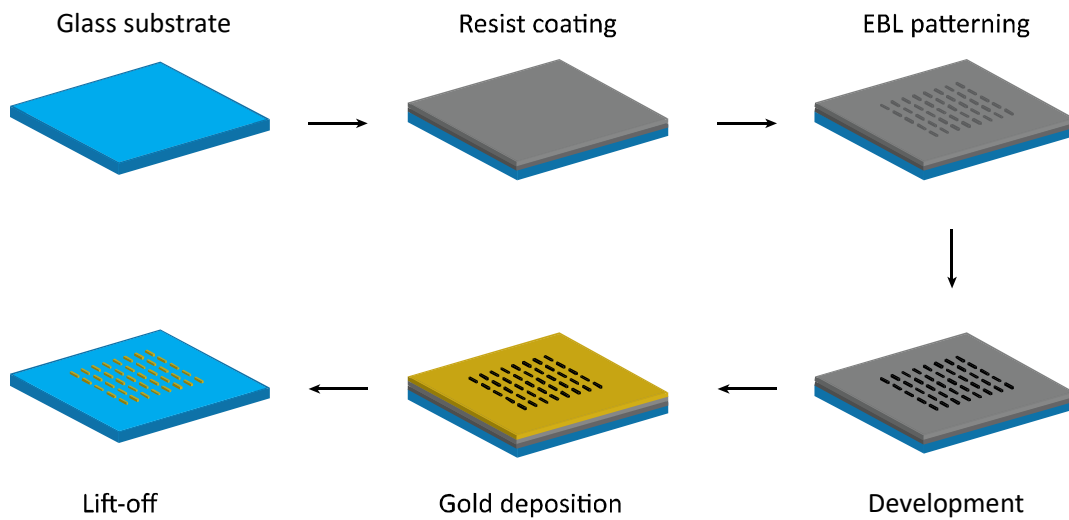


Figure 3.1 Fabrication process of the gold nanoantenna arrays. A cleaned glass substrate is spin-coated with two layers PMMA resist (70 nm and 150 nm) with different E-beam sensitivities. Afterward, the nanostructures are patterned into the resist by EBL. Subsequently, the exposed PMMA is removed in a development process and 2 nm of chromium, as well as 30 nm of gold, are deposited on top of the sample. In a last step, the remaining PMMA mask is removed in a lift-off process, which leaves the nanostructures on the glass surface behind.

3.3. Polarization-dependent SHG in hybrid metasurfaces

3.3.1. Design concept

To study the polarization dependency of plasmonic/TMDC hybrid metasurfaces, plasmonic nanoantenna arrays consisting of simple gold nanorods with a two-fold rotational C_2 symmetry are chosen (see Table 1). Since the inversion symmetry is not broken for simple nanorods, they can be approximated as subwavelength scale dipole antennas. Therefore, their impact on the SHG can be reduced to an analysis based on their plasmon resonances, while the measured SHG mainly originates at the 1L- WS_2 . In order to fully characterize the polarization-dependent SHG in such hybrid metasurfaces, the relative orientation between the nanorods long axis and the 1L- WS_2 lattice structure needs to be taken into account. Therefore, each hybrid metasurface is divided into four distinct areas. Each area consists of plasmonic nanorod arrays, where the individual nanorods are rotated by an angle α (see Figure 3.2). To further study any impact of the plasmonic lattice arrangement, three distinct samples are fabricated, wherein each sample contains a plasmonic nanoantenna array with a different lattice structure, namely a square, hexagonal and degenerated hexagonal lattice structure (Figure 3.2B-D).

In chapter 2.2.1 it was exemplified, that SHG can only be present if the inversion symmetry is broken. Although for plasmonic C_2 nanoantennas, as illustrated in Figure 3.2, this is not the case, it is possible to introduce a broken inversion symmetry with the help of the lattice structure. Therefore, the coupling between the individual nanorods to their next neighbors is utilized [87, 88]. Apparently, the square and hexagonal lattice (Figure 3.2) structures maintain the inversion symmetry, whereas the degenerated hexagonal lattice structure (Figure 3.2) possesses a unit cell similar to the hexagonal lattice structure, where the centered nanorod is missing, creating a new unit cell with broken inversion symmetry.

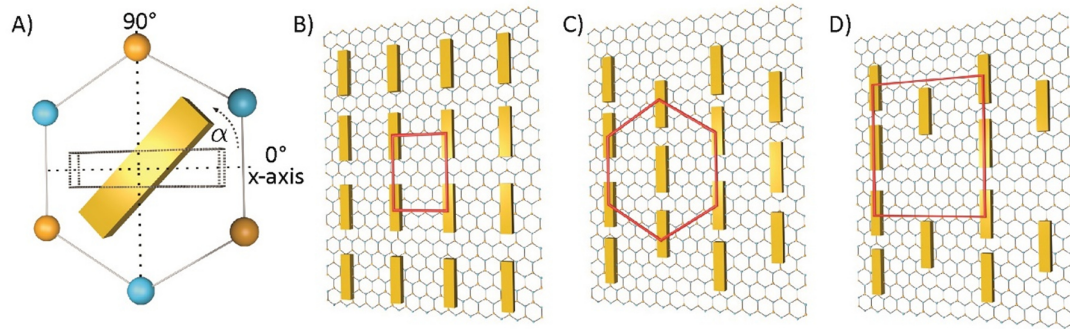


Figure 3.2: Hybrid metasurface for second-harmonic generation. (A) Relative rotation angle between plasmonic nanoantenna and the hexagonal lattice structure of the WS_2 for 45° - 90° in 15° steps. The horizontal dotted line indicates the angle of 0° with respect to the hexagonal lattice structure. The blue and orange spheres represent the W and S atoms arranged in a hexagonal lattice. **(B-D)** Schematic illustration of the nanoantennas arranged in a square (B), hexagonal (C), and degenerated hexagonal (D) lattice structure. The red lines represent the unit cells for each lattice structure. The 1L- WS_2 layer depicted in these images lays on top of the nanoantenna arrays. A similar image can be found in [80].

3.3.2. Linear optical characterization

For a fundamental study, each of the presented plasmonic lattice structures, illustrated in Figure 3.2B-D, is fabricated twice, where one of each is covered by a monolayer of WS_2 and the second one is left bare. In this way, a comparison of the SHG between a hybrid metasurface and bare plasmonic metasurface as a reference is possible. The nanorods dimensions are chosen to be 300 nm in length, 100 nm in width and 30 nm in height. This results in a plasmon resonance at a fundamental wavelength of around 1230 nm, which equals half of the band gap energy of ~ 2 eV ($\triangleq 615$ nm) for 1L- WS_2 . As a strong SHG is expected for 1L- WS_2 at this fundamental wavelength, the plasmon resonance, therefore, can couple to this wavelength resonantly.

After the six plasmonic nanoantenna arrays were fabricated by the process, described in chapter 3.2, scanning electron microscopy (SEM) images were taken and the linear optical properties of the nanoantennas were checked to ensure, that their plasmon resonances are suiting the design wavelength and the different parametric studies provide reliable results about the SHG in plasmonic-TMDC hybrid metasurfaces. To determine the plasmon resonance of the freshly fabricated plasmonic nanoantenna

arrays, their transmission spectra were measured via Fourier-transform infrared spectroscopy. This was done with a Bruker Vertex 70 spectrometer and a Bruker Hyperion 1000 IR-microscope, which is equipped with a knife-edge aperture to measure an exclusively small area, e.g. a plasmonic nanoantenna array [89]. The transmitted light was collected by a Schwarzschild microscope objective (x36/0.5) and focused onto an Indium-Gallium-Arsenide (InGaAs-) detector. The measured spectrum was divided by a reference spectrum, which was taken for pure glass substrate to calculate the relative transmittance T . Figure 3.3A-C shows SEM images of three different plasmonic nanoantenna arrays, whereas Figure 3.3D provides the corresponding transmission spectra.

As Figure 3.3 prove, the fabricated plasmonic nanoantenna arrays have the correct dimensions providing the intended plasmon resonances at around 1230 nm (Figure 3.3), which fit half of the band gap energy of 1L-WS₂. The dip in the transmission spectra slightly varies between the different fields in width, depth and position. This variation can be explained by the different lattice structures in each metasurface. Previous studies have shown, that the coupling between nanostructures changes with a changed lattice structure, resulting in slightly different transmission spectra [90]. Note, that the transmission spectra were taken from the different types of lattice structures for all antenna rotations from 45-90°.

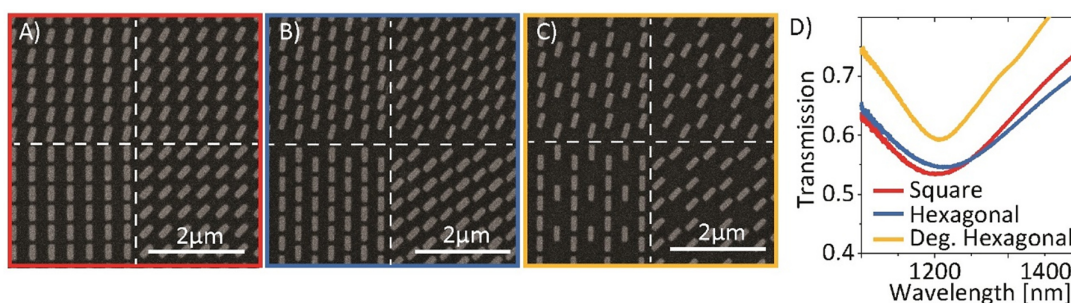


Figure 3.3: Characterization of plasmonic nanoantenna arrays. (A-C) SEM images of plasmonic nanoantenna arrays with a square (A), hexagonal (B) and degenerated hexagonal (C) lattice structure. Each metasurface contains four distinct areas, wherein each area the individual nanorods are rotated in steps of 15°. **(D)** Transmission spectra of the plasmonic metasurfaces, measured with unpolarized light. Note that the color-coding of (D) matches the frame color in A-C. A similar image can be found in [80].

After the characterization, the 1L-WS₂ is transferred on top of the plasmonic nanoantenna arrays. White-light images, as well as PL-images of the hybrid metasurfaces, are shown in Figure 3.3A-C. To confirm, that the transfer onto the

nanoantenna arrays was successful and the transferred WS_2 is of monolayer thickness, a PL-measurement is done. Therefore, the setup, illustrated in Figure 2.12, is used to determine, whether the monolayer is damaged or distorted. Figure 3.3D shows the measured PL-spectra, where a strong peak at 613 nm with a linewidth of 10 nm is observed for all samples, confirming, that the transferred WS_2 layers are indeed of monolayer thickness. By comparing the PL-emission wavelength to the plasmon resonances of the nanoantenna arrays (Figure 3.3D), a good overlap can be confirmed.

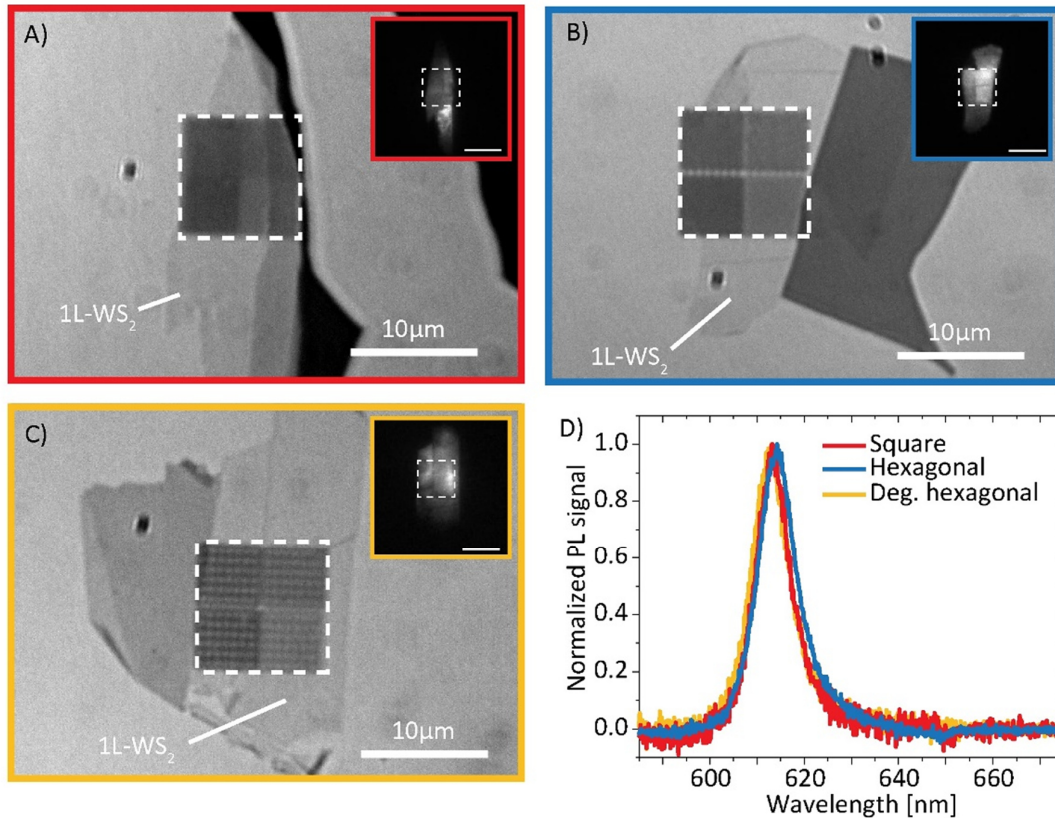


Figure 3.4: Photoluminescence measurements. (A-C) Optical microscopy images of the plasmonic nanoantenna arrays with the square (A), hexagonal (B), and degenerated hexagonal (C) lattice structure, covered with a 1L- WS_2 as indicated. The white dotted line marks the hybrid metasurface. The insets of these images show PL-images of the same areas, where also the white dotted line marks the hybrid metasurface. The scale bar represents 10 μm . (D) Normalized photoluminescence spectra of the three monolayers from (A-C) showing a clear peak at 613 nm indicating a band gap energy of ~ 2 eV. A similar image can be found in [80].

3.3.3. Nonlinear optical characterization

After the linear optical characterization, the wavelength-dependency of the SHG was analyzed. For this, the SHG signals arising from the individual parts of the hybrid metasurface, the bare plasmonic metasurface and solely 1L-WS₂, were measured independently from each other. Note, that for the characterization of the SHG of bare plasmonic nanoantenna arrays, only the SHG arising from nanoantenna array arranged in a degenerated hexagonal lattice structure was measured, where the inversion symmetry is broken. Since the other two lattice structures have present inversion symmetry, no SHG is expected for these metasurfaces. For this measurement, a home-build microscopy setup was used, which is depicted in Figure 3.5A. As a fundamental light source, laser pulses with a pulse length of about 60 fs at peak wavelengths ranging from 1200-1290 nm varied in 10 nm steps and emitted by an optical parametric amplifier system at a 1 MHz repetition rate were used. The excitation polarization state was set by a combination of a linear polarizer and a half-wave plate. After the laser beam was filtered by a long pass (LP), it was focused down by a microscope objective down to a spot size of ~2 μm in diameter (full width at half maximum). The beam passed the substrate first and illuminated the nanorods (or 1L-WS₂) on the backside of the sample afterward. In the case of the hybrid metasurfaces, the plasmonic nanostructures were excited first and the 1L-WS₂ subsequently. The SHG signals, generated by either 1L-WS₂ or plasmonic nanoantenna arrays, were collected by another microscope objective and filtered by a short pass (SP) and another linear polarizer. As it was shown in chapter 2.4.2, that the SHG of 1L-WS₂ strongly depends on the polarization state. Therefore, the output linear polarizer was set to be parallel to the input polarization state at all times. The filtered SHG signal was then focused onto the inlet of a spectrometer, consisting of an Andor Shamrock monochromator with a 300 l/mm grid (Blaze 500 nm) and an Andor Newton CCD camera.

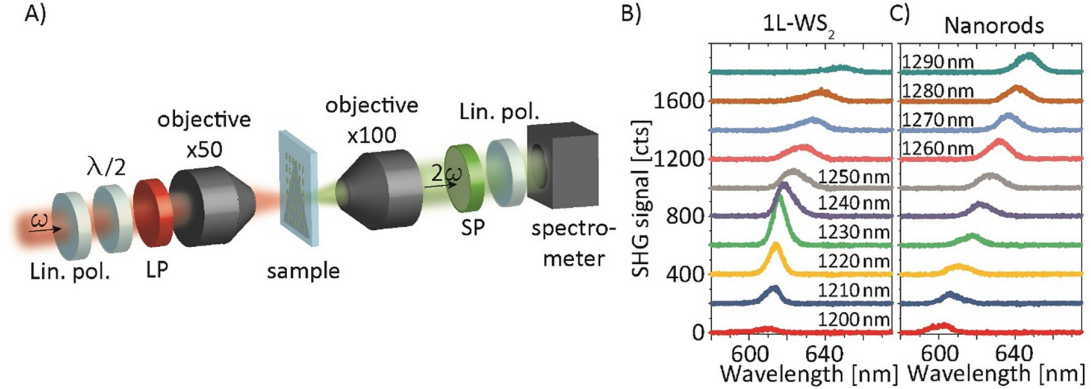


Figure 3.5: Wavelength-dependent SHG signals. (A) Schematic illustration of the setup for SHG measurement. The fundamental infrared laser beam first was linearly polarized, filtered by a long pass (LP) and then focused by a microscope objective (x50/NA 0.42) onto the backside of the sample. The input polarization was set by a linear polarizer (Lin. Pol.) and a half-wave plate. The SHG signal was collected by another microscope objective (x100/NA 0.8), filtered by a short pass (SP) and another linear polarizer and measured by a spectrometer. **(B)** Measured SHG signal of solely 1L-WS₂ for different excitation wavelengths. **(C)** Measured SHG signal of bare plasmonic nanoantenna arrays arranged for the degenerated hexagonal lattice structure and different excitation wavelengths. The input polarization was set to be alongside the nanorods long axis. Note that each spectrum is labeled with its excitation wavelength inside B) or C) and shifted upwards for better visibility. A similar image can be found in [80].

The measured results of the wavelength-dependent SHG for bare plasmonic metasurface and solely 1L-WS₂ are shown in Figure 3.5B-C. For solely 1L-WS₂, the SHG signal becomes strongest, when it is excited with a wavelength of 1230 nm. This observation consents with the results of the PL-measurements, which exhibit a band gap energy equal to 613 nm. Usually, the SHG signal is located at wavelengths equal to half of the excitation wavelength. For excitation wavelengths shorter than 1230 nm, this does not hold true anymore. The nonlinear signal rather converges against 613 nm, which hints that the primary nonlinear process is not SHG anymore, but rather a two-photon luminescence (TPL) [35, 91]. This effect occurs, when the summed up energy of two absorbed photons is higher than the band gap energy of the absorbing material. At once, the energy of one of the absorbed photons is still too lower than the band gap energy. If these requirements are fulfilled, an electron is excited into the conduction band of the material, where it relaxes to the minimum of the conduction band after a short time. This process is similar to the direct excitation for PL-measurements, described in chapter 2.4.1. After the excited electron recombines with the leftover hole in the valance band, it releases its energy in form of a photon with an energy equal the band gap energy of the material [92, 93]. In this way, the TPL-signal shows a peak at an

energy equal to 613 nm, as visible in Figure 3.5B. A closer investigation of this process is discussed later in this thesis. Compared to the SHG signals of solely 1L-WS₂, the strongest nonlinear signal arising from bare plasmonic nanoantenna arrays (see Figure 3.5C) cannot be easily identified. This can be reasoned with quite broad plasmon resonance (Figure 3.3D), which leads to a broad wavelength range for SHG. Another difference to the SHG arising from solely 1L-WS₂ appears if the locations of the nonlinear signals are compared. For wavelengths below 1230 nm, the SHG signals are always located at half of the excitation wavelength, which refers to a pure SHG process and no TPL. Based on the results obtained for the 1L-WS₂ and bare plasmonic nanoantenna arrays, the upcoming polarization-dependent SHG measurements are done with a wavelength of 1230 nm.

3.3.4. Symmetry effects on nonlinear harmonic generation

After the linear and nonlinear optical characterization of the individual parts of the hybrid metasurface, the polarization dependency of the SHG is studied to determine the influence of the coupling effects between the nanoantennas and the 1L-WS₂ on the SHG. During the transfer process of the 1L-WS₂, the absolute orientation of its hexagonal lattice structure with respect to the nanorods' long axis cannot be precisely measured, as it is constituted in Figure 3.2A. Therefore, small variations from the during the alignment are unpreventable and the relative orientation between the 1L-WS₂ and the nanorods' long axis deviates from the intended angles. Note, that the x-axis, as it is illustrated in Figure 3.2A, represents an angle of $\alpha = 0^\circ$, which is chosen with respect to the hexagonal lattice structure of the 1L-WS₂.

Nevertheless, the absolute value of the relative orientation between the 1L-WS₂ (or x-axis) and the nanorods' long axis needs to be determined. This determination is done by measuring the polarization-dependent nonlinear signals of the 1L-WS₂ and the plasmonic nanoantenna arrays. To determine the orientation of the 1L-WS₂ hexagonal lattice structure, the polarization-dependent second-harmonic generation is measured, allowing a precise determination of the x-axis (see chapter 2.4.2). In the case of the plasmonic nanorods, the determination of their long axis' orientation is a more difficult problem. Due to the present inversion symmetry in two out of three plasmonic nanoantenna arrays, no SHG is expected for these plasmonic metasurfaces. Therefore, the polarization-dependent third-harmonic generation is measured for the plasmonic nanoantenna arrays arranged in a square and hexagonal lattice structure. Previous studies have shown, that the THG of plasmonic nanorods also exhibits a strong polarization dependency [94]. Note, that for the degenerated hexagonal lattice

structure, the polarization-dependent SHG signal is measured again to determine the orientation of the nanorods' long axis. For the polarization-dependent nonlinear measurements, the same setup (Figure 3.5A) is used, where the input polarization is varied from 0-180° in 4° steps and the output polarizer is parallel to the input polarization at all times. The nonlinear signals are spectrally integrated and represent the SHG/THG signal for each input polarization angle. The results are illustrated in Figure 3.6.

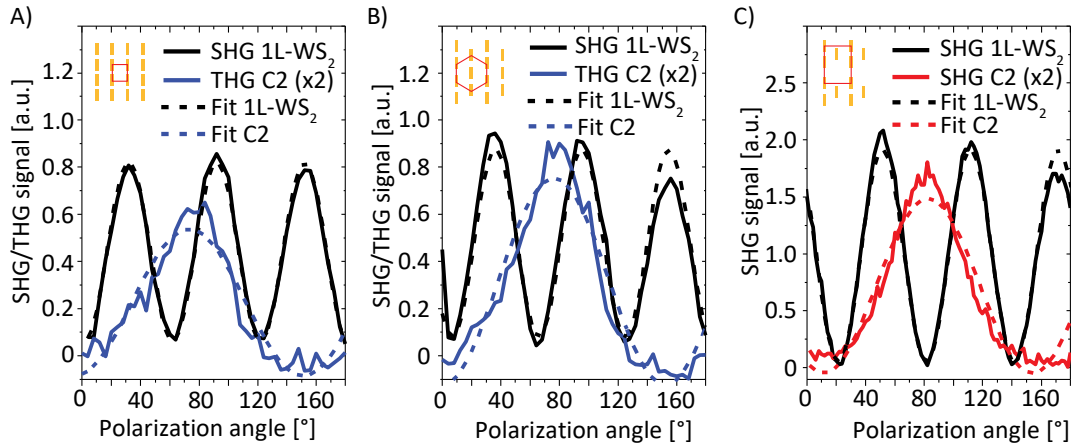


Figure 3.6: Determination of relative angles between C2 antenna and WS₂. (A) Polarization-dependent nonlinear signals of 1L-WS₂ and C2 nanoantenna arrays arranged in a square lattice in dependency of the polarization angle. The rotation angle of the 1L-WS₂ is determined to 2° while the rotation angle of the C2 antenna is determined to 73°, which results in a relative rotation angle between both systems of 71°. (B) Polarization-dependent nonlinear signals of 1L-WS₂ and C2 nanoantenna arrays arranged in a hexagonal lattice in dependency of the polarization angle. The rotation angle of the 1L-WS₂ is determined to 7° while the rotation angle of the C2 antenna is determined to 76°, which results in a relative rotation angle between both systems of 69°. (C) SHG signals of 1L-WS₂ and C2 nanoantenna arrays arranged in a degenerated hexagonal lattice in dependency of the polarization angle. The rotation angle of the 1L-WS₂ is determined to 22° while the rotation angle of the C2 antenna is determined to 82°, which results in a relative rotation angle between both systems of 60°. Note that all data, labeled with (x2), are multiplied with a factor of 2 for better visibility. The insets show a schematic illustration of the lattice structure of the corresponding plasmonic nanoantenna array. A similar image can be found in [80].

The results of the polarization-dependent nonlinear measurements allow a clear determination of the relative orientations between the 1L-WS₂ and plasmonic nanorods. First, the relative orientation angle $\theta_{C_{WS_2}}$ of the 1L-WS₂ is determined. The polarization-dependent SHG of the 1L-WS₂ shows the same behavior for each sample with three distinct peaks, which is in good accordance to the results shown previously in Figure 2.13. Thus, the calculation of the orientation angle can be done with help of the equation $I_{2\omega} \propto \cos^2(3\theta + \theta_{C_{WS_2}})$, where θ represents the polarization angle. In comparison to this, the measured polarization-dependent nonlinear signals of the plasmonic nanorods shows only one peak, which is expected due to the two-fold rotational symmetry of the plasmonic nanorods. Thus, the particular orientation angles of the nanorods θ_C are calculated by the fit function $A \cdot \sin^2\left(\pi \frac{\theta - \theta_C}{w}\right) + A_0$, where θ represents the polarization angle, A & A_0 are the fit parameters regarding the amplitude and offset and w corresponds to the period. As of only important information regarding these results is the relative orientation angle θ_C , Table 2 provides the obtained values for all three hybrid metasurfaces.

Lattice structure	$\theta_{C_{C2}}$	$\theta_{C_{WS_2}}$	$\theta_{C_{C2}} - \theta_{C_{WS_2}}$
Square	73°	2°	71°
Hexagonal	76°	7°	69°
Degenerated hexagonal	82°	22°	60°

Table 2: Orientation angles of 1L-WS₂ ($\theta_{C_{C2}}$) and plasmonic C2 nanoantennas ($\theta_{C_{WS_2}}$) determined from polarization-dependent measurement, shown in Figure 3.6. A similar table can be found in [80].

After the determination of the relative orientation angles, the polarization-dependent SHG of bare plasmonic nanoantenna arrays without 1L-WS₂ on top is measured. Note, that the upcoming results provide graphs, where the x-axes labeled with ‘Polarization angle’ are related to the orientation of the individual transferred 1L-WS₂. Therefore, the same orientations of the plasmonic nanoantennas, presented in Figure 3.3A-C will have slightly different orientation angles with respect to the particular transferred 1L-WS₂. The results for the three different lattice structures are shown in Figure 3.7. The denoted rotation angles of the nanorods for each nanoantenna array are already given in respect to the x-axis as assigned in Figure 3.2A, which is possible because the bare plasmonic nanoantenna arrays were fabricated on the same substrate as the hybrid metasurfaces. For the square lattice (Figure 3.7A) almost no SHG signal can be observed for any polarization angle, except for the plasmonic nanorods, rotated by 56° in the 1L-WS₂ reference frame. For these nanorods, a small increase of the SHG signal is visible. These

results are comparable to the SHG signals arising from the hexagonal lattice structure where also almost no SHG signal is observable (Figure 3.7B). The absence of SHG in these nanoantenna arrays can be explained by the present inversion symmetry in the C2 nanorod and the lattice arrangement. The comparatively low SHG signals, which are observable for these polarization angles, are more likely to be caused by small surface impurities, originating from a non-perfect fabrication process so that a perfect inversion symmetry is not given. In addition, the comparatively small laser spot can lead to a small SHG signal when it is not perfectly aligned with a symmetry point of the nanoantenna array's lattice structure, leading to an imperfect cancellation of SHG from different locations.

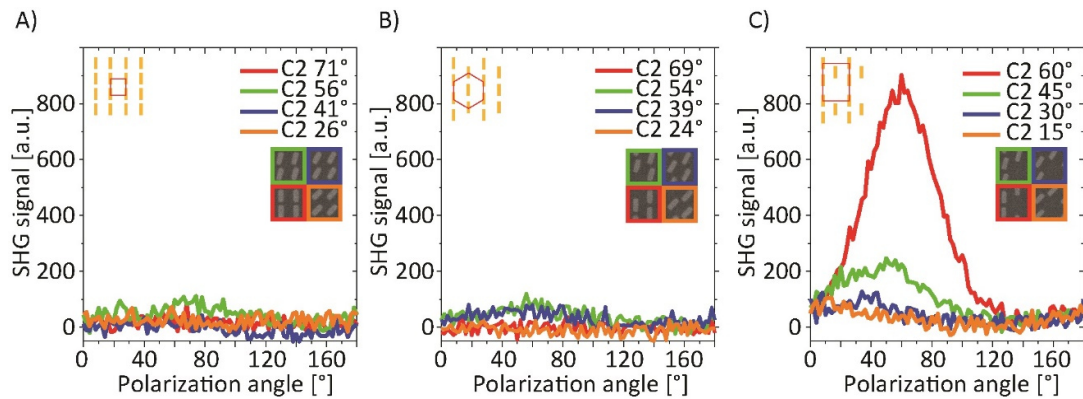


Figure 3.7: Nonlinear optical measurements of plasmonic metasurfaces without the 1L-WS₂. Polarization-dependent SHG signals of plasmonic metasurfaces with a square (A), hexagonal (B), and degenerated hexagonal (C) lattice structure. The lower right insets show SEM images of the plasmonic nanoantenna arrays corresponding to the rotation angle of the individual nanorods labeled by the same color, while the upper left insets indicate the related lattice structure of the plasmonic nanorods. A similar image can be found in [80].

By looking at the polarization-dependent SHG signals for the degenerated hexagonal lattice structure (Figure 3.7C), strong SHG signals can be observed, which is expected, since the inversion symmetry is broken for this lattice structure. The SHG signal becomes strongest for the antenna rotation of 60° under an illumination polarization angle, which coincides with the nanorods' long axis under this very angle. For the other antenna rotation angles, the SHG signals also become strongest, when the nanorods are excited resonantly along their long axis, exhibiting a smaller signal strength. However, they are still stronger than the signals, arising from the plasmonic nanoantenna arrays arranged in the square and hexagonal arrangement. Since the measured SHG signals originate from the lattice structure in its entirety, the coupling between the individual nanorods

plays an important role, when it comes to SHG. The lower SHG signals for smaller antenna rotation angles can be justified with a weaker coupling between the individual nanorods. This is supported by a polarization-dependent transmission measurement done at the excitation wavelength of 1230 nm. Figure 3.8 illustrates, that for smaller antenna rotation angles a higher transmission is measured, which indicates a smaller coupling between the individual nanorods.

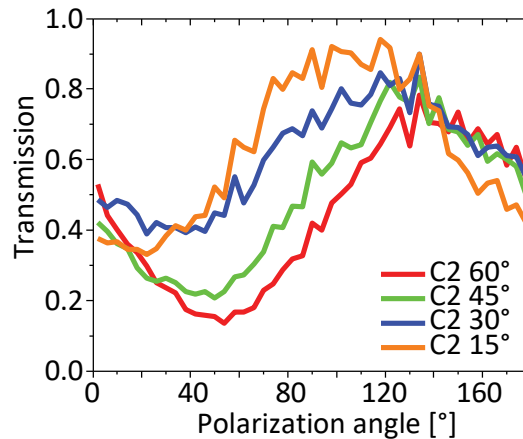


Figure 3.8: Polarization-dependent transmission for 1230 nm excitation wavelength measured from the plasmonic nanoantenna arrays arranged in a degenerated hexagonal lattice structure. A similar image can be found in [80].

3.3.5. Linear polarization dependency

After characterizing the nonlinear responses of second-order for the two components of the hybrid metasurface independently from each other, it is now time for the discussion about the polarization-dependent SHG for the combined hybrid structure. Therefore, the measurement has been repeated on the hybrid metasurfaces, consisting of the three different plasmonic nanoantenna arrays with different lattice arrangements covered with a monolayer WS_2 . The results are shown in Figure 3.9. For better visualization, Figure 3.9A-C illustrates the relative orientation angles between the 1L- WS_2 hexagonal lattice structure and the individual rotation angles of the fabricated nanorods for each lattice arrangement.

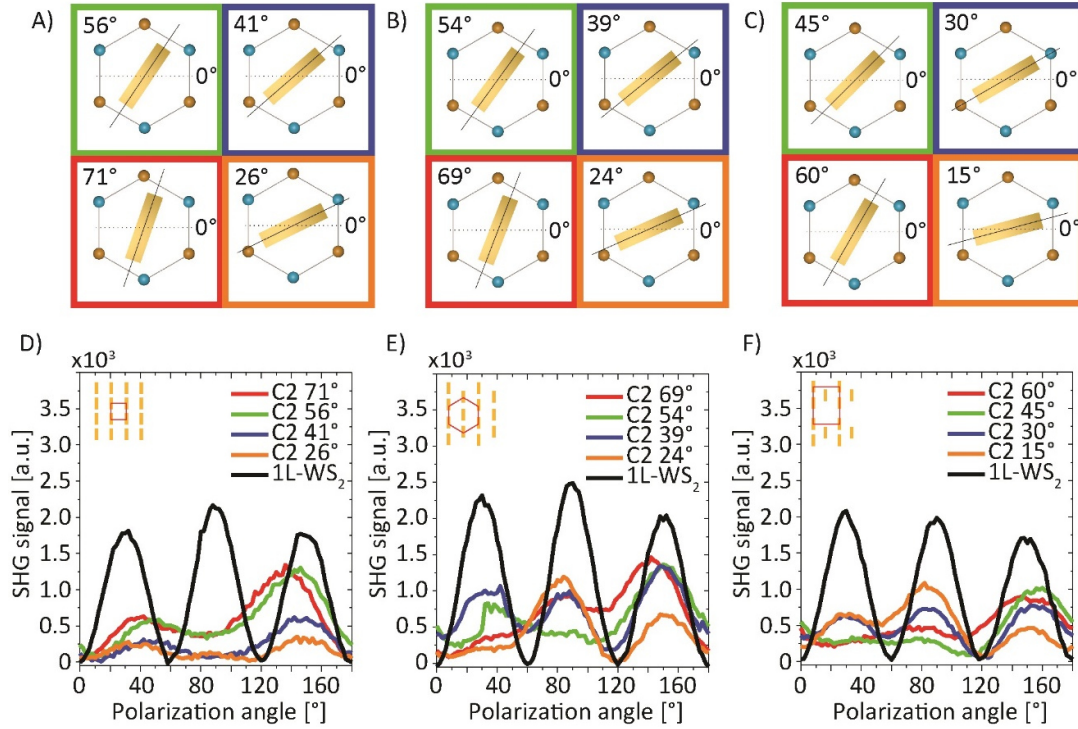


Figure 3.9: Polarization-dependent SHG signals of the hybrid metasurfaces including the 1L- WS_2 . (A-C) Schematic illustrations of the relative orientations between the plasmonic nanorods and the hexagonal lattice structure of the 1L- WS_2 for the square (A), hexagonal (B), and degenerated hexagonal (C) lattice structure. (D-F) Polarization-dependent SHG signals of hybrid metasurfaces with plasmonic nanoantenna arrays arranged in a square (D), hexagonal (E), and degenerated hexagonal (F) lattice structure. While the color code matches the marked colors in Figure 3.7, the black data represents the polarization-dependent SHG signal of bare 1L- WS_2 . Note that the insets indicate the related lattice structure of the plasmonic nanoantenna array. A similar image can be found in [80].

By looking at the results of the hybrid metasurface based on the plasmonic nanoantenna array with a square lattice (Figure 3.9D), the polarization-dependent SHG signals differ from the SHG signals arising from its individual parts solely, the 1L- WS_2 (black line) and bare plasmonic nanoantenna array (Figure 3.7A). First of all, the strength of the SHG is much greater than the SHG of the bare plasmonic nanoantenna array. Second, the SHG signal seems to be mainly determined by the 1L- WS_2 and becomes almost as strong as for solely 1L- WS_2 (black data) for greater polarization angles. This states, that the plasmonic part of the hybrid system only contributes weakly to the SHG signal and might even attenuate it. The data shows, that the SHG signal of the hybrid metasurface becomes stronger, if the polarization angle coincides with a mirror axis of the 1L- WS_2 ,

where a maximum in SHG signal is observable, e.g. $\sim 150^\circ$. Although the signal strength is lower than for a polarization angle of 150° , a second maximum at $\sim 30^\circ$ can be found. This observation can be explained by the relative orientation of the individual nanorods. The more the long axis of the nanorods coincides with a symmetry axis of the 1L-WS₂ hexagonal lattice structure, where usually a maximum in SHG is expected, the more the plasmon resonance of the nanorods is excited by the fundamental wave, which results in a smaller amount of light participating in the process of SHG in the 1L-WS₂. It can therefore be said, that the SHG signal decreases when the long axis of the nanorods comes closer to a symmetry axis of the 1L-WS₂.

The hybrid metasurface with plasmonic nanoantenna arrays arranged in a hexagonal lattice structure shows a similar behavior compared to the square lattice structure. The SHG signal becomes strongest when the polarization angle coincides with a 1L-WS₂ symmetry axis and a nanorods short axis, which is the case for 90° and 150° . The resemblance to the results of the square lattice structure is not surprising since the inversion symmetry is still given for this lattice arrangement. Hence, the SHG signal is still mainly determined by the 1L-WS₂. This changes, when the hybrid metasurface with plasmonic nanoantennas arranged in a degenerated hexagonal lattice structure is considered. The previously obtained polarization-dependent SHG signals for this bare nanoantenna array, illustrated in Figure 3.7C, have shown, that for these arrays an SHG signal can be measured if the nanorods are excited resonantly. When combined with a monolayer WS₂, a participation to the SHG signal is expected. By looking at the results, this seems not the case. The polarization-dependent SHG signals resemble the other hybrid metasurfaces discussed previously, where the strongest signals are again observable at 90° and 150° . Although the SHG is allowed for this plasmonic nanoantenna array due to the present inversion symmetry peaking at e.g. 60° , a lower signal strength is observed for the hybrid metasurface case, where no additional local maximum is formed. Compared to the results of the other hybrid metasurfaces, it stands out that the SHG signals are mainly determined by the 1L-WS₂ forming local maxima alongside a 1L-WS₂ mirror axis at 30° , 90° and 150° although the signal strength at these angles is always lower than the SHG measured for solely 1L-WS₂.

3.3.6. Modeling the SHG of hybrid metasurfaces

To support the experimental results, a theoretical analysis has been done. To model the nonlinear optical response of the hybrid metasurface, it is split into two parts, the linear transmission of the plasmonic nanorods and the nonlinear process of SHG in the 1L-WS₂. For this model, the same setup configuration as in the experiments is considered

described in chapter 3.3.3. In a first step, the transmitted electric field after the plasmonic nanorods is calculated. In accordance with the experiment, a linear polarized electric field at normal incidence (z-direction) rotated by the angle θ only having E-field components in the xy-plane is considered, given by

$$\vec{E}_{in} = E_0 \begin{pmatrix} \cos \theta \\ \sin \theta \end{pmatrix}. \quad (3.1)$$

A common approach to describe the behavior of polarized light in optics is the usage of the Jones calculus, where linear optical elements are represented by individual Jones matrices [95]. The Jones matrix of the plasmonic nanorods, which are rotated by the angle α can be written as [96]

$$J(\alpha) = \begin{bmatrix} \cos \alpha & -\sin \alpha \\ \sin \alpha & \cos \alpha \end{bmatrix} \begin{bmatrix} t_x & 0 \\ 0 & t_y \end{bmatrix} \begin{bmatrix} \cos \alpha & \sin \alpha \\ -\sin \alpha & \cos \alpha \end{bmatrix}, \quad (3.2)$$

where the outer matrices describe the rotation of the nanorod and the matrix in between describes the nanorods' transmission behavior. The Jones matrix is used to calculate the transmitted electric field:

$$\begin{aligned} \vec{E}_{trans} &= J(\alpha) \vec{E}_{in} \\ &= E_0 \left[\cos \alpha \sin \alpha (t_x - t_y) \begin{pmatrix} \sin \theta \\ \cos \theta \end{pmatrix} + \begin{pmatrix} \cos \theta (t_x \cos^2 \alpha + t_y \sin^2 \alpha) \\ \sin \theta (t_y \cos^2 \alpha + t_x \sin^2 \alpha) \end{pmatrix} \right]. \end{aligned} \quad (3.3)$$

Here, t_x and t_y represent the transmission coefficients of the plasmonic nanorods and in respect to its long and short axis. The transmission coefficient t_x is chosen to $t_x = 0.5$ (based on the experimental results from Figure 3.8) and $t_y = e^{i\Delta\phi}$, where a phase shift $\Delta\phi$ for the consideration of the nanorods thickness of 30nm needs to be taken into account. For the determination of this phase shift, the E-field components parallel to the short and long axis of an excited nanorod are simulated with the help of CST Studio Suite (see Figure 3.10A). Subsequently, the phase values for the two E-field components are extracted from the simulation results for various distances behind nanorods, as illustrated in Figure 3.10B. All phase values are taken for the same point in time so that the phase differences between the two E-field components can finally be calculated to $\Delta\phi = 0.23\pi$.

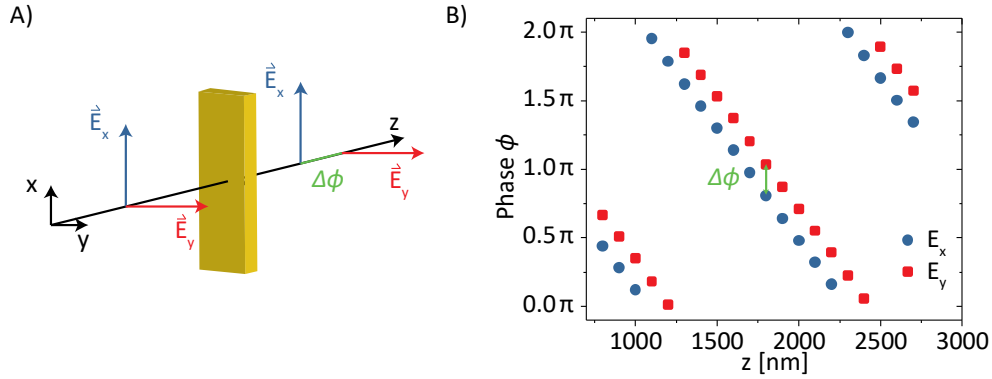


Figure 3.10: Phase shift determination (A) Schematic illustration of the transmitted E-field components parallel to the long and short axis of the plasmonic nanorod. **(B)** Obtained phase values for the two E-field components.

As equation (3.3) provides an expression for the transmitted electric field components in the xy-plane, the SHG in 1L-WS₂ can be calculated. Therefore, the total E-field after the plasmonic nanorods is described by

$$\vec{E}_{C2} = \begin{pmatrix} E_{trans,x} \\ E_{trans,y} \\ 0 \end{pmatrix}. \quad (3.4)$$

Since the 1L-WS₂ belongs to the D_{3h} point symmetry group and the non-zero elements of the second-order susceptibility tensor $\chi^{(2)}$ of 1L-WS₂ were already stated in chapter 2.4.2, the second-order polarization can be calculated to

$$\vec{P}^{(2)} = \varepsilon_0 \chi^{(2)} \vec{E}_{C2}^2 = \varepsilon_0 \chi_{yyy}^{(2)} \cdot \begin{pmatrix} -2 \cdot E_{trans,x} \cdot E_{trans,y} \\ E_{trans,y}^2 - E_{trans,x}^2 \\ 0 \end{pmatrix}. \quad (3.5)$$

Afterward, the second-order polarization can finally be used, to calculate the intensity of the SHG with the same polarization as the incident E-field, which corresponds to the measured SHG in the experiment. It is done by

$$I_{\parallel}^{SHG} = \frac{c_0}{2 \cdot \varepsilon_0} \cdot \left| \vec{P}^{(2)} \cdot \begin{pmatrix} \cos \theta \\ \sin \theta \end{pmatrix} \right|^2. \quad (3.6)$$

With the help of equation (3.6), the polarization-dependent SHG signals can be calculated. The theoretical results are shown in Figure 3.11, which are calculated with respect to the experimentally determined rotation angles of the plasmonic nanorods. By looking at the theoretical results, shown in Figure 3.11, it stands out, that the three predominant local maxima arising from the hexagonal lattice structure of the 1L-WS₂ are still visible for the polarization angles of 30°, 90° and 150°. Further, these maxima underlie small spectral shifts, which are also visible in the experimental results (see Figure 3.9D-F). The most important observation made from the theoretical results regards the relative SHG intensities for polarization angles. If the nanoantenna is excited more resonantly, the SHG strength at polarization channels, where usually a strong SHG signal is expected, is attenuated. Note, that these theoretical calculations only consider the impact of the plasmonic nanorods and neglect any lattice interactions between individual nanorods or further coupling between the 1L-WS₂ and the nanorods. Nevertheless, the presented theoretical results provide a solid approach to model the SHG in the investigated hybrid metasurfaces, which match the experimental results shown in Figure 3.9D-F.

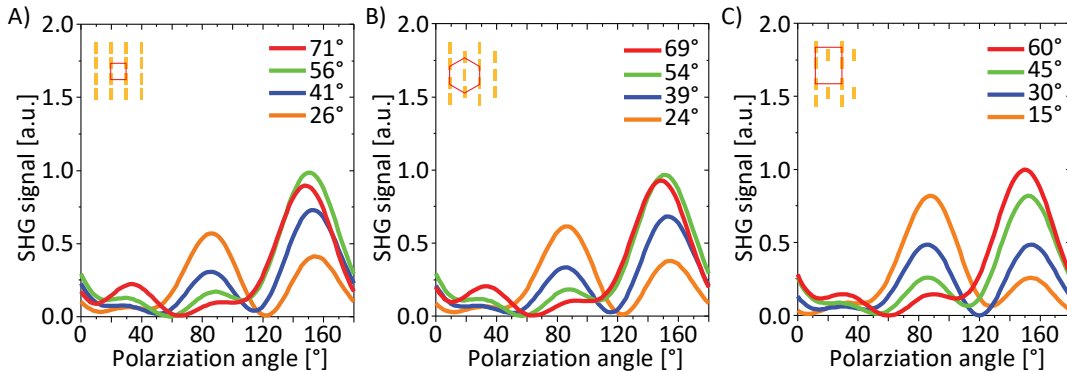


Figure 3.11 SHG simulation of the SHG signals arising from hybrid metasurfaces. (A-C) Calculated polarization-dependent SHG signals of hybrid metasurfaces with plasmonic nanoantennas rotated by the denoted rotation angles α for the square (A), hexagonal (B), and degenerated hexagonal (C) lattice structure. Note, that the color code matches the marked colors in Figure 3.9(D-F) and that the absolute values are not comparable to the values, shown in the experimental results. A similar image can be found in [80].

3.3.7. Enhanced second-harmonic generation

Although no overall enhancement for the SHG generation in plasmonic/TMD hybrid metasurfaces is observed, a closer look at the results exhibits a strong enhancement for certain polarization angles. As it was previously concluded, that the SHG in these hybrid metasurfaces is mainly determined by the 1L-WS₂, the theoretical model (Figure 3.11) and the experimental data (Figure 3.9) of the polarization-dependent SHG signals in hybrid metasurfaces show comparatively strong SHG signals for polarization angles of 0°, 60° and 120°, where no SHG is expected for 1L-WS₂ at all. This hints, that the plasmonic nanorods as part of such hybrid metasurfaces provide a channel for SHG into polarization states, that are usually forbidden for either 1L-WS₂ or the presented bare plasmonic metasurfaces. To quantify this increase of SHG in these polarization states, the enhancement factor

$$\varepsilon_{SHG} = \frac{SHG_{hybrid}}{SHG_{PNA} + SHG_{1L-WS_2}} \quad (3.7)$$

is introduced. Hereby, SHG_{hybrid} , SHG_{PNA} and SHG_{1L-WS_2} are the polarization-dependent absolute SHG signals, measured for the hybrid metasurfaces, plasmonic nanoantenna arrays (PNA) and 1L-WS₂, respectively. The results are shown in Figure 3.12.

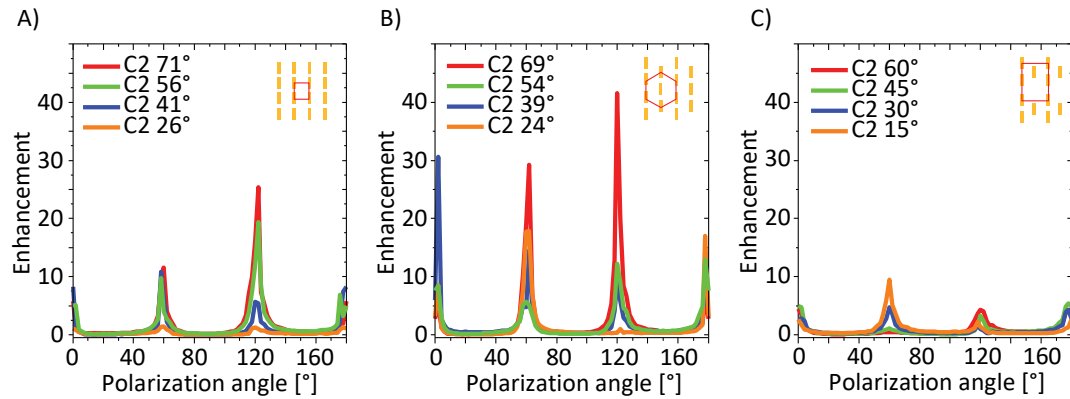


Figure 3.12 Enhancement factors of SHG for hybrid metasurfaces. (A-C) Polarization-dependent enhancement ε_{SHG} for the hybrid metasurface with plasmonic nanorods arranged in a square (A), hexagonal (B), and degenerated hexagonal (C) lattice structure for different orientations of the nanoantennas. The insets in each plot indicate the related lattice structure of the plasmonic nanorod array. A similar image can be found in [80].

The calculations show, that the polarization-dependent enhancement factors peak at the polarization angles of 0° , 60° and 120° , where usually no SHG signals are expected for 1L-WS₂. Further, no enhancement for the polarization angles in-between but only attenuation is observed. This behavior is visible for all presented hybrid metasurfaces regardless of their lattice structure of the plasmonic nanoantenna array. By comparing the absolute values of the enhancements among the three different plasmonic nanoantenna arrangements, the hybrid metasurface with the plasmonic nanoantenna arrays arranged in a hexagonal lattice structure provides the strongest enhancement whereas the degenerated hexagonal lattice structure has the lowest enhancement in these polarization states. This can be explained by the stronger SHG signals for the bare plasmonic metasurface compared to the other nanoantenna arrays with present inversion symmetry. Nevertheless, it can be concluded, that an allowed SHG in plasmonic nanoantenna array does not support an overall increase of SHG when it is combined with 1L-WS₂ for a hybrid metasurface. It is noticeable, that the hybrid metasurface with the plasmonic nanoantenna array arranged in a square lattice shows only half of the enhancement compared to the sample with the hexagonal lattice structure although both bare plasmonic metasurfaces exhibit only very weak SHG signals.

3.4. Tuning the plasmon resonances

To understand how plasmon resonances influence the SHG in hybrid metasurfaces, three additional metasurfaces are investigated, where the plasmon resonances are tuned away from the 1L-WS₂ resonance wavelength at 1230nm to shorter and longer wavelengths. For a better comparison between the results, we stick to a square lattice arrangement for every nanoantenna array. To shift the plasmon resonance away from the 1L-WS₂ band gap energy and therefore change the coupling to it, the dimensions of the individual nanorods are varied. For a longer resonance wavelength, the nanorods long axis is increased to 330nm resulting in a plasmon resonance at 1380nm. By shortening the nanorods' long axis by 30nm, a plasmon resonance at 1130nm is achieved. The plasmonic nanoantenna arrays with the different lengths of their individual nanorods are fabricated directly next to each other so that a single layer of 1L-WS₂ can be transferred on the nanoantenna arrays. In this way, any differences that might arise from transferring two or more 1L-WS₂ monolayers onto the different nanoantenna arrays are avoided. Further, the plasmonic nanoantenna arrays are fabricated in the same way as the previous samples, described in chapter 3.2.

Images of the linear characterization, as well as corresponding transmission spectra obtained by an FTIR-measurement, are shown in Figure 3.13. After the linear characterization of the plasmonic nanoantenna arrays, 1L-WS₂ is transferred again in the same way, as it was done for the previous samples. The subsequent PL-measurement, which results are shown in Figure 3.13C, confirms that the transferred 1L-WS₂ is indeed of the monolayer thickness, where a PL peak at 613 nm is observed.

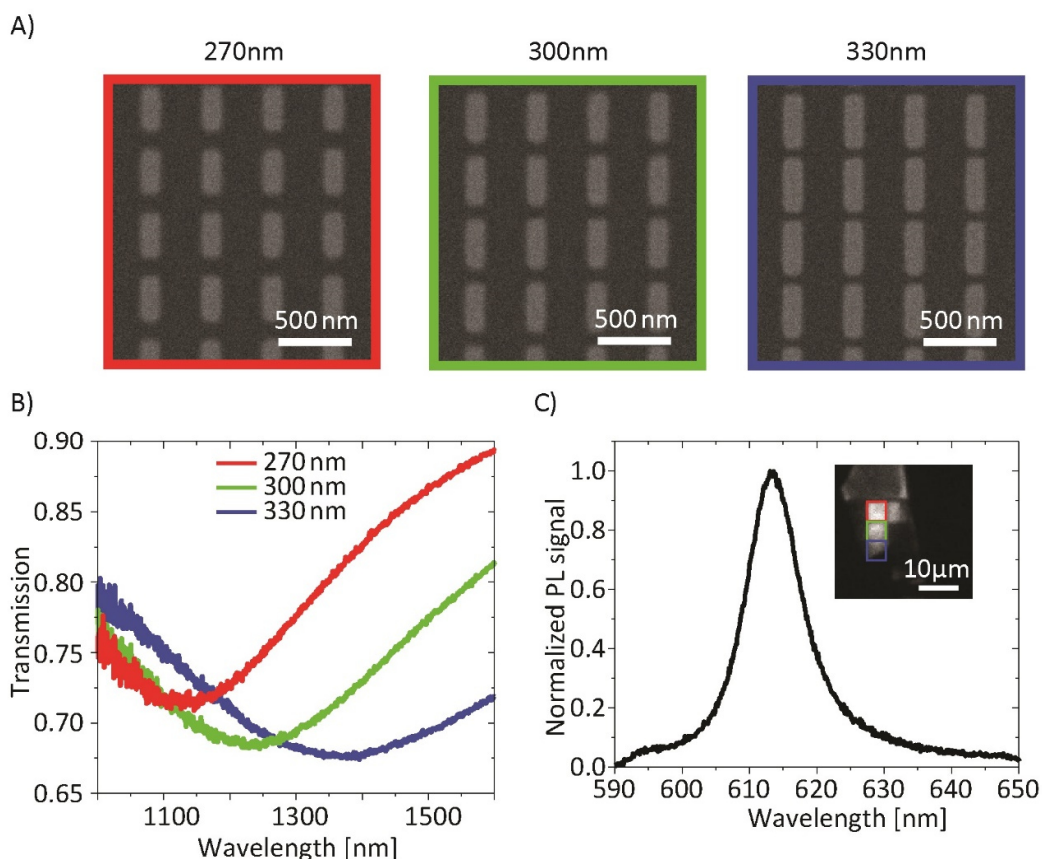


Figure 3.13: Linear characterization of the plasmonic nanorods. (A) SEM-images of the plasmonic nanoantenna arrays with nanorods of 270 nm, 300 nm and 330 nm length, respectively. **(B)** Transmission spectra of plasmonic nanoantenna arrays with nanorods of different lengths measured with unpolarized light. For shorter antenna length the plasmon resonance shifts to shorter wavelengths. Note that the colors in the spectra match the colors of the SEM-images shown in (A). **(C)** Measured PL spectrum of the hybrid metasurface sample with plasmonic nanorods of length 270 nm, 300 nm, and 330 nm. The inset shows a PL image of the hybrid metasurfaces, marked with the same colors as in (A). A similar image can be found in [80].

As the polarization-dependent measurements in the preceding chapter were all done at the same wavelength of 1230 nm, the excitation wavelength is now varied from 1160-1370 nm to examine, whether the enhancement changes for different excitation wavelengths and how it might be supported or further suppressed by shifted plasmon resonances. For these measurements, the linear polarization is switched to a circular polarization state, as it was shown, that the SHG generated in hybrid metasurface strongly depends on the linear polarization state. By doing so, a more generalized impact of the plasmon resonances on the SHG can be studied. Therefore, the input half-wave plate is exchanged with a quarter-wave plate and the output linear polarizer is removed. The used measurement setup is shown in Figure 3.14A and the results of the wavelength-dependent SHG measurements are shown in Figure 3.14C-D.

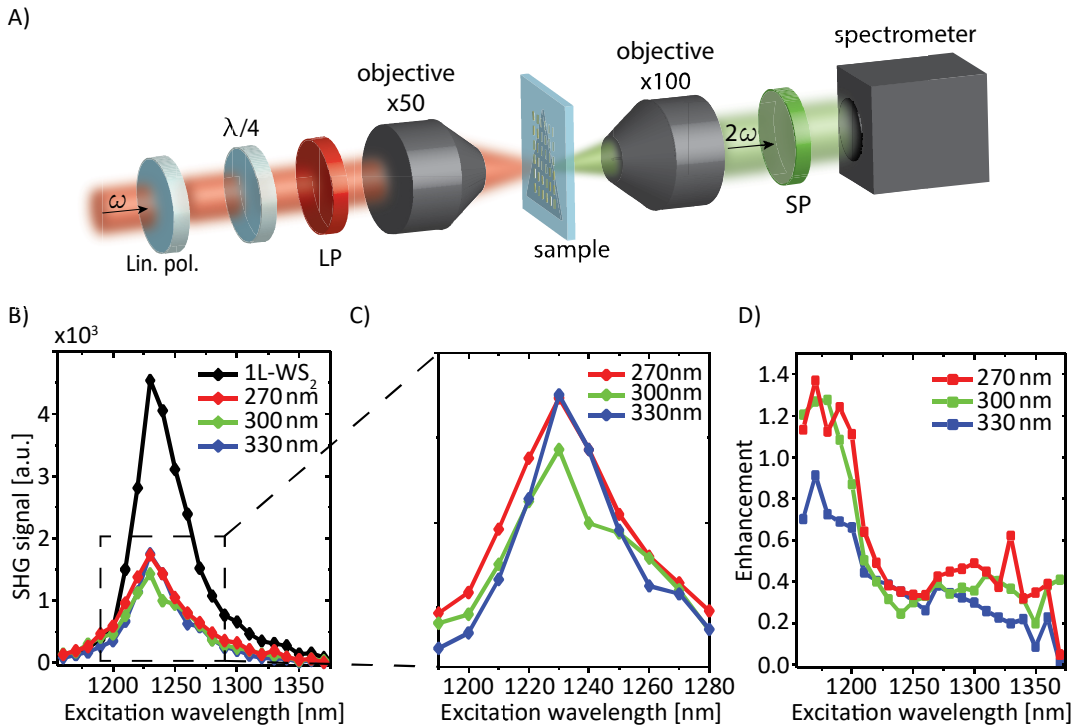


Figure 3.14: Tuning of the plasmon resonance. (A) Used setup for a wavelength-dependent SHG analysis with a circular input polarization. (B) SHG signals of bare 1L- WSe_2 and the different hybrid metasurfaces for various excitation wavelengths ranging from 1160-1370 nm. (C) Close-up of the SHG signals for the wavelengths of 1190-1280 nm shown in (A). (D) Calculated enhancement ϵ_{SHG} for different excitation wavelengths. Note that the SHG signal of bare plasmonic nanoantenna arrays is assumed to be zero for all excitation wavelengths since no SHG is expected. (D) Used setup for a wavelength-dependent SHG analysis. A similar image can be found in [80].

Since the plasmonic nanoantenna array does not contribute to the SHG in any way due to the lack of inversion symmetry, the SHG is mainly determined by the 1L-WS₂. As Figure 3.14A shows, the SHG signal decreases if the excitation wavelength is not located at 1230 nm, where the direct band gap of the TMD is excited directly. Further, it stands out, that the SHG measured for all hybrid metasurfaces is lower than the SHG measured of bare 1L-WS₂ for most of the wavelengths. This is consent with the previously made observations for the polarization-dependent SHG measurements in chapter 3.3 as well as the wavelength-dependent measurements, shown in Figure 3.5. Further, the SHG measured at 1230 nm, and therefore at the band gap of the 1L-WS₂, is lowest for the hybrid metasurface with plasmonic nanorods of 300 nm length. The other two hybrid metasurfaces provide an SHG signal of similar strength. This supports the previously made assumption, that if the plasmonic plasmon modes in the nanoantennas are excited more resonantly, they suppress the SHG signal generated in the 1L-WS₂. This statement is supported by the fact, that the plasmon resonances of the nanorods with a length of 270 nm and 330 nm are shifted by 100 nm to lower and 150 nm to higher wavelengths, respectively.

To estimate, whether the plasmon modes support an enhancement for the SHG in hybrid metasurfaces, the enhancement ϵ_{SHG} is calculated for this data set. As no SHG for bare plasmonic nanoantenna arrays is expected, it is now given by

$$\epsilon_{\text{SHG}} = \frac{SHG_{\text{hybrid}}}{SHG_{1L-WS_2}}. \quad (3.8)$$

The results are shown in Figure 3.14D. On closer inspection, it is noticeable, that for longer wavelengths no overall enhancement of the SHG for any of the hybrid metasurfaces is observable, although the plasmonic nanorods of 330 nm length are excited more resonantly. This changes for shorter wavelengths than 1230 nm. As for the hybrid metasurfaces with 330 nm long nanorods the SHG is still attenuated, while the other hybrid metasurfaces reach a small enhancement compared to bare 1L-WS₂, which reaches values of up to 1.4. Nevertheless, the overall measured enhanced SHG is still lower than the SHG measured at 1230 nm. This leads to the conclusion, that the SHG in hybrid metasurfaces can be enhanced, if they are excited at wavelengths with higher photon energies than half of the direct band gap energy. This enhancement is further supported if plasmon resonances are tuned to these wavelengths.

3.5. Impact of different symmetries

The previous investigations in this chapter have shown, that the individual symmetries of hybrid metasurfaces consisting of plasmonic nanoantenna arrays and 1L-WS₂ are of great importance. Therefore, an in-depth study regarding different symmetries is done in the following. The hexagonal lattice structure of the 1L-WS₂ and therefore its symmetry is not modifiable and certain symmetries in the lattice structure of plasmonic nanoantennas are already reported in chapter 3.3.5, now the symmetry of the individual nanoantennas are changed. Until now, simple nanorods with a two-fold rotational C₂ symmetry were fabricated, which cannot provide an SHG signal on themselves due to the present inversion symmetry. Though, in chapter 2.2.2 two additional plasmonic nanoantennas with a one-fold and three-fold rotational symmetry were introduced, labeled as C₁ and C₃.

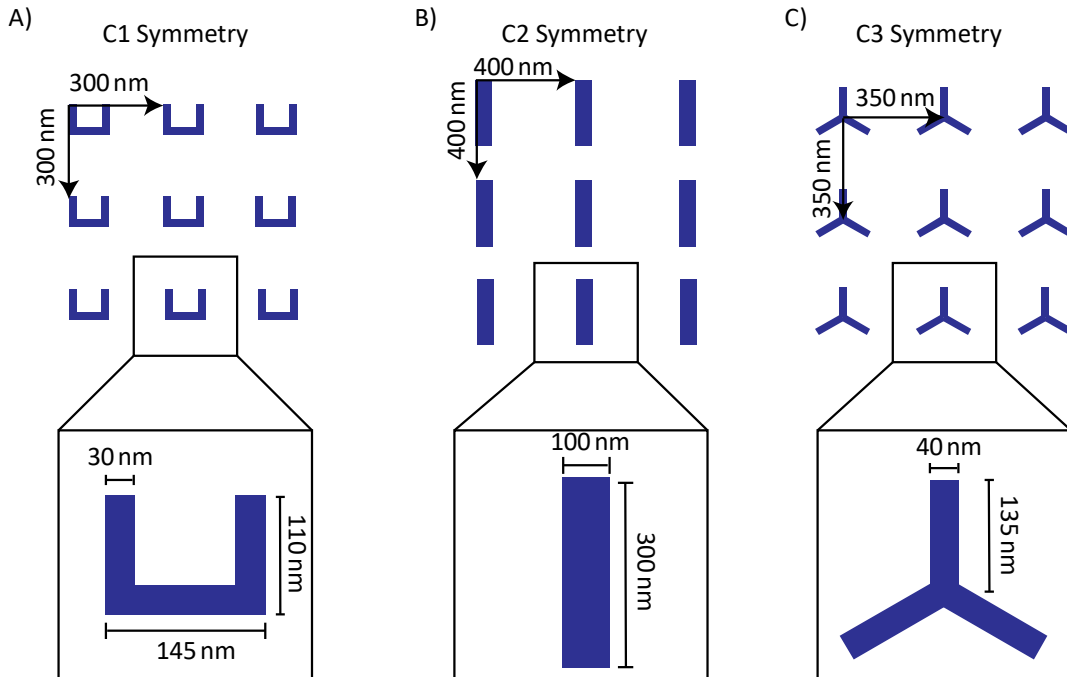


Figure 3.15: Different nanoantenna symmetries. Illustration of the fabricated plasmonic nanoantenna arrays arranged in a square lattice and the individual dimensions of the (A) C₁, (B) C₂ and (C) C₃ plasmonic nanoantenna. The arrows in each illustration indicate the lattice constant and are labeled with its value.

For these symmetries, the inversion symmetry is broken and plasmonic nanoantenna arrays consisting of antennas with either a C1 or C3 symmetry exhibit strong SHG signals without introducing a broken inversion symmetry with the help of the lattice structure, like it was done previously for plasmonic nanoantenna arrays consisting of C2 nanorods. For the upcoming investigation, six distinct plasmonic nanoantenna arrays are fabricated with nanoantennas of C1, C2 and C3 rotational symmetry, where each pattern is fabricated twice and only one will be covered with 1L-WS₂. In this way, the results of the hybrid metasurfaces can be compared to the results of bare plasmonic metasurface. The nanorods are designed to be resonant at 1230 nm again, where the previous studies from chapters 3.3.3 and 3.4 have shown, that for this wavelength, the strongest SHG signals can be measured. For this study, plasmonic nanoantenna arrays consisting of nanorods with individual C1, C2 and C3 rotational symmetry are fabricated directly next to each other, so that a single layer of 1L-WS₂ can be transferred on the nanoantenna arrays. In this way, any differences that might arise from transferring two or more 1L-WS₂ monolayers onto the different nanoantenna arrays are avoided. A schematic illustration of the three distinct plasmonic nanoantenna arrays including their dimensions is shown in Figure 3.15. Note, that the plasmonic nanoantenna arrays are fabricated in the same way again as the previous samples, described in chapter 3.2.

After the fabrication of the plasmonic nanoantenna arrays, SEM-images are taken and the transmission spectra are measured again. Subsequently, a monolayer 1L-WS₂ is transferred to the nanostructures. After the transfer, a PL-measurement of the transferred WS₂ layer is done to confirm the monolayer thickness. The results of these linear optical characterizations are shown in Figure 3.16. The measured transmission spectra show, that not for every plasmonic nanoantenna array a plasmonic resonance at 1230 nm is measured. Only for the nanoantennas with a C1 rotational symmetry, a suitable resonance wavelength is observed. For the plasmonic nanorods (C2), the plasmon resonance shifts to 1220 nm, whereas for the C3 nanoantennas the resonance is located at 1270 nm. As the plasmon resonance is very sensitive to the shape and dimensions of the nanoantennas, small wavelength shifts are unpreventable and were already observed previously, when different lattice structures were investigated (Figure 3.3D). Although these plasmonic nanoantenna arrays show slightly stronger shifts, they are still in an acceptable range for nonlinear measurements, because previously obtained results, discussed in chapter 3.4, have shown, that even greater shifts to longer wavelengths have only a limited impact on the SHG. The measured PL-spectrum, illustrated in Figure 3.16C, confirms, that the transferred WS₂ is indeed of monolayer thickness. The spectrum shows a clear peak at 613 nm, which is comparable in position and width to the previously measured PL-spectra, shown in Figure 3.4D and Figure 3.13C.

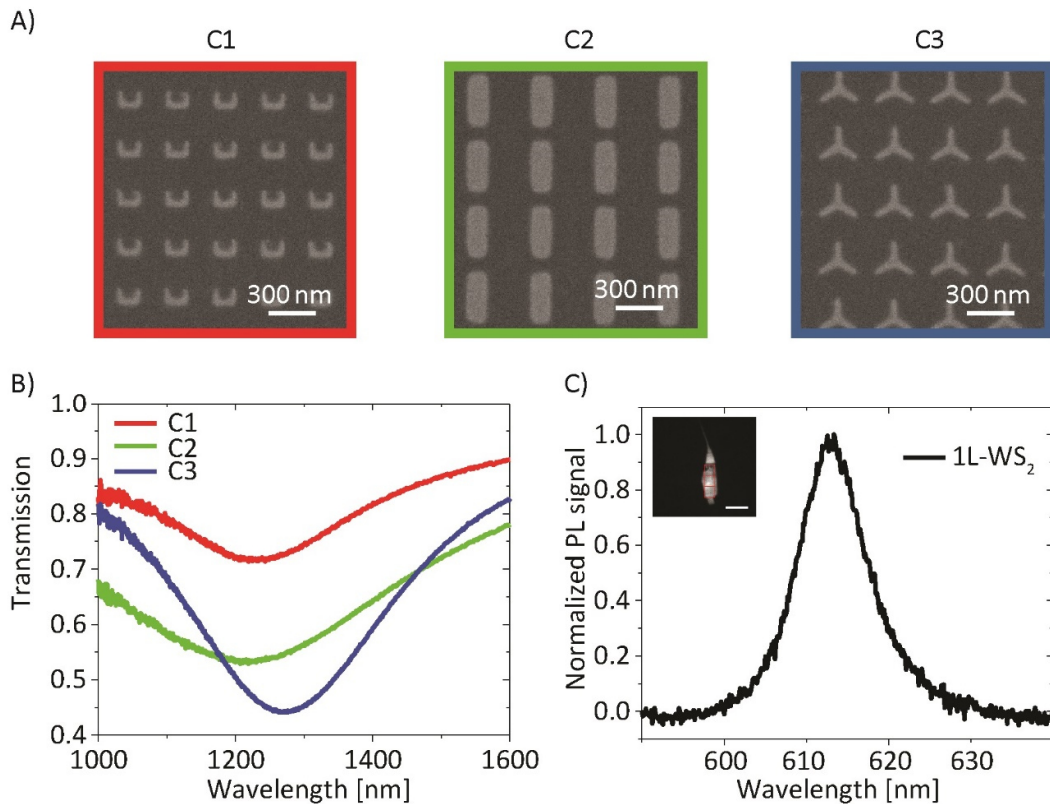


Figure 3.16: Linear characterization (A) SEM-images of the plasmonic nanoantenna arrays with nanoantennas of different rotational symmetries. **(B)** Corresponding transmission spectra for each nanoantenna array. Note that the color-coding matches the marking colors in (A). **(C)** Photoluminescence measurement of the transferred WS₂ layer. The spectrum shows a peak at 613nm, confirming a monolayer thickness. The inset shows a PL image of the measured monolayer, where the hybrid metasurfaces are marked in red.

After the linear characterization, the SHG of each bare plasmonic nanoantenna array as well as of each hybrid metasurface is measured. Therefore, the same setup, which is schematically illustrated in Figure 3.14A, under circular illumination polarization is used. The experimentally obtained results are shown in Figure 3.17.

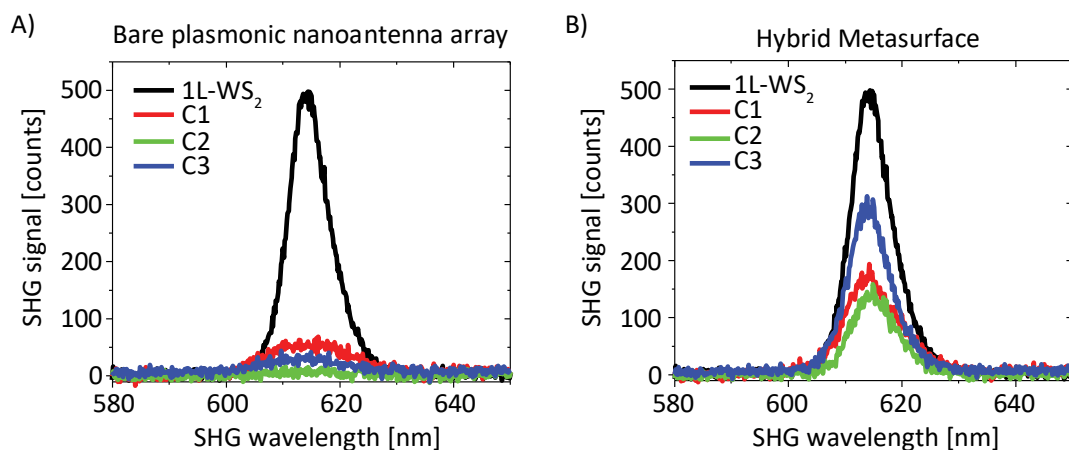


Figure 3.17: SHG signals for different nanoantenna symmetries. (A) SHG signals for bare plasmonic nanoantenna array for the different rotational symmetries of the individual nanoantennas. **(B)** SHG signals of hybrid metasurfaces for the different nanoantennas' rotational symmetry. Note that in (A) and (B) the SHG signal of bare 1L-WS₂ is added as a reference.

By looking at the results, it stands out, that the solely 1L-WS₂ provides the strongest SHG signals among all measured samples. This observation is common to all hybrid metasurfaces, investigated previously in this chapter. A second important observation is, that the SHG signal increases for every hybrid metasurface compared to its bare plasmonic counterpart without a transferred WS₂ monolayer on top. Although the plasmonic nanoantenna arrays with C1 or C3 nanoantennas show an SHG signal by themselves, the SHG gets boosted when the nanorods are covered with a monolayer WS₂. By comparing the SHG signals of the three different hybrid metasurfaces, it becomes strongest for the metasurface containing the nanorods with a three-fold rotational C3 symmetry, followed by the hybrid metasurface consisting of C1 nanoantennas. Therefore, it can be concluded, that the SHG generated in hybrid metasurfaces can be maximized by the choice of symmetry for the individual nanorods. Nevertheless, no overall enhanced SHG, which is stronger than the SHG arising from solely 1L-WS₂ can be observed, regardless of the symmetry of the individual plasmonic nanoantennas.

3.6. Conclusion

In this chapter, a rigorous study of the SHG generated in plasmon/TMD hybrid metasurfaces was performed, to investigate, whether a further enhancement compared to solely 1L-WS₂ or bare plasmonic nanoantenna array can be achieved due to the utilization of the strong near-fields in plasmonic nanostructures. As part of this study, the impact on various parameters, e.g. polarization, lattice structure and symmetry, was investigated and underlined by experimental results. As the SHG generated in solely 1L-WS₂ peaks at an excitation wavelength of 1230 nm, the plasmonic nanoantenna arrays were designed to be resonant at this wavelength. Although the linear characterization of the individual parts of the hybrid metasurfaces showed good matching between the plasmon resonance and half of the 1L-WS₂ band gap at 1230 nm, no overall enhanced SHG was observed for any of them. Nevertheless, the variation of plasmon modes has shown, that an overall enhanced SHG can be achieved for excitation wavelengths lower than 1230 nm if the plasmon modes are tuned to these wavelengths (compare Figure 3.14). Further, the selection of the plasmonic nanorods' individual symmetry plays a key role, when it comes to the SHG in hybrid metasurfaces. The experimental results have shown (Figure 3.17), that the hybrid metasurfaces containing plasmonic nanoantennas with an individual three-fold rotational C₃ symmetry provide a stronger SHG signal than their counterparts with a C₁ or C₂ rotational symmetry. As these results already provide new approaches to generate an enhanced SHG in hybrid metasurfaces, the polarization-dependent measurements have shown, that the plasmonic nanoantenna arrays provide a channel for the SHG into polarization states, that are usually forbidden by either plasmonic nanoantenna array or solely 1L-WS₂ (Figure 3.9). An enhancement of SHG of about a factor of up to 40 in these polarization states has been observed (Figure 3.12). Further, a simple model was developed, which describes how the plasmonic nanoantennas attenuate the process of SHG in hybrid metasurfaces by a shadowing effect (chapter 3.3.6). As this simple model recreates the experimental data very well, these insights into the coupling of plasmon modes and 1L-WS₂ pave the way for promising applications of hybrid metasurfaces, where the implementation of phase information, e.g. the Pancharatnam-Berry phase of plasmonic nanoantennas, can be accomplished.

4. PHASE MODULATION IN HYBRID METASURFACES

Plasmonic metasurfaces, like the previously presented ones, are capable of manipulating light in different ways. Many applications rely on the spatial tailoring of the amplitude and phase to imitate conventional optical elements (e.g. lenses) or complex information encoding, like holograms [51, 97-101]. In much used optical components, e.g. lenses and wave plates, modulations of incident light are done in their volume over distances, which are much larger than the wavelength. Unlike such conventional optics, where a change in the light is accumulated during its optical path in the medium, plasmonic metasurfaces can induce an abrupt change. A basic implementation of such an abrupt change is the phase modulation via the geometric Pancharatnam-Berry (PB-) phase, which can be used for tailoring the linear and nonlinear response of hybrid metasurfaces.

In the following, the concept of the geometric PB-phase is introduced and its application in hybrid metasurfaces is studied. In particular, it is shown, that plasmonic metasurfaces can be fabricated on top of 1L-WS₂, which is fabricated by CVD and transferred onto a quartz substrate in the first place. Subsequent SHG measurements show, that the plasmonic metasurface can alter the SHG generated in 1L-WS₂ under circularly polarized illumination into the emission of SHG-light in a circular polarization state, which is usually forbidden by solely 1L-WS₂ (see Figure 2.14B). Afterward, the implementation of phase modulation by making use of PB-phase in plasmonic nanoantenna arrays is shown, which opens up possibilities for far-field interference pattern and holography encoded in the SHG signal generated in plasmonic/TMD hybrid metasurfaces. Note, that parts of this chapter are already published in [102].

4.1. The Pancharatnam-Berry phase

Usually, a phase difference between light beams arises due to their different optical path lengths in a medium. In contrast to this, the geometrical Pancharatnam-Berry phase results from a space-variant change of the polarization, which was first reported by S. Pancharatnam [103]. As the presented plasmonic nanoantennas can be seen as an optical element that acts as a half wave-plate [96], the change in the polarization is accompanied by a phase shift compared to the incident light wave. As it was already utilized in chapter 3.3.6, the Jones matrix of a plasmonic nanoantenna, which is an anisotropic scatterer rotated by an angle α , can be written as [5]

$$J(\alpha) = \begin{bmatrix} \cos \alpha & -\sin \alpha \\ \sin \alpha & \cos \alpha \end{bmatrix} \begin{bmatrix} t_1 & 0 \\ 0 & t_2 \end{bmatrix} \begin{bmatrix} \cos \alpha & \sin \alpha \\ -\sin \alpha & \cos \alpha \end{bmatrix}. \quad (4.1)$$

Here, t_1 and t_2 represent the complex scattering coefficients for an incident light, which is linearly polarized along the two axes of such an anisotropic scatterer. By considering a circular polarized incident E-field, given by

$$\vec{E}_{L/R} = \frac{1}{\sqrt{2}} \begin{pmatrix} 1 \\ i\sigma \end{pmatrix}, \quad (4.2)$$

where $\sigma = \pm 1$ denotes the left or right circular polarization state, respectively, the scattered light is calculated by

$$\begin{aligned} \vec{E}_S &= J(\alpha) \cdot \vec{E}_{L/R} = (t_1 - t_2) \begin{pmatrix} 1 \\ \sigma i \end{pmatrix} + (t_1 + t_2) e^{i2\alpha\sigma} \begin{pmatrix} 1 \\ -\sigma i \end{pmatrix} \\ &= (t_1 + t_2) \vec{E}_{L/R} + (t_1 - t_2) \vec{E}_{R/L} e^{i2\alpha\sigma}. \end{aligned} \quad (4.3)$$

It stands out, that the first term in equation (4.3) describes scattered light, which has the same handedness as the incident light and does not contain any geometrical phase. This is different for the second term, which describes a scattered light wave of the opposite handedness, phase-shifted by a factor of $\phi = 2\alpha\sigma$. This acquired phase, called Pancharatnam-Berry phase, is dependent on the relative orientation of the nanoantenna and can cover up phase shifts in the entire range of $0 - 2\pi$ for rotation angles of $0 - 180^\circ$. As a plasmonic metasurface consists of many individual nanoantennas, this phase shift can be different for each individual nanoantenna within

the metasurface, since they all can be individually rotated by a different angle α_i . This circumstance can be exploited to encode complex information, e.g. holographic images, into metasurfaces by converting the information pixel-wise into rotation angles of individual nanoantennas.

As equation (4.3) shows, the E-field transmitted by the plasmonic nanoantenna arrays provides two circular polarized beams of opposite helicity, where the cross-polarized beam contains phase information and the co-polarized beam is unmodulated. In a simplified picture, where the SHG in hybrid metasurfaces is considered, these two beams can generate a second-harmonic signal independently from each other. Therefore, the process of SHG in hybrid metasurfaces can be split into two parts, the linear optical scattering at the plasmonic metasurface and the subsequent SHG of the scattered light at the 1L-WS₂. This process is illustrated in Figure 4.1.

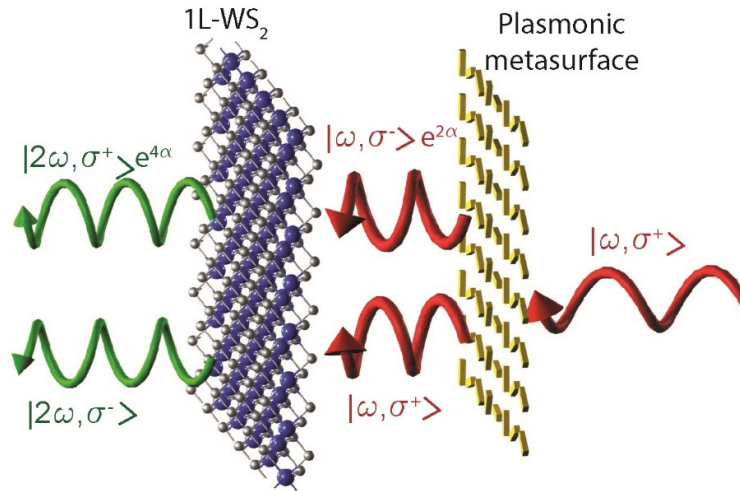


Figure 4.1: Schematic illustration of the hybrid metasurface for nonlinear frequency conversion. The hybrid metasurface consists of plasmonic Au-nanorods that are placed directly on top of monolayer WS₂. An incident laser beam with a frequency ω and right circular polarization σ^+ (RCP) interacts with the metasurface. The scattered field by the nanorods can be decomposed into the superposition of both circular polarization states σ^+ (RCP) and σ^- (LCP), which couple to the WS₂ and result in a second harmonic generation (SHG). Note that only the σ^- state of the scattered fundamental light by the nanorods carries an additional phase of 2α due to the orientation of the nanorods. After the interaction with the WS₂ the phase of the σ^+ SHG signal doubles to 4α . A similar image can be found in [102].

The first part of the process is already described by equation (4.3), where the decomposition of the E-field transmitted by the plasmonic metasurface into two beams is considered. The subsequent process of SHG at the 1L-WS₂ can be calculated analog to the SHG calculation in chapter 3.3.6 via equation (3.5), where the E-fields

$$\vec{E}_{S,1} = (t_1 + t_2)\vec{E}_{L/R} \quad (4.4)$$

and

$$\vec{E}_{S,2} = (t_1 - t_2)\vec{E}_{R/L}e^{i2\alpha\sigma} \quad (4.5)$$

are inserted. The corresponding second-order polarization terms are then given by

$$\vec{P}_1^{(2)} = \varepsilon_0\chi^{(2)}\vec{E}_{S,1}^2 = -2\varepsilon_0\chi^{(2)}(t_1 + t_2)^2 e^{i\frac{\pi}{2}} \cdot \vec{E}_{R/L} = C \cdot \vec{E}_{R/L} \quad (4.6)$$

and

$$\vec{P}_2^{(2)} = \varepsilon_0\chi^{(2)}\vec{E}_{S,2}^2 = 2\varepsilon_0\chi^{(2)}(t_1 - t_2)^2 e^{i\frac{\pi}{2}} \cdot \vec{E}_{L/R}e^{i4\alpha} = D \cdot \vec{E}_{L/R}e^{i4\alpha} . \quad (4.7)$$

Equations (4.6) and (4.7) show, that the hybrid metasurface generates two circular polarized SHG beams in opposite polarization states, where the cross-polarized SHG signal (σ^-) has no phase modulation and the co-polarized SHG signal (σ^+) is phase modulated based on the nanoantennas' rotation angle α (see Figure 4.1). Note, that the labels co- and cross-polarization state are given with respect to the polarization state of the fundamental illumination light, given by equation (4.2). However, equation (4.7) also shows, that the encoded phase information is dependent on the rotation angle of the individual nanoantennas and equals $\phi = 4\alpha$, which is twice as large as the phase modulation in the linear scattered light, calculated in equation (4.3). Note, that any cross term $\vec{P}_{cross} \propto \chi^{(2)}\vec{E}_{S,1}\vec{E}_{S,2}$ vanishes, if a superposition of the two E-fields is inserted into equation (3.5).

4.2. Fabrication process

In 2.3.1, the fabrication process of a hybrid metasurface, where plasmonic nanoantenna arrays are covered with a monolayer of WS_2 was described. For the upcoming investigations, 1L- WS_2 fabricated by ME is no longer used, because of their limited size. For the upcoming investigations, large monolayer flakes are required, especially for the implementation of holographic images via the plasmonic nanoantenna array. Since smaller plasmonic metasurfaces contain fewer nanoantennas, this reduced number of 'pixels' results in a downgraded image quality of the encoded holographic image. Therefore, larger plasmonic metasurfaces are fabricated and larger 1L- WS_2 monolayers are needed. 1L- WS_2 fabricated by CVD (see chapter 2.3.1) is transferred onto a quartz substrate. These CVD-grown monolayers were fabricated commercially and purchased at 2Dsemiconductors. The substrates are covered with 1L- WS_2 flakes, which show a strong PL-signal at around 2 eV, as illustrated in Figure 2.12C-D. The fabrication of the plasmonic metasurface is done on the same substrate onto the 1L- WS_2 flakes. Due to the high coverage density of the 1L- WS_2 flakes on the sample surface, a great percentage of the plasmonic metasurface is placed directly onto monolayers of WS_2 . Although this chapter handles different kinds of hybrid metasurfaces for various applications, the fabrication routing of the plasmonic nanoantenna arrays stays the same as described in chapter 3.2. First, different parameters, which have a great impact on the SHG in hybrid metasurfaces, are investigated for a nanoantenna array consisting of gold nanorods with a two-fold rotational C_2 symmetry arranged in a square lattice with a period of 400 nm. The nanoantennas are designed to be resonant at half of the band gap energy of 2 eV at 1230 nm again. To approach the best overlap between the resonance wavelength with half of the band gap energy of 1 eV, a set of three metasurfaces is fabricated, where the lengths of the nanorods vary from 220-230 nm. Additionally, the metasurfaces are designed with spatial varying orientation angles of the individual nanorods, where horizontally neighboring antennas are rotated by an angle of $\alpha = \Delta 70^\circ$. A schematically illustration of the plasmonic metasurface labeled with their dimensions can be found in Figure 4.2A. These spatial varying orientations are implemented to visualize the impact of the geometric PB-phase. Neighboring antennas with different rotation angles implement different phase modulations to the generated SHG signal leading to an interference pattern in the far-field. The chosen rotation angles result in a phase difference of $\Delta\phi = 80^\circ$ for neighboring antennas leading to a spatially modulated SHG in the horizontal direction due to interference. Note, that eight consecutive nanoantennas are rotated by 70° in the horizontal direction incrementally, forming a unit cell of 8×1 nanoantennas. This periodicity is marked in the inset of Figure 4.2B. Hence, a horizontal periodicity is formed with a period of $3.2 \mu\text{m}$, which covers up a

phase modulation of almost 4π over one period. It is expected, that this implemented phase modulation leads to a stripe pattern for the SHG generated in the co-polarization state. Note, that in the vertical direction no additional periodicity exists and this stripe pattern should only be visible in the horizontal direction.

4.3. Linear optical characterization

After the fabrication process, the hybrid metasurfaces are characterized in the linear regime, where their transmission spectra, as well as PL-spectra and images, are measured. First, the transmission spectra of the hybrid metasurfaces are measured. Since the 1L-WS₂ only interacts weakly with the NIR-light due to a low absorption rate at these wavelengths, the transmission spectra are mainly determined by the plasmonic metasurface so that the plasmon resonance can be estimated.

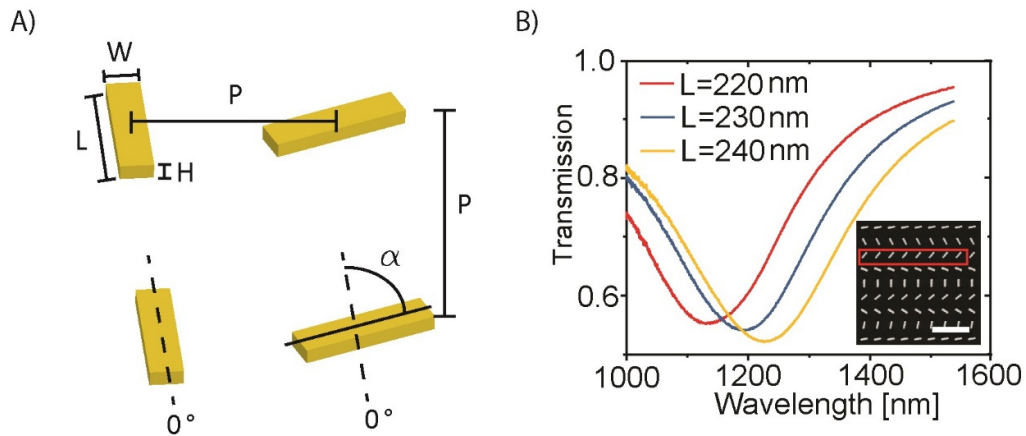


Figure 4.2: Characterization of hybrid metasurfaces (A) Schematically illustration of the dimensions of the plasmonic metasurface. The width of the nanorods is $W=50$ nm, the height is chosen to $H=30$ nm and the length varies from $L=220$ - 240 nm. The period of the square lattice is $P=400$ nm and the relative orientation angle of next neighbored antennas is $\alpha = \pm 70^\circ$. **(B)** Measured transmission spectra of hybrid metasurfaces with three different antenna lengths and unpolarized light. The resonance wavelengths of the nanoantennas can be tuned to match the resonance wavelength of the two-photon absorption process of 1L-WS₂ at 1230 nm by optimizing the antenna length. The inset shows a scanning electron microscopy (SEM) image of the Au-metasurface with antenna lengths of 220 nm (scale bar equals 1 μ m). The red marked area indicates a unit cell, where within each nanorod is rotated by 70° incrementally. A similar image can be found in [102].

The corresponding results are shown in Figure 4.2B, as well as an SEM image of a plasmonic metasurface. The results of the transmission spectra measurement show, that for a nanorod length of 240 nm, the plasmon resonance is located at around 1230 nm, which is in good accordance with half of the band gap energy of 1 eV. Nevertheless, the other plasmonic metasurfaces with shorter nanorods are also suitable for nonlinear measurements, as their plasmon resonance is only slightly blue-shifted so that they still might show coupling effects with the 1L-WS₂. After the transmission measurement, the PL-spectra of the fabricated hybrid metasurfaces are measured. Therefore, the previously PL measurement setup, illustrated in Figure 2.12A, is used. The results are shown in Figure 4.3.

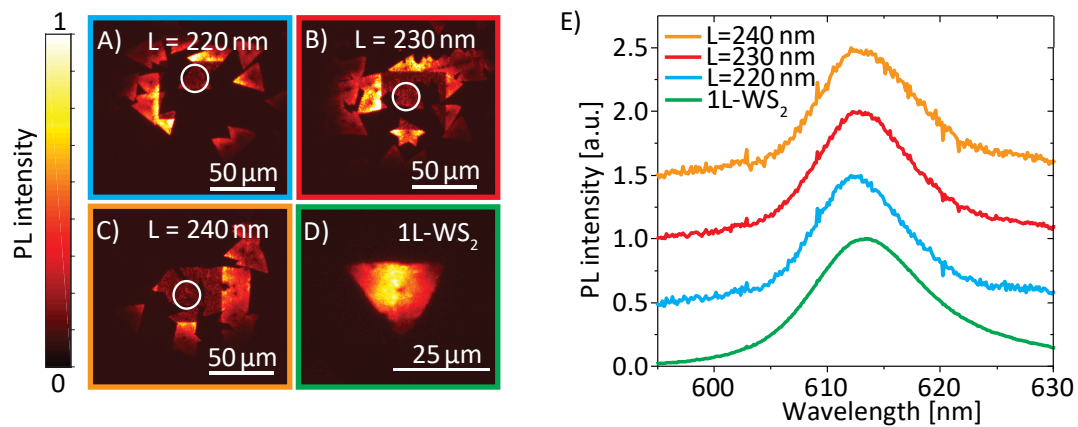


Figure 4.3: Photoluminescence measurements for excitation at 532 nm wavelength. (A-C) PL-images of the areas around three different hybrid metasurfaces with different antenna lengths $L=220\text{--}240\text{ nm}$. The white circles indicate the area, where the corresponding PL spectra are taken. The WS₂ flakes are clearly visible. The higher PL intensities close to the center of the image result from the excitation with an enlarged Gaussian beam shape (diameter $\sim 50\ \mu\text{m}$) at 532 nm. Note, that the squared shadows in the PL images indicate the metasurfaces. (D) PL image of a single 1L-WS₂ flake without plasmonic nanorod antennas on top for comparison. (E) Corresponding PL spectra showing a clear peak at 614 nm. The spectra are shifted upwards by 0.5 for better visibility. A similar image can be found in [102].

The PL-images in Figure 4.3A-D show, that the PL-light coming from the sample shows higher intensities around the hybrid metasurfaces from bare 1L-WS₂ compared to the intensities coming from the hybrid metasurfaces themselves. This is due to a partial reflection of the incident laser light at 532nm by the plasmonic nanorods, which results in less transmitted light hitting the 1L-WS₂ for the generation of PL-light. This is supported by experimentally obtained transmission spectra in the visible range, illustrated in Figure 4.4A. The experimental data shows a small dip at wavelengths around 550nm, which explains a slightly stronger scattering of the excitation laser light and the attenuated PL-intensity. This dip arises most likely due to the transversal plasmon mode in the short axis of the nanorods. Another explanation might be quenching effects, which were also observed in other works, where plasmonic nanostructure arrays attenuated the PL-intensity [104]. Nevertheless, the strong PL-emission allows a clear identification of the spatial location of the 1L-WS₂ flakes within the metasurfaces. Anyway, the nanorods are designed to be resonant at wavelengths around 1230nm and therefore, only a weak coupling effect for the SHG emission at 615nm is expected, which is supported by the experimental and theoretically obtained transmission spectra in Figure 4.4B, where the data show a nearly flat response at this wavelength and no significant resonance is visible at 615nm. Therefore, no destructive or constructive interference due to the encoded phase information is visible in the PL-images. The corresponding spectrum of this strong PL-emission is shown in Figure 4.3E. The obtained PL-spectra show a clear peak at 614nm, confirming that the excited 1L-WS₂ flakes within the hybrid metasurface are indeed of monolayer thickness. Further the PL-spectra of all hybrid metasurfaces show good accordance to previously measured PL-spectra. Only the PL-peak of the hybrid metasurface with plasmonic nanorods of L=220nm is slightly blue-shifted by around 1nm, which is most likely caused by experimental uncertainties. Nevertheless, the results of the PL-measurements prove, that the band gap of the 1L-WS₂ flakes is not changed significantly by the fabrication process of the plasmonic nanoantenna arrays.

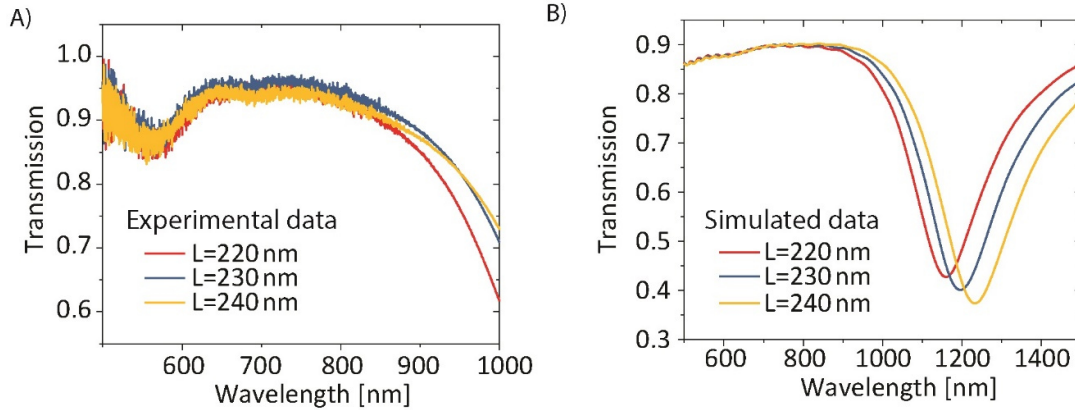


Figure 4.4: Linear transmission spectra for the hybrid metasurfaces. (A) Experimentally gained linear transmission spectra of the hybrid metasurfaces with the nanorod length of 220-240 nm in the visible range. The resonance dip occurring in the near-infrared region, starting at around 900 nm, shows the onset of the plasmonic resonance at around 1200 nm. The measurement was taken with unpolarized light. **(B)** Simulated transmission of the periodic nanorod array predicting a strong plasmonic resonance around 1200 nm. The simulations are confirmed by the experimental results shown in Figure 4.2B. Note, that the simulation was done with CST microwave studio without a monolayer WS₂. A similar image can be found in [102].

4.4. Nonlinear optical imaging

To characterize the SHG of the fabricated hybrid metasurfaces, a similar setup to the previously presented one in chapter 3 is used. A schematic illustration can be found in Figure 4.5. As a fundamental pump light, ultrashort laser pulses with a pulse duration of around 60 fs at a repetition rate of 1 MHz generated by an optical parametric amplifier (OPA) in the NIR-wavelength range from 1210-1270 nm are used. As for the upcoming measurements, a circular polarization state is required. Therefore, the fundamental beam is circularly polarized by a linear polarizer and a quarter wave-plate. Afterward, it is focused by a lens onto the sample with a spot size of around 50 μm (FWHM), so that the hybrid metasurfaces, as well as surrounding 1L-WS₂ flakes, are illuminated. The emitted SHG is collected by a microscope objective and filtered by a short pass. The subsequent polarization optics, consisting of another quarter wave-plate and a linear polarizer, is used to choose between the co- or cross-polarized SHG signal, which is measured by either an sCMOS camera or a spectrometer.

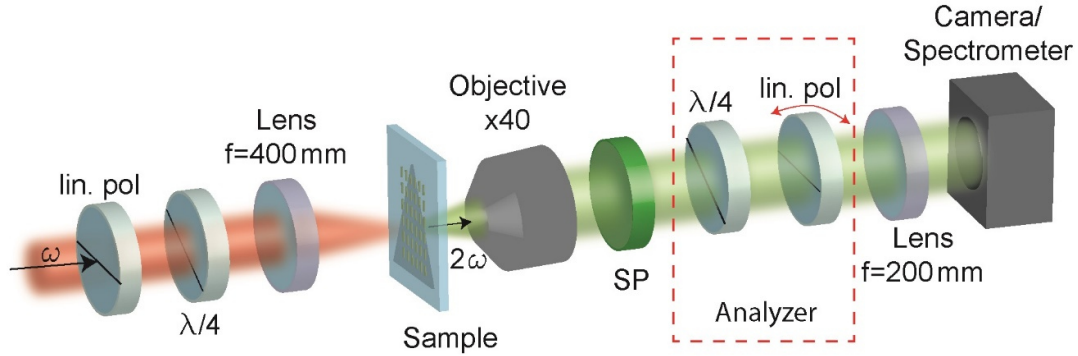


Figure 4.5: Setup for nonlinear optical measurements of the hybrid metasurfaces. The fundamental laser beam is focused on the metasurface field on the substrate and the polarization state is set by the linear polarizer and a quarter-wave plate. The spatially resolved SHG signal is collected by a microscope objective (x40), filtered by a short pass as well as polarization optics (analyzer) and measured by a spectrometer or camera. A similar image can be found in [102].

4.4.1. Visualization of optical selection rules for SHG

First, the two polarization states of the SHG, predicted by the equations (4.6) and (4.7) are investigated. Therefore, the three distinct hybrid metasurfaces are illuminated with a right-circular polarized laser beam at a wavelength of 1230 nm. The results of the spatially resolved SHG are shown in Figure 4.6. The SHG signals, measured in the cross-polarization state σ^- (see Figure 4.6A-D top row), becomes strongest for the 1L-WS₂ flakes without plasmonic nanoantennas on top, which are located nearby the hybrid metasurfaces. Based on the selection rules of SHG in monolayer WS₂, as depicted in Figure 2.14, this SHG light is only generated in this cross-polarization state at the K and K' point of the 1L-WS₂. Hence, the co-polarization state lacks an SHG signal generated for the 1L-WS₂, which can be seen by the SHG images shown in Figure 4.6A-D bottom row.

Compared to the SHG signals observed in the cross-polarization state, the intensity of the SHG signals in the co-polarization state is comparatively low, which is a result of the coupling process between the plasmonic nanoantennas to the fundamental light. The interaction of the fundamental light with the plasmonic metasurface can be divided into four parts, the scattering into the co- and cross-polarization state, the reflection and absorption. While the reflection and absorption do not contribute to any measured SHG

signal, the SHG signal measured in the co-polarization state can only be generated by the scattered fundamental light in the cross-polarization state. While the SHG signal, measured in the cross-polarization state is based solely on the SHG process in the 1L-WS₂, the SHG signal measured in the co-polarization state requires the additional polarization conversion of the plasmonic metasurface. Note, that the labels co- and cross-polarization state are still given with respect to the polarization state of the fundamental illumination light, given by equation (4.2). This observation of different SHG signal strengths in the two polarization states hints towards a limited polarization conversion efficiency of the plasmonic nanostructures, which has already been addressed in previous works [13].

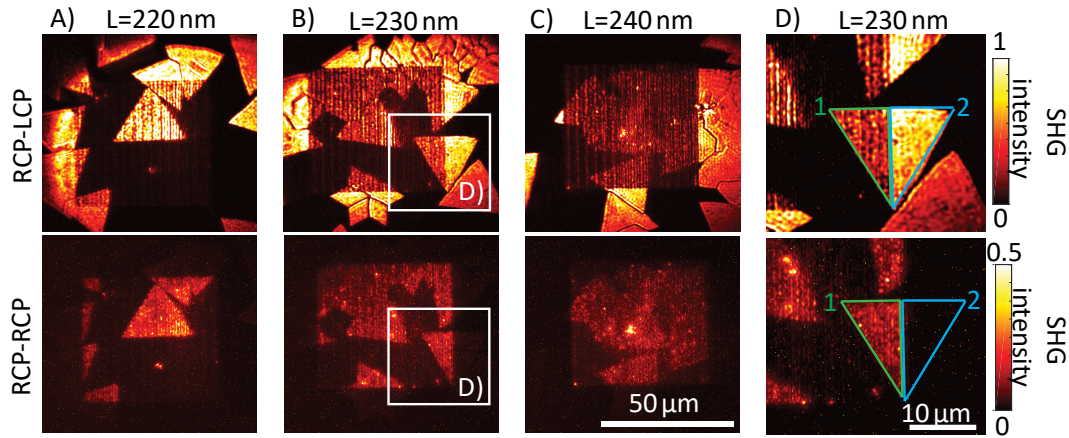


Figure 4.6: Circular polarization states of SHG (A-C) SHG images of three different metasurfaces with antenna lengths of $L=220-240$ nm measured for the cross-polarization state σ^- (LCP) (top row) and in co-polarization state σ^+ (RCP) (bottom row). The SHG signal of the surrounding 1L-WS₂ nearly vanishes in the co-polarization state σ^+ due to the selection rules for the SHG process. **(D)** Close-up of the marked area (white box) in (B) showing the edge of the metasurface passing through a 1L-WS₂ flake. Area 1 (marked in green) points out an area covered with Au-nanoantennas while area 2 (marked in blue) points out the same flake which is not covered with Au-nanoantennas. The SHG signal in the blue marked area 2 vanishes for measurement in the co-polarization state. A similar image can be found in [102].

However, the coupling of the plasmonic metasurface to the 1L-WS₂ is clearly visible for a flake, which is only partially covered with plasmonic nanoantennas. The area, marked by a white box in Figure 4.6B, contains a 1L-WS₂ flake, which can be divided into two parts, a part with and another part without nanoantennas on top. An enlarged image is

shown in Figure 4.6D for better visualization. As the images show, the edge of the hybrid metasurface can be clearly identified and divides the flake by approximately the half. In the magnified view, the two areas are marked with 1 and 2 (green and blue) and show the SHG for all four possible polarization states. For the bare 1L-WS₂ flake without plasmonic nanoantennas on top (blue marked area 2), a strong SHG signal only for the cross-polarization state σ^- is visible, which is in accordance with the optical selection rules for SHG in 1L-WS₂. In contrast to this, an SHG signal for the hybrid metasurface case (green marked area 1) for both polarization states is observable, where the nanoantennas scatter fundamental light in both polarization states, which subsequently is frequency-converted by 1L-WS₂.

In contrast to the strong SHG signals arising for the hybrid metasurfaces in both polarization states, the bare plasmonic metasurface does not show a significant SHG signal, whether for the co- nor the cross-polarization state. The lack of the SHG signal can be explained by their present inversion symmetry, which does not allow the generation of second harmonics [51]. Although the SHG intensity is nearly zero, at some locations a small SHG signal comparable to the background signal of the quartz substrate is detectable, which is most likely due to surface defects and deviations from the perfect inversion symmetry arising from a non-perfect fabrication process.

By comparing the different hybrid metasurfaces with each other, the impact of the nanorods' length and therefore the impact of the plasmon resonance can be studied. The SHG signals, arising from the three different hybrid metasurfaces with antenna lengths of L=220-240 nm, all show a similar strength among each polarization state. Only the metasurface with nanorods of 220 nm length provides a slightly stronger signal strength in each polarization state. This is in good accordance with previously measured SHG signals, where the SHG signals of different hybrid metasurfaces were investigated (see Figure 3.14B-D). These results also showed that the SHG strength increases by a small amount if the plasmon resonance is tuned to shorter wavelengths. However, the different lengths of the plasmonic nanorods have only a weak impact on the SHG signal of the hybrid metasurface.

4.4.2. Wavelength dependency

As previous measurements have shown (see Figure 3.14B-D), the SHG efficiency in 1L-WS₂ as well as in hybrid metasurfaces is strongly dependent on the excitation wavelength. For wavelengths around half of the band gap energy of 1L-WS₂ at 1 eV, the process of SHG is strongly enhanced [50], which can be even further enhanced if plasmon resonances are tuned to certain spectral locations [105-107]. However, the resonance of the plasmonic nanoantennas, as it is shown in Figure 4.4B, is quite broad compared to the band edge emission of the 1L-WS₂. Therefore, small variations of the plasmon resonances have only a weak impact on this sharp band edge emission, as it was already observable in Figure 3.14. Nevertheless, this effect is investigated for the different circular polarization states and visualized in Figure 4.7. Here, the hybrid metasurface with plasmonic nanorods of 230nm length is chosen to be investigated for fundamental wavelengths ranging from 1210-1270 nm.

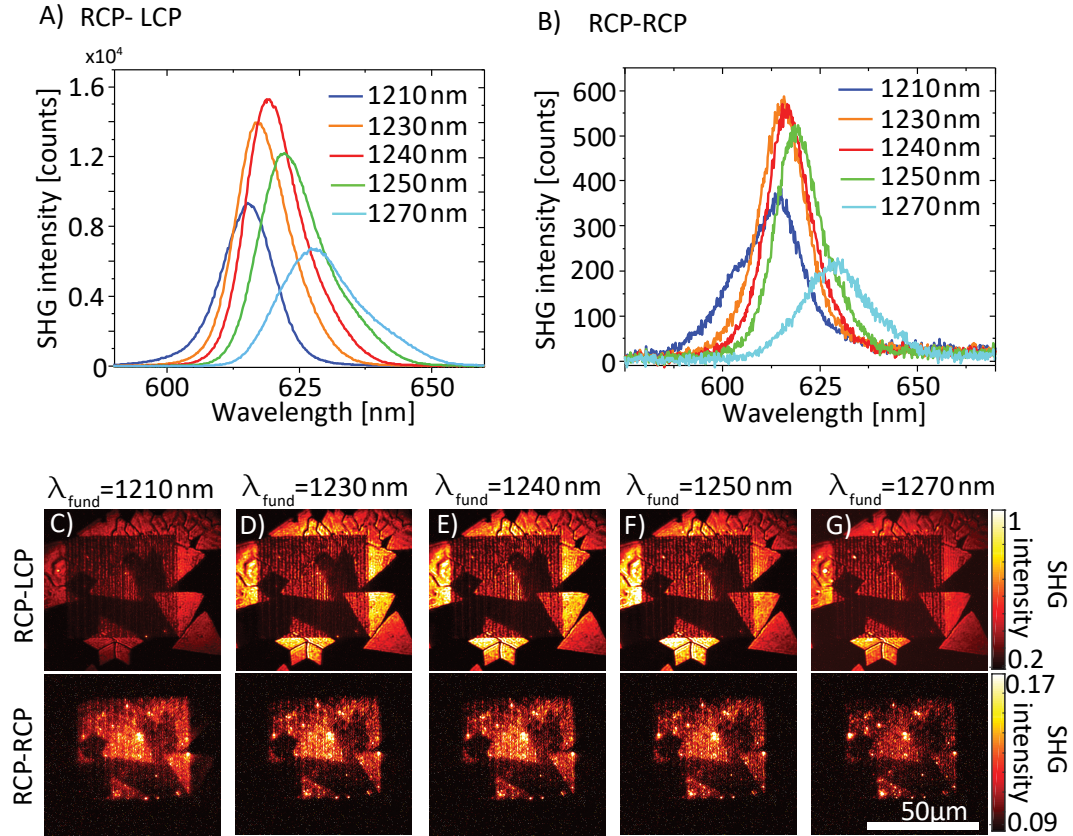


Figure 4.7: Wavelength dependence of the hybrid metasurface. (A) Obtained SHG of the hybrid metasurfaces spectra measured in the cross-polarization state σ^- . The strongest SHG is observed for a fundamental wavelength of 1240 nm. (B) Obtained spectra measured of the hybrid metasurfaces in the co-polarization state σ^+ . The curves show nearly the same wavelength dependence as for the cross-polarization state in (B) despite the lower intensity. (C-G) Spatially resolved SHG for the wavelength-dependent measurement in the range of $\lambda_{fund} = 1210$ -1270 nm measured in the cross-polarization state σ^- (RCP-LCP) and the co-polarization state σ^+ (RCP-RCP). A similar image can be found in [102].

The measured spectra show, that for the SHG measured in the cross-polarization state σ^- , the strongest signal arises for a fundamental wavelength of 1240 nm (Figure 4.7A). The corresponding spatially resolved SHG images in Figure 4.7C-G (top row) show, that most of the measured SHG signal at this wavelength arises from the 1L-WS₂ flakes around the hybrid metasurface, which do not have plasmonic nanoantennas on top. For this polarization state, it can be concluded, that most of the SHG originates mostly from solely 1L-WS₂. It is noticeable, that the strongest SHG signal

is not detected at a fundamental wavelength of 1230 nm but rather for 1240 nm, which does not correspond to half of the band gap energy measured in the PL spectra (Figure 4.3E). Nevertheless, a SHG signal of similar strength is measured for an excitation wavelength of 1230 nm. Compared to this, the SHG signals in the co-polarization state σ^+ have lower intensities (Figure 4.7B), but show a similar wavelength dependency as for the cross-polarization state σ^- . As the spatially resolved SHG images in Figure 4.7C-G (bottom row) show, the SHG measured in this polarization state is only created by the hybrid metasurface. The nearby 1L-WS₂ flakes without plasmonic nanoantennas on top do not provide any SHG signal. For this configuration, the strongest SHG signal is observable for a fundamental wavelength of 1230 nm, which is slightly blue-shifted compared to the contrary polarization state. Since the plasmonic nanoantennas have a resonance at 1200 nm, this can result in a shift for the highest SHG efficiency. To obtain an even greater SHG signal in the co-polarization state, one might optimize the length of the plasmonic nanorods to achieve a better polarization and frequency conversion efficiency. However, the overall efficiency for the SHG generated in the co-polarization state σ^+ for this hybrid metasurface is calculated to around 10^{-13} for a fundamental wavelength of 1240 nm.

4.4.3. Power dependency

Due to the strong pump intensity of the fundamental beam, a two-photon absorption can occur, which would result in the emission of PL-light by the recombination of excited excitons at wavelengths corresponding to the band gap energy, which is called two-photon luminescence (TPL). This effect occurs, when the summed energy of the two absorbed photons is higher than the band gap energy, which allows the exciton excitation by two-photon absorption. This process can be observed in the nonlinear spectrum obtained for an excitation wavelength of 1210 nm in the co-polarization state (Figure 4.7B). Here, the dominating process is still SHG, but the left half of the signal peak is deformed, hinting that a TPL process might take place. This process becomes more dominant if the 1L-WS₂ is excited with even shorter wavelengths and was already observed discussed in chapter 3.3.3 briefly. Figure 4.8 shows the obtained nonlinear signals of solely 1L-WS₂ without plasmonic nanoantennas on top for excitation wavelengths of 1150-1200 nm. The spectra show a clear peak splitting of the nonlinear signal, where one peak of the signal shifts to lower SHG wavelengths for shorter excitation wavelengths. Meanwhile, the other peak in the spectrum stays at the same

wavelength of around 613 nm, which equals the band gap energy of 1L-WS₂, hinting, that some of the absorbed photons are emitted as PL-light.

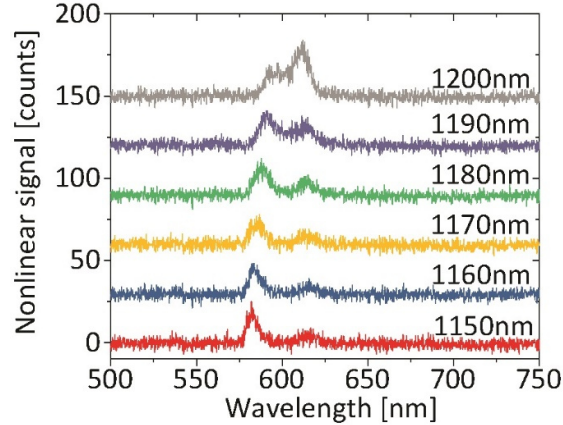


Figure 4.8: Two-photon emission. Visualization of the peak-splitting due to two-photon luminescence. The spectra show the nonlinear signal obtained for 1L-WS₂ under NIR excitation for wavelengths lower than 1230nm, which equals half of the band gap energy of 1L-WS₂.

However, the spectral width (measured at full width half maximum) of the measured SHG signals is a convolution of the laser spectrum and the instantaneous spectral nonlinear response function. In comparison, the PL spectra have only half of the spectral width, since it is only determined by the exciton lifetime and the inhomogeneous broadening. To exclude any saturation effects due to the strong excitation, a power-dependent measurement is done, where the SHG signal strength is measured for varying power levels of the excitation laser beam. The results of this measurement, done at an excitation wavelength of 1240 nm, are shown in Figure 4.9.

As a power-dependent measurement is delicate, because a too high power of the illumination beam may not only result in saturation but could also lead to a damaged sample, it is done for low laser powers. By doing so, the region of finite carrier concentration in the 1L-WS₂ or heating effects of the gold nanoantennas are avoided. For this kind of measurement, a power-dependent relation of the SHG signal $I_{SHG} \propto P^2$ is expected, where P denotes to the incident laser power. The spatially resolved SHG images in Figure 4.9A as well as the extracted power-dependent SHG signals in Figure 4.9B obtained for each polarization state confirm our expectations, despite small deviations. The polynomial function fitted to the data of the power-dependent SHG signals on a double logarithmic scale provide a slope of 2.08 for the cross-polarization state σ^- and a slope of 2.41 for the co-polarization state σ^+ . In the ideal case, both

slopes should be around 2 to confirm a quadratic correlation, as it was expected. For the cross-polarization state this can be assumed, since the slope deviates only little from the expectations. Although the deviation for the co-polarization state is larger, it is still in the same regime and saturation effects can be excluded, which leads to the conclusion, that the damage threshold was not reached yet.

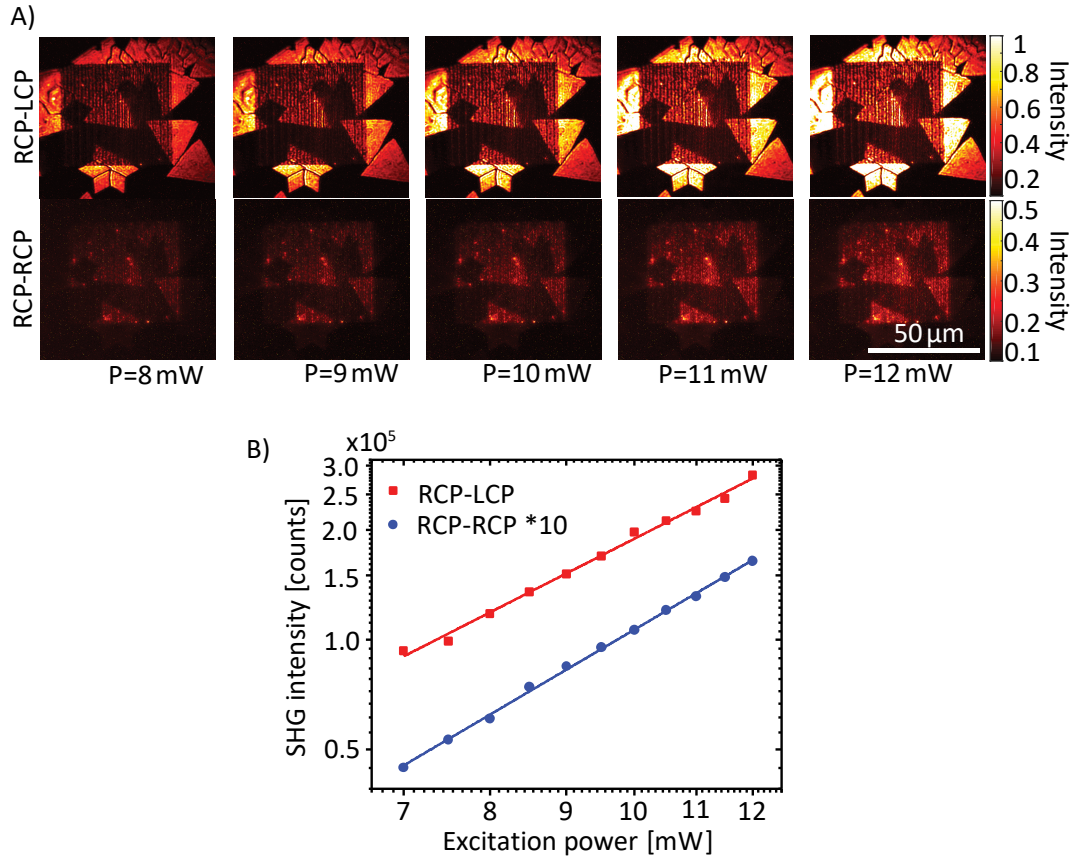


Figure 4.9: Power-dependent measurement of the SHG signals. (A) Spatially resolved SHG signal from the hybrid metasurface and the 1L-WS₂ flakes in cross-polarization state σ^- and co-polarization state σ^+ for different incident fundamental powers. **(B)** Extracted SHG intensities from the images in (A) versus the incident power for both polarization states. Note that the values for the SHG signal for the co-polarization state (blue dots) have been multiplied by the factor 10. The solid lines represent a polynomial fit to the measured values with the slope of 2.08 for the fit of RCP-LCP (σ^-) and 2.41 for the fit of RCP-RCP (σ^+). A similar image can be found in [102].

4.5. Spatial phase modulation

At this point, the spatial phase modulation via the plasmonic metasurfaces is investigated. As it was exemplified previously in chapter 4.3, the hybrid metasurfaces were designed to implement a relative phase between the horizontal neighboring antennas by their incremental rotation angle of $\alpha = 70^\circ$ for eight consecutive nanoantennas. As this phase modulation is not visible in the PL-images (Figure 4.3A), it is visible as a vertical stripe pattern in any of the previously shown spatially resolved SHG images for either, the co- and cross-polarization state (e.g. Figure 4.9A). As equations (4.6) and (4.7) only predict a phase modulation for the co-polarization state σ^+ , no interference pattern in the cross-polarization state should be visible. However, this pattern might not arise due to the induced PB-phase but rather is a near-field coupling effect between neighboring antennas, where the individually rotated nanoantennas show a more complex interaction with each other. A similar effect was already shown in chapter 3, where near-field effects can give rise to different transmission levels in the NIR range (Figure 3.8) or open up the possibility for SHG due to an introduced inversion symmetry in the lattice structure (Figure 3.7C). However, this near-field coupling present in this special kind of hybrid metasurface is not yet fully understood and would need further investigations.

Here, the mechanism of PB-phase applied in hybrid metasurfaces is of special interest in this thesis. To further investigate this mechanism, two additional hybrid metasurfaces are fabricated. As stated before, the scattered light in the cross-polarization state σ^- carries the PB-phase corresponding to the nanoantenna rotation angle given by $\phi = 2\alpha$. The subsequent nonlinear process of SHG changes this phase to $\phi_{SHG} = 4\alpha$, as it is predicted by (4.7), which is now four times the rotation angle of the individual plasmonic nanorods. Note, that this phase information is now encoded in the co-polarized SHG beam σ^+ , since the SH generated by the 1L-WS₂ changes its helicity. To visualize the effect of this phase modulation in the co-polarization state of the SHG signal, a spatial phase modulation over the entire hybrid metasurface is introduced. Therefore, two additional hybrid metasurfaces are fabricated, where each metasurface contains two different spatially separated areas with different phase modulations to demonstrate a spatial interference of the SHG in the far-field. An SEM image of the fabricated plasmonic nanoantenna arrays is shown in Figure 4.10A.

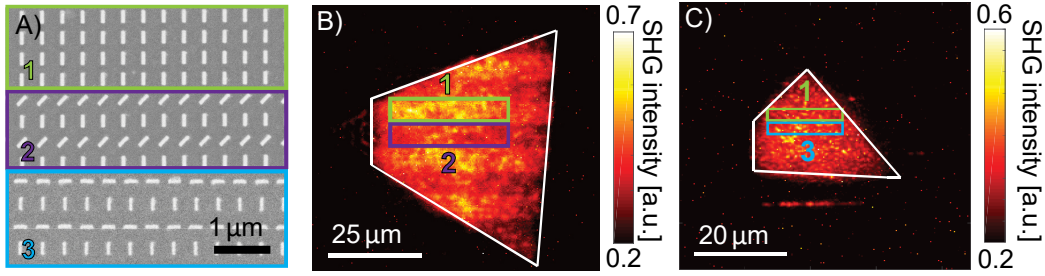


Figure 4.10: Spatial phase control of the SHG signal. (A) SEM image of the three distinct areas to generate different local phase distributions. In area 1 (marked in green) the plasmonic nanorods all have the same orientation. In area 2 (marked in purple) half of the antennas have the same orientation as the antennas in area 1. The other half (every second row) is rotated by an angle of $\theta=45^\circ$ resulting in an additional PB phase of $\varphi=180^\circ$. In area 3 (blue) the previously 45° rotated antennas are now rotated by $\theta=90^\circ$ resulting in an additional PB phase of $\varphi=360^\circ$. (B) SHG image of the plasmonic metasurface with alternating areas 1 and 2 on top of a 1L- WS_2 flake measured in copolarization state σ^+ . The marked areas (green and purple) correspond to the areas with constructive and destructive interference, respectively. (C) SHG image of the plasmonic metasurface with areas 1 and 3 on top of a 1L- WS_2 flake measured again in copolarization state σ^+ . Note that the white framed areas in (B) and (C) mark the hybrid metasurface area. Note, that the positions of the areas 1 and 3 cannot be identified by the spatially resolved SHG images. Therefore, they are estimated by the position of the plasmonic metasurface relatively to the 1L- WS_2 flake. A similar image can be found in [102].

The first hybrid metasurface consists of plasmonic nanoantenna arrays as they are pictured in Figure 4.10A and marked with 1 (green) and 2 (purple). In area 1, all antennas are not rotated at all and therefore, no phase modulation is present ($\phi_{SHG} = 0$). In the second area (2) the nanoantennas in every second row are rotated by 45° , which results in a phase shift of ($\phi_{SHG} = 4 \cdot 45^\circ = 180^\circ$). The two opposite phase shifts in the two different rows lead to destructive interference of the SHG in the far-field, resulting in an attenuated SHG compared to the SHG arising from area 1. In contrast to this, the second hybrid metasurface also contains nanoantenna arrays, which are arranged as depicted in area 1 having a phase shift of $\phi_{SHG} = 0$. However, in the other area the nanorods are arranged as depicted in area 3 marked in blue. Here, every second row consists of nanorods rotated by an angle of 90° , which results in a phase shift of $\phi_{SHG} = 4 \cdot 90^\circ = 360^\circ$. The resulting SHG signals from these two rows interfere constructively in the far-field since they both should have the same phase. Concluding,

the SHG arising from this second hybrid metasurface should show no difference between area 1 and area 3, since every SHG signal should carry the same phase.

To investigate the implementation of the PB-phase as described, the spatially resolved SHG for the first hybrid metasurface containing areas 1 and 2 is measured in the co-polarization state σ^+ . The corresponding spatially resolved SHG image is shown in Figure 4.10B, where the areas 1 and 2 are highlighted. The spatially resolved SHG image shows a clear stripe pattern, where the comparison between areas 1 and 2 provides a clear intensity difference. Although the destructive interference in area 2 is clearly visible, the intensity does not fully cancel out but drops rather by a factor of nearly 2 compared to the SHG arising from area 1. This leads to the conclusion, that the PB-phase can be transferred to the SHG originating in the 1L-WS₂, but that additional effects are present in this polarization state, that lead to a non-perfect cancellation of the SHG. A similar phenomenon was already observed previously, when SHG was observable in polarization states, that are usually forbidden (Figure 3.9). Thus, near-field coupling effects might also generate other phase components, leading to an imperfect cancellation. The spatially resolved SHG image of the second hybrid metasurface, shown in Figure 4.10C, provides further information about the effect of the PB-phase on the SHG. For this hybrid metasurface, no spatial intensity modulation in the far-field is expected, since all SHG generated in the two distinct areas 1 and 3 should carry the same phase. As the results show, this expectation is fulfilled and no intensity modulation is visible in the experimental results.

In the previously investigated hybrid metasurfaces, introduced in chapter 4.3, a spatial phase modulation in the cross-polarization state σ^- was observed, although the theoretical calculations didn't predict any. To check this circumstance for the recently discussed hybrid metasurfaces, Figure 4.11 shows the spatially resolved SHG images for the cross-polarization state σ^- . As the spatially resolved SHG images of the two additional hybrid metasurfaces obtained in the cross-polarization state σ^- show, no spatially modulated SHG is observable, which is in good accordance with the predictions, gained from the theoretical calculations made in chapter 4.1. This underlines the previously made assumption, that the observed phase modulation for the hybrid metasurfaces in the cross-polarization state σ^- , shown in chapter 4.4, are more likely caused by complex near-field interactions between neighboring antennas and do not originate from the implementation of the PB-phase.

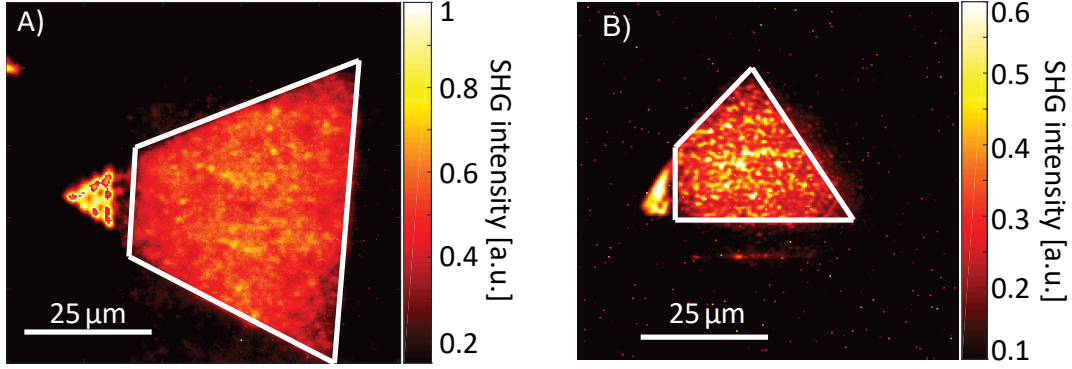


Figure 4.11: SHG measurement of the cross-polarization state σ^- (A) SHG image of the same flake as shown in Figure 4.10B but measured in the cross-polarization state σ^- . This polarization state does not carry the PB phase information and therefore no interference effect is observable. (B) SHG image of the same flake as in Figure 4.10C also measured in the cross-polarization state σ^- . This polarization state does not carry any phase information and therefore no spatial interference effect is observable.

4.6. Hologram encoded in hybrid metasurfaces

4.6.1. Pancharatnam-Berry phase in nonlinear harmonic generation

It was illustrated in Table 1, that different plasmonic nanoantennas can generate nonlinear harmonics of higher-order, based on their individual rotational symmetry. While the PB-phase of all plasmonic nanoantennas is given by twice the rotation angle of the individual nanoantenna in the linear regime, this changes in the nonlinear regime. Under circularly polarized illumination $\vec{E}_{L/R}$ (see equation (4.2)), an effective nonlinear dipole moment

$$\vec{P}_\alpha^{n\omega} = \beta_\alpha (\vec{E}^\sigma)^n \quad (4.8)$$

is formed [51], where β_α is the n -th harmonic nonlinear polarizability tensor of the nanostructure with an orientation angle of α . At this point, a second coordinate system coexisting next to the laboratory frame (x, y) is introduced, where the local coordinate axes are rotated by the angle α and denoted with (x', y') . A visualization is shown in Figure 4.12A.

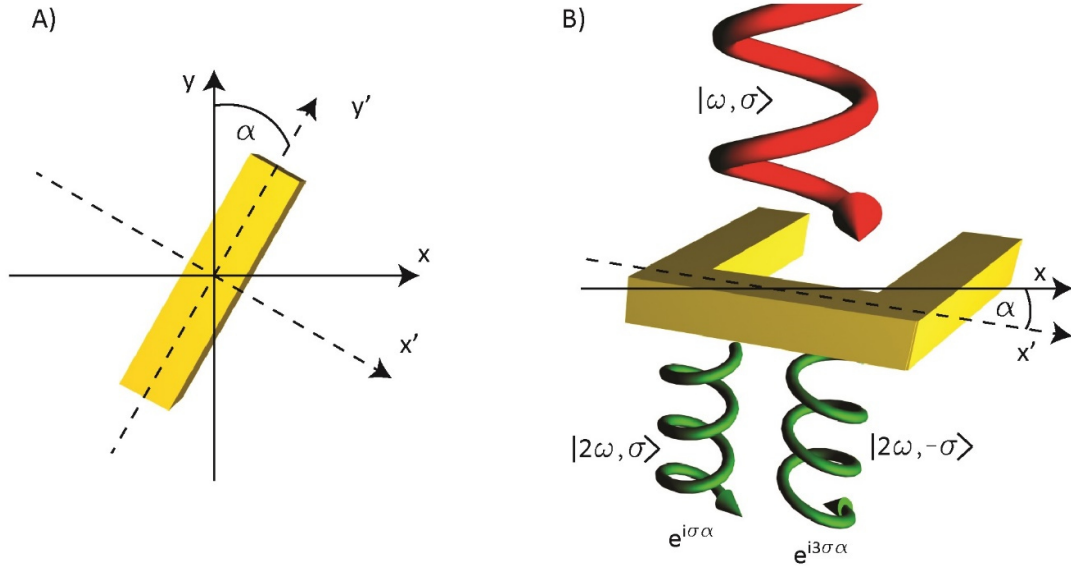


Figure 4.12: Schematically illustration of the nonlinear geometrical PB-phase (A) Rotated plasmonic nanoantenna by angle α in respect to the laboratory frame. (B) A plasmonic nanoantenna with a one-fold rotational C_1 symmetry, which induces a phase shift of $1\sigma\alpha$ and $2\sigma\alpha$ in the co- and cross-polarized light beam, respectively. A similar image can be found in [51].

The fundamental E-field can be transformed into the new coordinate system, leading to

$$\vec{E}_L^\sigma = \vec{E}^\sigma e^{i\sigma\alpha}, \quad (4.9)$$

where the index 'L' refers to the nanostructures local coordinate system. Thus, the n -th harmonic nonlinear polarizability tensor, given by equation (4.8), in the local frame of the nanoantenna is $\beta_0 = \beta_\alpha|_{\alpha=0}$, leading to the nonlinear dipole moment

$$\vec{P}_{\alpha,L}^{n\omega} = \beta_0 (\vec{E}_L^\sigma)^n = \beta_0 (\vec{E}^\sigma)^n e^{in\sigma\alpha}. \quad (4.10)$$

Further, this nonlinear dipole moment can be expressed as a superposition of two rotating dipoles, which correspond to the left- and right-circular polarization states ($\sigma = 1$ and $\sigma = -1$), as

$$\vec{P}_{\alpha,L}^{n\omega} = \vec{P}_{\alpha,L,\sigma}^{n\omega} + \vec{P}_{\alpha,L,-\sigma}^{n\omega}, \quad (4.11)$$

where, $\vec{P}_{\alpha,L,\sigma}^{n\omega}$ and $\vec{P}_{\alpha,L,-\sigma}^{n\omega}$ are proportional to $e^{in\sigma\alpha}$. The back transformation of these dipole moments into the laboratory coordinate system provides the final terms

$$\vec{P}_{\alpha,\sigma}^{n\omega} = \vec{P}_{\alpha,L,\sigma}^{n\omega} e^{-i\sigma\alpha} \propto e^{(n-1)i\sigma\alpha} \quad (4.12)$$

and

$$\vec{P}_{\alpha,-\sigma}^{n\omega} = \vec{P}_{\alpha,L,-\sigma}^{n\omega} e^{i\sigma\alpha} \propto e^{(n+1)i\sigma\alpha}. \quad (4.13)$$

The nonlinear polarizabilities of plasmonic nanoantennas can therefore be written as

$$\beta_{\alpha,\sigma^+} \propto e^{(n-1)i\sigma\alpha} \quad (4.14)$$

and

$$\beta_{\alpha,\sigma^-} \propto e^{(n+1)i\sigma\alpha}. \quad (4.15)$$

Note, that σ^+ and σ^- correspond to the co- and cross-polarization state in respect to the circular polarization state of the fundamental wave. Finally, the geometric phases accumulate to $(n-1)\sigma\alpha$ and $(n+1)\sigma\alpha$ and represent the nonlinear PB-phases for the co- and cross-polarized beam. As it was already described in chapter 2.2.2, plasmonic nanoantennas only allow the harmonic generation order of $n = lm \pm 1$, described by equation (2.32) [51, 108]. Figure 4.12B depicts the harmonic generation of second-order in plasmonic nanoantennas with a one-fold rotational C1 symmetry and the two different phase modulations of $\alpha\sigma$ and $3\alpha\sigma$ in the co- and cross-polarization state, respectively. Further, Table 3 shows the phase modulation of plasmonic nanoantennas with a C1, C2 and C3 rotational symmetry for different harmonic orders in the co- and cross-polarization state.




Harmonic order n	Sign of σ	C1	C2	C3
				
1	+			
	-	$2\alpha\sigma$	$2\alpha\sigma$	
2	+	$\alpha\sigma$		
	-	$3\alpha\sigma$		$3\alpha\sigma$
3	+	$2\alpha\sigma$	$2\alpha\sigma$	
	-	$4\alpha\sigma$	$4\alpha\sigma$	

Table 3: Phase modulation of plasmonic nanoantennas for different rotational symmetries and harmonic orders. Here, n represents the order of the harmonic process, α the rotation angle of the individual nanoantenna and σ the circular polarization state. A similar table can be found in [2].

4.6.2. Fresnel-approximation of diffraction

By utilizing the PB-phase, complex phase information can be implemented into a hybrid metasurface. As it was shown in the previous chapter 4.5, local phase differences induced by the plasmonic nanoantennas lead to constructive and destructive interference in the far-field. This principle can be utilized to realize a complex diffraction pattern, like so-called holographic images. To implement a hologram into a metasurface, a more detailed description of the diffraction is needed, which is done in the following by the Fresnel approximation. In general, nanostructures and metasurfaces can be of various shapes. Therefore, the description of their shape (and therefore the diffraction area) is done by a non-specific aperture δ . If such an aperture is illuminated by a light source located at L , the diffraction of the light at the metasurface plane $E_M(x, y, z = 0)$ leads to an intensity distribution at the image plane $E_P(x', y', z = z_0)$. This distribution is unique for different aperture shapes. A schematic illustration of the different planes and the beam propagation is shown in Figure 4.13.

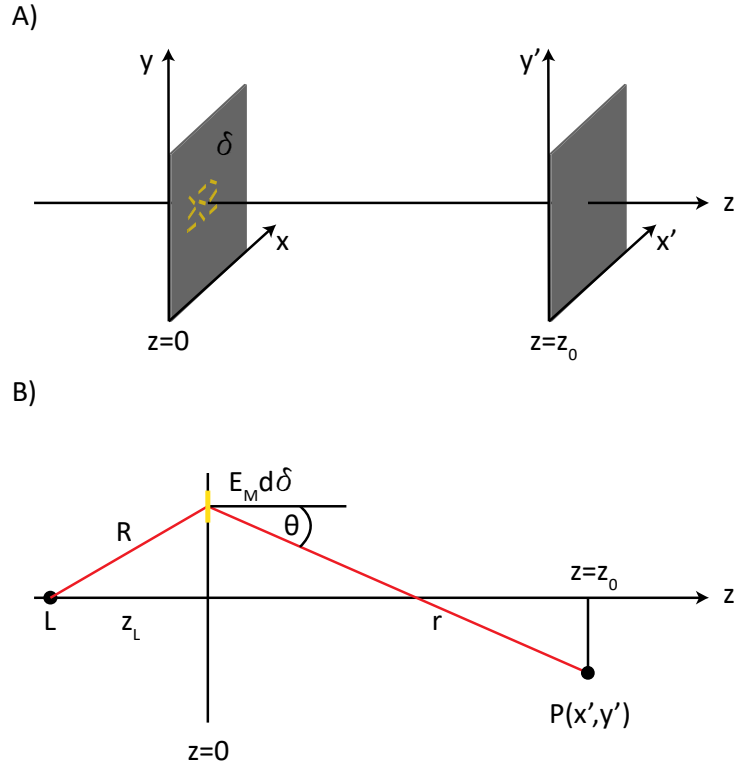


Figure 4.13: Schematically illustration of the Fresnel diffraction. (A) Illustration of the metasurface plane at $z = 0$ and holographic image plane at $z = z_0$. **(B)** Illustration of light beam propagation. A similar image can be found in [109].

At the metasurface plane, the E-field can be described as

$$\vec{E}_M(x, y) = \vec{E}_0(x, y)e^{i\phi(x, y)}, \quad (4.16)$$

which takes the characteristics of the illuminating source into account, such as a point light source, Gaussian beam, or plane wave. The light scattered at the infinitesimal element of area $d\delta(x, y)$ is described by the Huygens principle, resulting in an E-field distribution at point $P(x', y')$, given by

$$dE_P = C \cdot \frac{E_M d\delta}{r} e^{ikr}, \quad (4.17)$$

where r describes the distance between the aperture and the point $P(x', y')$ in the image plane, k the wave vector of the light beam and the factor C a proportional constant [109]. To calculate the overall E-field amplitude at the point $P(x', y')$, the integral over the whole aperture is calculated, given by

$$\vec{E}_P = \iint C \cdot E_S \frac{e^{ikr}}{r} dx dy. \quad (4.18)$$

The equation (4.18) is called the Fresnel-Kirchhoff diffraction integral, describing the E-field distribution generated by the illumination of a diffracting aperture at a plane in a certain distance r . An approximation can be applied, if $r \gg \delta$ is valid, resulting in $z_0 \approx r$ and $C \approx i/\lambda$ [109]. However, since the phase of the E-field is very sensitive to r , this approximation cannot be applied for the exponent. Hence, a Taylor expansion is considered, given by

$$r = \sqrt{z_0^2 + (x - x')^2 + (y - y')^2} \approx z_0 \left(1 + \frac{(x - x')^2}{2z_0^2} + \frac{(y - y')^2}{2z_0^2} + \dots \right), \quad (4.19)$$

changing the Fresnel-Kirchhoff diffraction integral to

$$\vec{E}_P(x', y', z_0) = \frac{i}{\lambda z_0} e^{ikz_0} \int_{-\infty}^{\infty} \int_{-\infty}^{\infty} E_M(x, y) \cdot e^{\frac{ik}{2z_0}((x-x')^2 + (y-y')^2)} dx dy. \quad (4.20)$$

This integral can also be written as

$$\begin{aligned} \vec{E}_P(x', y') &= \frac{C e^{ikz_0}}{z_0} e^{\frac{ik}{2z_0}(x'^2 + y'^2)} \\ &\cdot \int_{-\infty}^{\infty} \int_{-\infty}^{\infty} E_M(x, y) e^{\frac{ik}{2z_0}(x^2 + y^2)} e^{\frac{ik}{z_0}(xx' + yy')} dx dy, \end{aligned} \quad (4.21)$$

showing, that the E-field distribution in the image plane can be calculated by a Fourier-transformation of the E-field in the object plane [110-112]:

$$\vec{E}_P(x', y') = \frac{i e^{ikz_0}}{\lambda z_0} \cdot \mathcal{F} \left[E_M(x, y) e^{\frac{ik}{2z_0}(x^2 + y^2)} \right] \cdot e^{\frac{ik}{2z_0}(x'^2 + y'^2)}. \quad (4.22)$$

4.6.3. Computer-generated holograms

Historically, the first phase holograms were recorded in a medium, in which a reference beam interferes with an object beam forming an interference pattern. Hereby, only the object beam carries phase information of an object acquired by the interaction with a real object. Equation (4.22) can now be used, to calculate phase profiles for metasurfaces, which can reconstruct holographic images under illumination. In 1966, Brown and Lohmann invented the so-called computer-generated holograms (CGHs) making the presence of real objects unnecessary [113]. As a result, any virtual object now can be reconstructed by a calculated hologram using different kinds of media, such as spatial-light modulators or metasurfaces [1, 114-116]. The algorithm used here to calculate the hologram is based on a Gerchberg-Saxton algorithm developed in 1972. It is an iterative phase retrieval algorithm that can calculate a phase mask for a given intensity distribution at an image plane. This is done with the help of Fourier transformations, which represent the propagation between the hologram and the image plane.

A basic implementation of the Gerchberg-Saxton algorithm is depicted in Figure 4.14. In the first step, an initial random phase distribution is inserted into the algorithm and multiplied with the illuminating E-field. For an incident plane wave, the amplitude is given by $A_0 = 1$. The resulting E-field distribution E_n is then Fourier transformed, which represents the wavefront propagation into the image plane. Afterward, the amplitude of the target image I_T (image of the virtual object) is inserted into the previously obtained E-field distribution, calculated by the Fourier transformation (FT), and replaces the amplitude $A_{Im} = A_T$. Subsequently, an inverse FT is done, which represents a backpropagation to the hologram plane. At this state, the gained E-field distribution E'_H already represents a hologram, which has encoded phase information of the target image. Nevertheless, a reconstruction of this hologram would lead to a bad-quality copy of the target image. Therefore, the amplitude of this E-field distribution is set to the original illuminating E-field distribution (e.g. plane wave) and the described loop is done N more iterations. There are several abbreviations of this algorithm, where for example another illumination distribution away from the plane wave is taken into account, a first guess phase distribution is considered or a weight function of the acquired image after the first FT is introduced, which all aim at a better reconstruction image quality [117, 118]. However, the presented plasmonic metasurfaces can provide multiple phase modulations opening up the possibility to encode more than one target image into a single metasurface. Although this circumstance makes the application of holography in hybrid metasurfaces even more attractive, the implementation of more than one image into the same phase profile is more challenging.

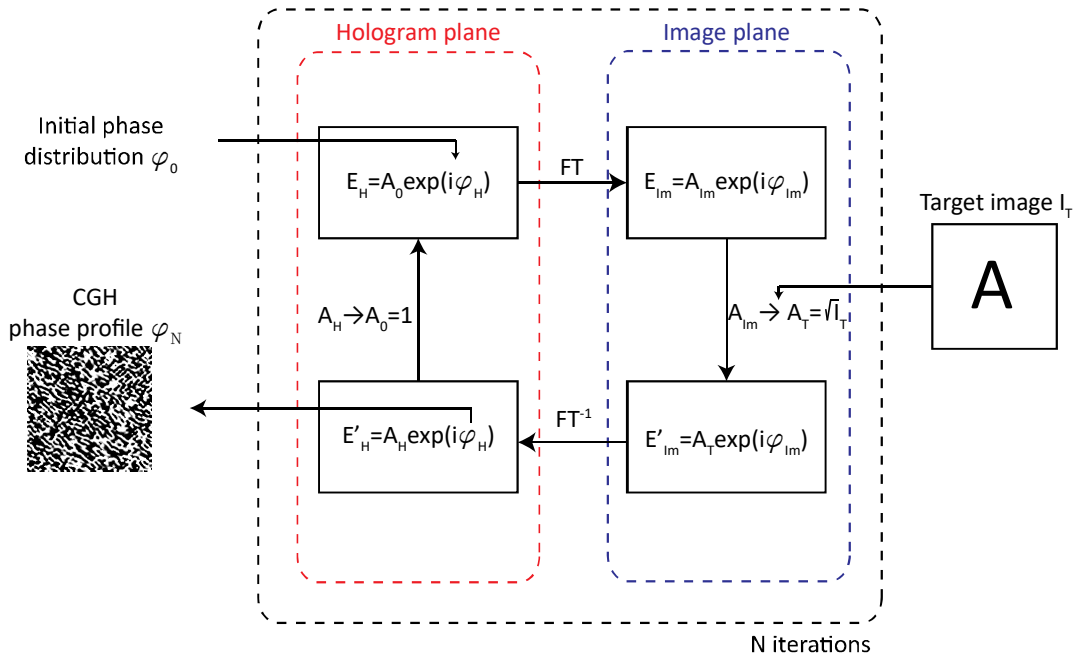
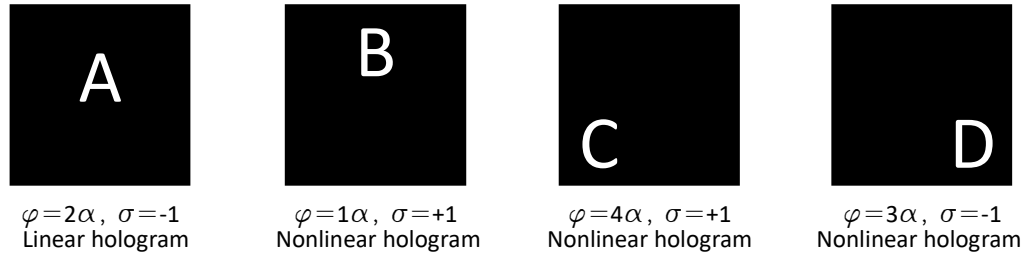


Figure 4.14: Schematically representation of the Gerchberg-Saxton algorithm. This phase retrieval algorithm calculates a phase distribution φ_N for a given target image I_T with the help of Fourier transformations, which represent the forward (FT) and backward propagation (FT⁻¹) between the hologram and the image plane.

For the implementation of several holographic images into a single hybrid metasurface, plasmonic nanoantennas with a one-fold rotational C1 symmetry are chosen. As Table 3 shows and Figure 4.12B depicts, such nanostructures provide three different phase modulations. In the linear regime, a phase modulation of 2α in the cross-polarization state is present. Additionally, two phase modulations of 1α and 3α in the case of SHG for the co- and cross-polarization state can be observed, respectively. In addition to these three phase modulations, it was shown in chapter 4.5, that hybrid metasurfaces with plasmonic nanorods provide a phase modulation of 4α in the co-polarization state of the SHG. Therefore, four different kind of phase modulations are providing the possibility of encoding four different holographic images into a single hybrid metasurface with C1 nanoantennas. Note, that three out of four images originate from the plasmonic metasurface solely, whereas the fourth only appears in its hybrid application with 1L-WS₂. For simplicity, the alphabetical letters A-D are chosen as images for the four phase modulations of the hybrid metasurface. To increase the contrast of the letters' holographic images, a black background is added, so that less to no light is

scattered into the area around the letters. The assignment of the letters to the phase modulation and the corresponding polarization state is depicted in Figure 4.15A.

A)



B)

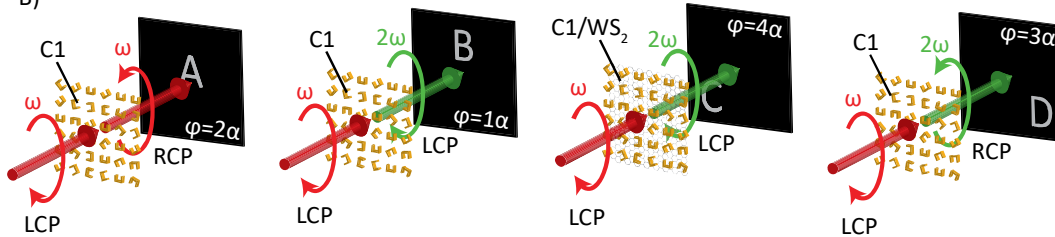


Figure 4.15: Hologram design (A) Assignment of the letters' holographic images to the corresponding phase modulations. Hereby, α is the nanoantennas rotation angle and $\sigma = \pm 1$ correspond to the co- or cross-polarization state in which the image is generated under circular polarization excitation. **(B)** Schematic illustration of the hologram reconstruction. The letter A is measured in the linear regime whereas the letters B-D are measured in the nonlinear regime of SHG. Of special interest is the hologram of the letter C, which results from the coupling of the C1 plasmonic nanoantennas to the 1L-WS₂.

Figure 4.15B illustrates schematically illustrations of the hologram reconstruction for the four different phase manipulations. It is shown, that three out of four holograms are reconstructed as SHG holograms in the nonlinear regime (letters B-D), whereas only the holographic image of the letter C arises due to the coupling of the C1 plasmonic nanoantennas to the 1L-WS₂. Note, that a special case are the holographic images of the letters B and C. Since all other holographic images are separable by either their wavelength or their polarization state, these two images appear in the same polarization state in the case of SHG. Thus, a spatial separation among the two letters is considered,

so that they can be distinguished from each other in the measurements since it is likely that both images do not provide the same signal strength.

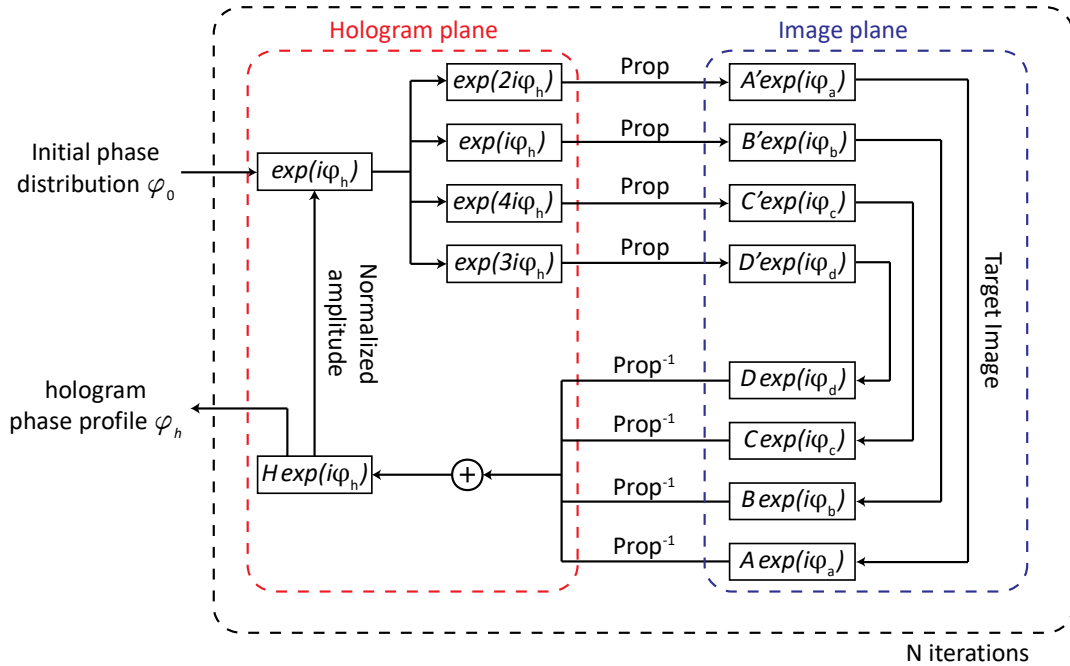


Figure 4.16: Flow chart of the expanded Gerchberg-Saxton algorithm for calculating a single phase profile considering four different phase modulations. The notation ‘Prop’ and ‘Prop⁻¹’ refers to the forward and backward propagation described by the equation (4.22).

As the Gerchberg-Saxton algorithm, depicted in Figure 4.14 is only capable of calculating the phase profile of one image at a time, it needs to be expanded for the implementation of four phase modulations into a single phase profile. Figure 4.16 represents a flow chart of the optimization method for generating the desired phase profile out of four different holographic images. First, a random phase profile φ_0 composed of 166x166 pixels is generated for the initialization in regard to the 166x166 plasmonic nanoantennas contained in the metasurface. After the initialization, the phase values are multiplied by 2,1,4 and 3 to consider the different phase modulations in the hybrid metasurface. Afterward, the E-field distributions are propagated into forward direction described by the Fresnel-approximation as defined in equation (4.22). Subsequently, the four different target images are set as new amplitude values for the four different phase modulations. Here, an expansion is implemented additionally, which increases the

signal-to-noise ratio of the alphabetical letter to its surrounding area. We call this expansion frame expansion. This expansion only takes a fraction of the target image of the alphabetical letters and set them as new amplitude values. By doing this, most of the noise is collected in the outer area of the target image, whereas the area close to the alphabetical letter has less noise [119]. After that, an inverse propagation is done and the four different complex amplitude distributions are summed up. The resulting phase distribution is regarded as the hologram [76]. For the next iteration step, the amplitude of the E-field distribution is normalized again the algorithm restarts for N iterations.

4.6.4. Theoretical reconstruction of holographic images

During the calculation of the phase profile via the Gerchberg-Saxton algorithm, the four different images corresponding to the phase modulations of 2α , 1α , 4α and 3α , shown in Figure 4.15, can be extracted before the last backpropagation after the N th iteration. The theoretically obtained holographic images are shown in Figure 4.17.

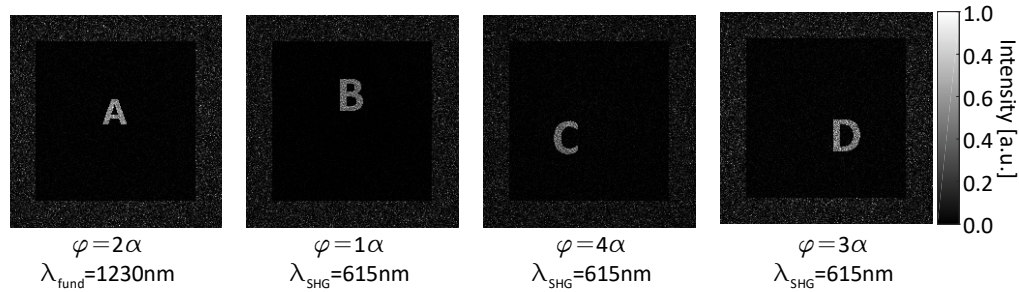


Figure 4.17 Theoretical reconstruction of the four holographic images. Calculated holographic images for the four different phase modulations of 2α , 1α , 4α and 3α corresponding to the four images of the alphabetic letters A-D, shown in Figure 4.15. The images are labeled with the corresponding phase modulation and wavelength.

By looking at the calculated reconstructed holographic images it stands out, that the alphabetical letters A-D are clearly visible and less to no noise is visible in the area around the letters. Therefore, it can be concluded, that the encoding of the four different images into a single phase profile via the expanded Gerchberg-Saxton algorithm was successful. Further, the black background in the area around the letters,

which is the result of the frame expansion, is visible and increases the contrast between the letters and any noise. This is supported by an increased noise visible in the outer area of the images. A common approach to evaluating the visibility in such holographic images is the calculation of the signal-to-noise ratio (SNR), given by

$$SNR = \frac{I_{Signal}}{I_{Noise}}. \quad (4.23)$$

Here, I_{Signal} is the peak signal strength of the individual alphabetical letters and I_{Noise} the mean signal strength of the background obtained from the black area around the letter. The corresponding values were extracted from the calculated holographic images, shown in Figure 4.17, in the corresponding areas. The obtained SNR values for the four different holographic images are determined to $SNR_A^{Calc} = 804$, $SNR_B^{Calc} = 216$, $SNR_C^{Calc} = 87$ and $SNR_D^{Calc} = 153$, stating, that the holographic image of the letter A in the linear regime has the best visibility, which drops in the nonlinear regime by more than a factor of four. However, the SNR calculated for theoretically obtained results is only meaningful to a limited extend. From experience, these values are much larger than the SNR values obtained from experimental results. Previous studies reported an SNR of about 25 the experimental results for holograms measured in the linear regime.

4.6.5. Linear optical characterization

For the experiments, two plasmonic metasurfaces are fabricated with the same procedure as it is described in chapter 4.2, where one is fabricated on top of 1L-WS₂ and the other one is fabricated on a glass substrate as a reference sample. The nanoantennas are designed to be resonant at a fundamental wavelength of 1230 nm and therefore, the nanoantennas dimensions are chosen similar to the dimensions, depicted in Figure 3.15A. After the fabrication, SEM-images and transmission spectra are taken again, which results are shown in Figure 4.18. The transmission spectra show, that their plasmon resonances are located at 1180 nm and 1350 nm for the hybrid metasurface and reference sample, respectively. It stands out, that these resonances are not located at 1230 nm as intended, which is most likely the result of uncertainties in the fabrication process. These uncertainties in the fabrication process arise due to the comparatively low size of the structure. As the width of the antenna arms is designed to be around 30 nm, the limit of the EBL-system is just around that scale. Therefore, any small

abbreviation in the fabrication process might result in nanoantennas with different dimensions and plasmon resonances. Nevertheless, the natural width of the plasmon resonance still covers up the intended excitation wavelength, so that the linear and nonlinear experiments are done at a fundamental wavelength of 1230 nm.

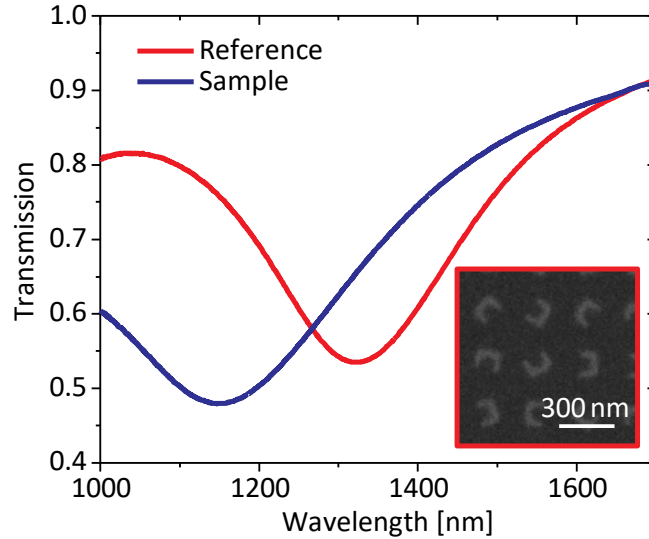


Figure 4.18: Sample Characterization. Transmission spectra of the fabricated hybrid metasurface (blue) and reference (red) sample. The inset shows an SEM-image of the plasmonic C1 nanoantennas obtained for the reference sample. No SEM-images are taken for the hybrid metasurface sample to avoid damaging the 1L-WS₂.

4.6.6. Experimental reconstruction of holographic images

First, the obtained holographic images of the bare plasmonic metasurface are investigated. Therefore, the setup illustrated in Figure 4.5 is used to reconstruct the images encoded in the bare plasmonic metasurface. For a left-circular input polarization, the linear and nonlinear holographic images are measured in the different polarization states, which are selected by the analyzer. The obtained results are shown in Figure 4.19. The results show, that the three holographic images of the letters A, B and D encoded in the phase modulation of 2α , 1α and 3α , respectively, are observable for the reference sample (Figure 4.19A-C). By comparing the intensities among each other, it stands out, that the holographic image A, encoded by the 2α phase modulation in the linear regime, has a better visibility than the holographic images of B and D in the

nonlinear regime of SHG. To quantify this observation, the SNR for each image is calculated again.

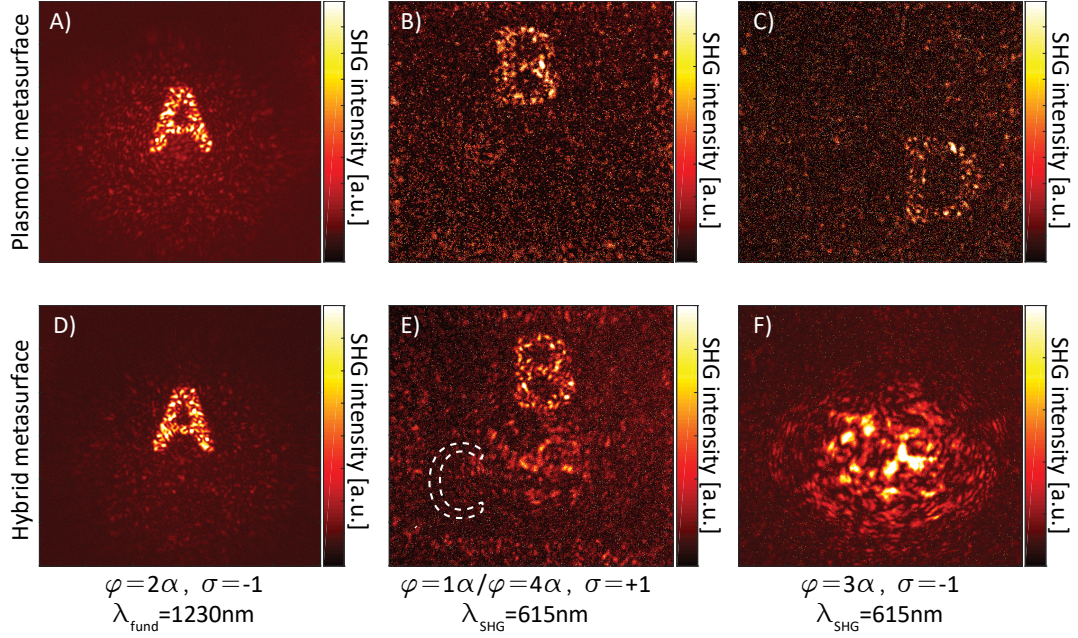


Figure 4.19: Reconstruction of holographic images. Measured holographic images in the (A) linear and (B-C) nonlinear case for the reference sample. Measured holographic images in the (D) linear and (E-F) nonlinear regime for the hybrid metasurface sample. The images are labeled with the corresponding phase modulation, wavelength and polarization state. The letter C, indicated by a white dotted line in Figure E, marks the area, where the additional holographic image for the phase modulation of 4α is expected for the hybrid metasurface.

They are determined to $SNR_A^{Ref} = 4.3$, $SNR_B^{Ref} = 2.0$ and $SNR_D^{Ref} = 1.8$ for the holographic images of A, B and D, respectively. These values underline the subjective observations, that the linear image of the letter A provides a better visibility than the other two images. Similar behavior is observable for the hybrid metasurface. Here, the holographic image of the letter A in the linear regime has also a better visibility than the holographic images in the nonlinear regime. Although the visibility of the letter B in the co-polarization state is comparable to the image taken for the reference sample, the additional holographic image of the letter C, which is expected for the hybrid metasurface case due to the 4α phase modulation, is not observable at all (Figure 4.19E). Instead, additional scattered SHG light is observed in the area below the image of the letter B, which is most likely arising due to the coupling of the plasmonic nanoantennas to the 1L-WS₂, leading to an SHG in different polarization states. However, the image reconstruction of the letter D in the cross-polarization state is even

worse. Here, a lot of SHG light is scattered into the area, where the D-image is expected, making it impossible to observe the reconstruction of the 3α phase modulation. This strong scattering light can be explained by the strong emission of SHG by the 1L-WS₂ in this polarization state, which was already observed previously, e.g. Figure 4.6. However, the SNR's of the two observable holographic images are determined to $SNR_A^{Sample} = 6.8$ and $SNR_B^{Sample} = 2.5$. By comparing these values to the SNR values determined for the reference sample, it stands out, that the SNR is increased for the hybrid metasurface sample. This is reasoned with the more resonant excitation of the plasmonic metasurface. Since the resonance wavelength of the nanoantennas fabricated on top of 1L-WS₂ is located at 1180 nm, their excitation with the fundamental wavelength of 1230 nm leads to higher absorption of the excitation light, than for the plasmonic nanoantennas fabricated on the glass substrate, where the plasmon resonance is located at 1350 nm. Comparing the SNR values to other studies, it stands out that they are of one magnitude lower than previous studies have reported ($SNR \sim 25$) [120]. This difference might arise due to the encoding of four different holographic images into a single phase profile, lowering the visibility of each image in the experiments.

However, to investigate the missing holographic images in Figure 4.19E-F, the experiment is redone for an excitation wavelength of 1180 nm to further increase the coupling to the plasmonic nanoantennas. As it was previously shown in Figure 3.14, the tuning of the excitation wavelengths away from the band gap of the 1L-WS₂ leads to a decreased SHG signal arising from the monolayer. The results are shown in Figure 4.20 and confirm the previously made assumption. The two reconstructed images show less scattered SHG light in the area around the holographic images arising from the 1L-WS₂ since the efficiency of SHG is much lower for this excitation wavelength. Nevertheless, the expected holographic image of the letter C implemented by the 4α phase modulation is still not visible for the cross-polarization state. This observation hints towards a very low nonlinear conversion efficiency of the hybrid metasurface in this polarization state, which results in a signal strength lower than the noise. This low nonlinear conversion efficiency of the hybrid metasurface can be lead back to the comparatively low polarization conversion efficiency of the plasmonic nanoantenna array into the cross-polarization state. This potential obstacle has already been stated for phase modulation applications in plasmonic metasurfaces in recent research [9, 13]. One approach to increase the nonlinear conversion efficiency of the hybrid metasurface might be a fine tuning of the plasmon resonance to a wavelength of 1230 nm, where the 1L-WS₂ shows a strong nonlinear response. By doing so, the polarization conversion efficiency of the plasmonic metasurface can be increased for this wavelength while making use of an increased nonlinear response of the 1L-WS₂. Another aspect is the

coverage of the plasmonic metasurface with 1L-WS₂ flakes. As only a fraction of the plasmonic metasurface is fabricated on top of 1L-WS₂, only this part contributes to the holographic image of the alphabetical letter C. In an ideal case, the whole plasmonic metasurface is placed onto 1L-WS₂ to maximize the nonlinear conversion efficiency. However, the growth of large area monolayer WS₂ is still challenging, where additional research might provide progress in the near future.

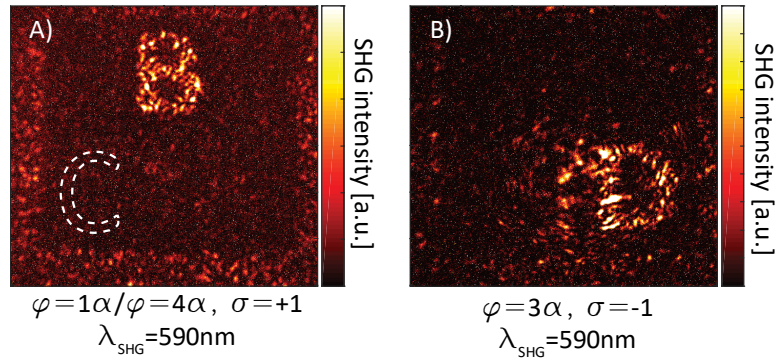


Figure 4.20: Reconstruction of holographic images at 1180nm excitation wavelength. Obtained holographic images nonlinear regime for the hybrid metasurface sample measured in the **(A)** co- and **(B)** cross-polarization state.

It is noteworthy at this point, that the effect of the frame expansion, which was visible in the theoretical reconstructed images, is only slightly visible in the image Figure 4.19E and Figure 4.20A. Here, a frame is only visible at the outer edges of the image due to the large magnification of the microscope objective.

4.7. Conclusion

In this chapter, spatially resolved SHG images of hybrid metasurface were investigated to visualize the coupling of the plasmonic metasurface to the 1L-WS₂. Further, the implementation of the linear and nonlinear Pancharatnam-Berry phase into hybrid metasurfaces was realized to illustrate a possible application for hybrid metasurfaces.

The results of the spatially resolved SHG measurement obtained for hybrid metasurfaces under excitation with circularly polarized light have shown, that an SHG signal can be emitted into a circular polarization state, that is usually forbidden by either bare plasmonic metasurface or solely 1L-WS₂. This observation is comparable to the results obtained for the excitation of a hybrid metasurface with linearly polarized light, shown

in chapter 3.3. For these experiments, also strong SHG signals can be observed in polarization states, where usually no SHG signal is expected for either bare plasmonic metasurface or solely 1L-WS₂.

Afterward, an implementation of the linear PB-phase shows a possible application to manipulate the SHG arising from plasmonic/TMDC hybrid metasurfaces and measured in the far-field. It was shown, that the SHG process in hybrid metasurfaces can be split into two separate processes, a linear transmission of the plasmonic nanoantenna array and the SHG process at the 1L-WS₂. With this consideration, constructive and destructive interference in the far-field by a careful choice of local phase modulation at the metasurface plane can be achieved. It was further suggested, that this coupling can be utilized to implement an even more complex phase modulation into hybrid metasurfaces. Therefore, a change of the plasmonic nanoantennas' rotational symmetry to a C1 rotational symmetry is done to encode four distinct holographic images into a single hybrid metasurface. Here, four simple holographic images of the alphabetic letters A, B, C and D were chosen to represent the phase modulation of 2α , 1α , 4α and 3α , respectively. For the calculation of the phase profile, an extended Gerchberg-Saxton algorithm was used, in which the phase profile for each holographic image was calculated separately and added together after every iteration step. Although the theoretical reconstruction of the holographic images provides a clear observation of all four alphabetic letters, only three out of four were observable for the hybrid metasurface in the experiments. The holographic image of the alphabetic letter C, which should only be present in the hybrid metasurface, was not observable. Since this holographic image is based on the coupling of the plasmonic metasurface to the 1L-WS₂, it is most likely that the nonlinear conversion efficiency of the hybrid metasurface for this holographic image results in a signal strength lower than the background noise.

5.SUMMARY AND OUTLOOK

This thesis is about the second-harmonic generation in hybrid metasurfaces consisting of plasmonic nanoantenna arrays made of gold and a single atomic layer of transition metal dichalcogenide. As a representative TMDC, WS_2 is chosen with a direct band gap in the visible regime. The investigations handle the second-harmonic generation for near-infrared excitation wavelengths with photon energies around half of the band gap energy of 1L- WS_2 at around 1 eV.

This thesis is motivated by the question, under which circumstances the nonlinear process of SHG can be enhanced for excitation wavelengths in the NIR regime and how this nonlinear response can be tailored utilizing plasmonic metasurfaces. In the framework of fundamental investigations, the impact of different parameters on the SHG is investigated. Thereby, the excitation polarization, the location of plasmon resonance as well as the influence of different symmetries in the lattice structure and individual nanoantennas are of special interest.

For the fundamental investigations, plasmonic nanoantenna arrays are fabricated in a first step onto a glass substrate, which contain nanoantennas with a two-fold rotational C_2 symmetry. Subsequently, the 1L- WS_2 is transferred onto the plasmonic metasurface. After the fabrication process, the linear properties of the hybrid metasurface are investigated and it was shown, that the plasmon resonances are located at half of the band gap energies of 1L- WS_2 as intended. Further, photoluminescence measurements confirm, that the transferred WS_2 layers are indeed of monolayer thickness. The subsequent polarization-dependent SHG measurements with linear polarized excitation light have shown, that the SHG is enhanced in polarization states, in which usually less to no SHG is expected for either, solely 1L- WS_2 or bare plasmonic metasurface. This enhancement can further be tuned by the choice of lattice arrangement, whereas plasmonic nanorods arranged in a hexagonal lattice structure show the greatest enhancement with a factor of more than 40. However, not for all linear polarization states an enhancement of the SHG is observable. For a better understanding, a

theoretical model describing the process of SHG in the presented hybrid metasurface is introduced. The results of the theoretical calculations show a good agreement with the experimentally obtained results and it can be seen, that the plasmonic nanorods have a shading-like effect resulting in an attenuated SHG emission, if the plasmonic nanorod is excited resonantly along its long axis.

This effect is further investigated for additional hybrid metasurfaces with shifted plasmon resonances. SHG measurements for these metasurfaces show, that a tuning of the plasmon resonances to shorter or longer wavelengths leads to an increased SHG signal for the same excitation wavelengths. The fundamental investigations are concluded by the study of different rotational symmetries of the individual plasmonic nanoantennas. As the previous investigations have shown, the introduction of a broken inversion symmetry via the lattice structure of the plasmonic nanoantenna array can lead to a significant SHG in bare plasmonic metasurfaces. Based on this observation, an additional broken inversion symmetry introduced in individual nanoantennas might result in an enhancement. The results show, that for hybrid metasurfaces with plasmonic nanoantennas of one- and three-fold rotational symmetry an enhancement of SHG can be observed compared to bare plasmonic nanoantenna array. However, the observed signal strength of the SHG is still lower than for solely 1L-WS₂.

Therefore, it can be concluded that an overall enhanced SHG in the presented hybrid metasurfaces was not observed, but rather an enhancement of SHG in polarization states, which are usually forbidden for either solely 1L-WS₂ or bare plasmonic metasurface. Further, the strength of the SHG signal can be tuned by the choice of symmetry present in the plasmonic nanoantenna array. It is shown, that an introduced broken inversion symmetry in the presented plasmonic metasurface leads to a stronger SHG emission compared to hybrid metasurfaces with present inversion symmetry.

After the fundamental investigations, the application of phase modulation for a tailored nonlinear response in hybrid metasurfaces via the geometric Pancharatnam-Berry phase is demonstrated. At this point, the fabrication process of the hybrid metasurfaces is reversed. Therefore, plasmonic metasurfaces with an implemented phase modulation are fabricated on top of CVD-grown 1L-WS₂, which were commercially bought. Subsequent photoluminescence measurements prove, that the band gap of the 1L-WS₂ is not changed significantly if the fabrication process is inverted. In a first investigation of the nonlinear response, spatially resolved SHG measurements show, that a strong co-polarized SHG signal can be obtained under circular illumination polarization, where usually no SHG is expected for either solely 1L-WS₂ or bare plasmonic metasurface. Further, the spatially resolved SHG images of the hybrid metasurfaces show a stripe pattern in the SHG emission in the co- and cross-polarization state. However, only a phase modulation in the co-polarization state induced by the plasmonic metasurface is

predicted. It can be reasoned, that the modulation most likely arises due to a more complex near-field coupling between the individual nanoantennas, which was already observable in the fundamental investigations. This is supported by additionally fabricated hybrid metasurfaces where the theoretical predictions of a phase modulation only visible in the co-polarization state of the SHG are in a good agreement with the experimental results. It is shown, that a local phase difference induced by individually rotated plasmonic nanoantennas leads to constructive and destructive interference in the spatially resolved SHG measured in the far-field.

This concept of phase modulation via the Pancharatnam-Berry phase is then extended to encode a more complex phase information pattern into a hybrid metasurface. The utilization of the linear and nonlinear Pancharatnam-Berry phase opens up the possibility to encode four different holographic images into a single hybrid metasurface. Therefore, a hybrid metasurface consisting of plasmonic nanoantennas with a C1 rotational symmetry is chosen, which offer one phase modulation in the linear regime and three phase modulations in the nonlinear regime of SHG. It is predicted, that three out of four holograms are observable for a bare plasmonic metasurface whereas the fourth hologram is only observable for the hybrid metasurface case. In the experiments, the reconstruction of the three holographic images for a bare plasmonic metasurface is shown successfully. However, the reconstruction of the four holographic images in the hybrid metasurface case proved to be more difficult, where two images were not observable. Deeper investigations have shown, that one of the missing nonlinear holographic images was hidden by noise, generated by the 1L-WS₂ in the same polarization state. It is made visible by a change of the excitation wavelength. However, it was not possible to reconstruct the other missing holographic image, which is expected only for the hybrid metasurface case. It is assumed, that the nonlinear conversion efficiency of the hybrid metasurface is too low for this configuration. A possible approach to increase this nonlinear conversion efficiency is a greater coverage of the plasmonic metasurface with 1L-WS₂, since only a fraction of the presented plasmonic metasurface was placed onto 1L-WS₂ flakes.

Overall, this thesis has presented an in-depth investigation of the SHG in plasmonic/1L-WS₂ hybrid metasurfaces under NIR-illumination near half the band gap energy of 1L-WS₂. Further, the application of tailored nonlinear optics via the geometric Pancharatnam-Berry phase was demonstrated successfully. Although the low conversion efficiency of the hybrid metasurface currently limits the implementation of complex phase information, researchers have already proven, that this obstacle can be overcome for bare plasmonic metasurfaces. A possible alternative to the presented hybrid metasurfaces may lie within the replacement of the plasmonic nanoantenna arrays with dielectric metasurfaces. Researchers have shown, that the polarization

conversion efficiency can be drastically increased up to 98% for a broad wavelength regime in the near-infrared region [121]. In addition to the high conversion efficiency, some light shaping applications were shown, such as mimicking a conventional lens, beam steering or holography [122, 123]. However, a challenging aspect in the combination of two-dimensional materials with dielectric metasurfaces is their fabrication process. Since most dielectric metasurfaces are fabricated with the help of etching processes, such fabrication steps might harm monolayers of TMDC, which are placed below the dielectric material in the first place. Therefore, a transfer of monolayers TMDC might be a more practical approach. However, the dimensions of the dielectric metasurfaces, which are much greater than for plasmonic nanoantennas, make a transfer process more difficult than for plasmonic metasurfaces. Here, strain effects play a more important role, which can change the band structure of TMDC's significantly [124]. Nevertheless, further research on hybrid metasurfaces may find ways to overcome such obstacles and achieve an overall enhancement of SHG and the successful encoding of complex phase information into it. Overall, hybrid metasurfaces consisting of nanoantenna arrays and monolayer TMDC's are promising applications for shaping light on small scales and provide a highly attractive field of research.

6. REFERENCES

- [1] Chen, H.-T., A.J. Taylor, and N. Yu, *A Review of Metasurfaces: Physics and Applications*. Reports on Progress in Physics, 2016, **79**(7): Art. no. 076401.
- [2] Li, G., S. Zhang, and T. Zentgraf, *Nonlinear Photonic Metasurfaces*. Nature Reviews Materials, 2017, **2**(5): Art. no. 17010.
- [3] Genevet, P. and F. Capasso, *Holographic Optical Metasurfaces: A Review of Current Progress*. Reports on Progress in Physics, 2015, **78**(2), Art. no. 024401.
- [4] She, A., et al., *Large Area Metalenses: Design, Characterization, and Mass Manufacturing*. Optics Express, 2018, **26**(2): p. 1573-1585.
- [5] Yu, N. and F. Capasso, *Flat Optics with Designer Metasurfaces*. Nature Materials, 2014, **13**(2): p. 139-150.
- [6] Mogensen, K.B. and K. Kneipp, *Size-Dependent Shifts of Plasmon Resonance in Silver Nanoparticle Films Using Controlled Dissolution: Monitoring the Onset of Surface Screening Effects*. The Journal of Physical Chemistry C, 2014, **118**(48): p. 28075-28083.
- [7] Chen, W.T., et al., *A Broadband Achromatic Metalens for Focusing and Imaging in the Visible*. Nature Nanotechnology, 2018, **13**(3): p. 220-226.
- [8] Yu, N., et al., *A Broadband, Background-Free Quarter-Wave Plate Based on Plasmonic Metasurfaces*. Nano Letters, 2012, **12**(12): p. 6328-6333.
- [9] Zheng, G., et al., *Metasurface Holograms Reaching 80% Efficiency*. Nature Nanotechnology, 2015, **10**(4): p. 308-312.

References

- [10] Huang, L., et al., *Broadband Hybrid Holographic Multiplexing with Geometric Metasurfaces*. *Advanced Materials*, 2015, **27**(41): p. 6444-6449.
- [11] Yu, N., et al., *Light Propagation with Phase Discontinuities: Generalized Laws of Reflection and Refraction*. *Science*, 2011, **334**(6054): p. 333-337.
- [12] Ling, X., et al., *Giant Photonic Spin Hall Effect in Momentum Space in a Structured Metamaterial with Spatially Varying Birefringence*. *Light: Science & Applications*, 2015, **4**(5): Art. no. e290.
- [13] Zhang, J., et al., *Plasmonic Metasurfaces with 42.3% Transmission Efficiency in the Visible*. *Light: Science & Applications*, 2019, **8**(1): Art. no. 53.
- [14] Sain, B., C. Meier, and T. Zentgraf, *Nonlinear Optics in All-Dielectric Nanoantennas and Metasurfaces: A Review*. *Advanced Photonics*, 2019, **1**(2): Art. no. 024002.
- [15] Bukasov, R., et al., *Probing the Plasmonic near-Field of Gold Nanocrescent Antennas*. *ACS Nano*, 2010, **4**(11): p. 6639-6650.
- [16] Novotny, L. and N. van Hulst, *Antennas for Light*. *Nature Photonics*, 2011, **5**(2): p. 83-90.
- [17] Mundry, J., et al., *Nonlinear Metasurface Combining Telecom-Range Intersubband Transitions in GaN/AlN Quantum Wells with Resonant Plasmonic Antenna Arrays*. *Optical Materials Express*, 2021, **11**(7): p. 2134-2144.
- [18] Chauvet, N., et al., *Hybrid KTP-Plasmonic Nanostructures for Enhanced Nonlinear Optics at the Nanoscale*. *ACS Photonics*, 2020, **7**(3): p. 665-672.
- [19] Novoselov, K.S., et al., *Two-Dimensional Atomic Crystals*. *Proceedings of the National Academy of Sciences of the United States of America*, 2005, **102**(30): p. 10451-10453.
- [20] Geim, A.K. and K.S. Novoselov, *The Rise of Graphene*. *Nature Materials*, 2007, **6**(3): p. 183-191.
- [21] Mak, K.F. and J. Shan, *Photonics and Optoelectronics of 2D Semiconductor Transition Metal Dichalcogenides*. *Nature Photonics*, 2016, **10**(4): p. 216-226.
- [22] Lee, Y.-H., et al., *Synthesis of Large-Area MoS₂ Atomic Layers with Chemical Vapor Deposition*. *Advanced Materials*, 2012, **24**(17): p. 2320-2325.

-
- [23] Wang, H., et al. *Large-Scale 2D Electronics Based on Single-Layer MoS₂ Grown by Chemical Vapor Deposition*. Institute of Electrical and Electronics Engineers, International Electron Devices Meeting, 2012, Accession Number: 13384002.
- [24] Mak, K.F., et al., *Atomically Thin MoS₂: A New Direct-Gap Semiconductor*. Physical Review Letters, 2010, **105**(13): Art. no. 136805.
- [25] Xie, L.M., *Two-Dimensional Transition Metal Dichalcogenide Alloys: Preparation, Characterization and Applications*. Nanoscale, 2015, **7**(44): p. 18392-18401.
- [26] Li, Y.L., et al., *Measurement of the Optical Dielectric Function of Monolayer Transition-Metal Dichalcogenides: MoS₂, MoSe₂, WS₂, and WSe₂*. Physical Review B, 2014, **90**(20): Art. no. 205422.
- [27] Kern, J., et al., *Nanoantenna-Enhanced Light-Matter Interaction in Atomically Thin WS₂*. ACS Photonics, 2015, **2**(9): p. 1260-1265.
- [28] Wang, S.J., et al., *Coherent Coupling of WS₂ Monolayers with Metallic Photonic Nanostructures at Room Temperature*. Nano Letters, 2016, **16**(7): p. 4368-4374.
- [29] Janisch, C., et al., *Extraordinary Second Harmonic Generation in Tungsten Disulfide Monolayers*. Scientific Reports, 2014, **4**, Art. no. 5530.
- [30] Kumar, N., et al., *Second Harmonic Microscopy of Monolayer MoS₂*. Physical Review B, 2013, **87**(16): Art. no. 161403.
- [31] Chen, J.W., et al., *Tungsten Disulfide-Gold Nanohole Hybrid Metasurfaces for Nonlinear Metalenses in the Visible Region*. Nano Letters, 2018, **18**(2): p. 1344-1350.
- [32] Wen, X.L., et al., *Plasmonic Hot Carriers-Controlled Second Harmonic Generation in WSe₂ Bilayers*. Nano Letters, 2018, **18**(3): p. 1686-1692.
- [33] Han, X., et al., *Harmonic Resonance Enhanced Second-Harmonic Generation in the Monolayer WS₂-Ag Nanocavity*. ACS Photonics, 2020, **7**(3): p. 562-568.
- [34] Arbabi, A. and A. Faraon, *Fundamental Limits of Ultrathin Metasurfaces*. Scientific Reports, 2017, **7**(1): Art. no. 43722.
- [35] Wang, G., et al., *Giant Enhancement of the Optical Second-Harmonic Emission of WSe₂ Monolayers by Laser Excitation at Exciton Resonances*. Physical Review Letters, 2015, **114**(9): Art. no. 097403.

References

- [36] Wang, G., et al., *Exciton States in Monolayer MoSe₂: Impact on Interband Transitions*. 2D Materials, 2015, **2**(4), Art. no. 045005.
- [37] Guo, W.-P., et al., *Chiral Second-Harmonic Generation from Monolayer WS₂/Aluminum Plasmonic Vortex Metalens*. Nano Letters, 2020, **20**(4): p. 2857-2864.
- [38] Hu, G.W., et al., *Coherent Steering of Nonlinear Chiral Valley Photons with a Synthetic Au-WS₂ Metasurface*. Nature Photonics, 2019, **13**(7): p. 467–472.
- [39] Maier, S.A., *Plasmonics : Fundamentals and Applications*. 2006; New York: Springer.
- [40] Novotny, L. and B. Hecht, *Principles of Nano-Optics*. 2006, Cambridge: Cambridge University Press.
- [41] Rakić, A.D., et al., *Optical Properties of Metallic Films for Vertical-Cavity Optoelectronic Devices*. Applied Optics, 1998, **37**(22): p. 5271-5283.
- [42] Johnson, P.B. and R.W. Christy, *Optical Constants of the Noble Metals*. Physical Review B, 1972, **6**(12): p. 4370-4379.
- [43] Haes, A.J., et al., *Plasmonic Materials for Surface-Enhanced Sensing and Spectroscopy*. MRS Bulletin, 2005, **30**(5): p. 368-375.
- [44] Merlein, J., *Lineare Und Nichtlineare Nanoplasmonik*, PhD Thesis, Universität Konstanz, 2008.
- [45] Md Saleh, N. and A. Abdul Aziz, *Simulation of Surface Plasmon Resonance on Different Size of a Single Gold Nanoparticle*. Journal of Physics: Conference Series, 2018, **1083**: Art. no. 012041.
- [46] Mie, G., *Beiträge Zur Optik Trüber Medien, Speziell Kolloidaler Metallösungen*. Annalen der Physik, 1908, **330**(3): p. 377-445.
- [47] Willets, K.A. and R.P. Van Duyne, *Localized Surface Plasmon Resonance Spectroscopy and Sensing*. Annual Review of Physical Chemistry, 2007, **58**(1): p. 267-297.
- [48] Jackson, J.D., *Classical Electrodynamics*. 3rd Edit. 1999, New York, NY: Wiley.
- [49] Franken, P.A., et al., *Generation of Optical Harmonics*. Physical Review Letters, 1961, **7**(4): p. 118-119.
- [50] Boyd, R.W., *Nonlinear Optics, Third Edition*. 2008: Academic Press, Inc.

-
- [51] Li, G.X., et al., *Continuous Control of the Nonlinearity Phase for Harmonic Generations*. *Nature Materials*, 2015, **14**(6): p. 607-612.
- [52] Ramakrishna Matte, H.S.S., et al., *MoS₂ and WS₂ Analogues of Graphene*. *Angewandte Chemie International Edition*, 2010, **49**(24): p. 4059-4062.
- [53] Kolobov, A.V. and J. Tominaga, *Two-Dimensional Transition-Metal Dichalcogenides*. 2016, Switzerland, Springer Series in Materials Science.
- [54] Wilson, J.A. and A.D. Yoffe, *The Transition Metal Dichalcogenides Discussion and Interpretation of the Observed Optical, Electrical and Structural Properties*. *Advances in Physics*, 1969, **18**(73): p. 193-335.
- [55] Agnihotri, O.P., H.K. Sehgal, and A.K. Garg, *Laser Excited Raman Spectra of Gr. VI Semiconducting Compounds*. *Solid State Communications*, 1973, **12**(2): p. 135-138.
- [56] Wang, Q.H., et al., *Electronics and Optoelectronics of Two-Dimensional Transition Metal Dichalcogenides*. *Nature Nanotechnology*, 2012, **7**(11): p. 699-712.
- [57] Newaz, A.K.M., et al., *Electrical Control of Optical Properties of Monolayer MoS₂*. *Solid State Communications*, 2013, **155**: p. 49-52.
- [58] Pospischil, A., M.M. Furchi, and T. Mueller, *Solar-Energy Conversion and Light Emission in an Atomic Monolayer P-N Diode*. *Nature Nanotechnology*, 2014, **9**(4): p. 257-261.
- [59] Ross, J.S., et al., *Electrically Tunable Excitonic Light-Emitting Diodes Based on Monolayer WSe₂ P-N Junctions*. *Nature Nanotechnology*, 2014, **9**(4): p. 268-272.
- [60] Dong, R. and I. Kuljanishvili, *Review Article: Progress in Fabrication of Transition Metal Dichalcogenides Heterostructure Systems*. *Journal of Vacuum Science & Technology B*, 2017, **35**(3): Art. no. 030803.
- [61] Liu, F., et al., *Disassembling 2D van der Waals Crystals into Macroscopic Monolayers and Reassembling into Artificial Lattices*. *Science*, 2020, **367**(6480): p. 903-906.
- [62] He, T., et al., *Synthesis of Large-Area Uniform MoS₂ Films by Substrate-Moving Atmospheric Pressure Chemical Vapor Deposition: From Monolayer to Multilayer*. *2D Materials*, 2019, **6**(2): Art. no. 025030.
- [63] Gutiérrez, H.R., et al., *Extraordinary Room-Temperature Photoluminescence in Triangular WS₂ Monolayers*. *Nano Letters*, 2013, **13**(8): p. 3447-3454.

References

- [64] Cong, C.X., et al., *Synthesis and Optical Properties of Large-Area Single-Crystalline 2D Semiconductor WS₂ Monolayer from Chemical Vapor Deposition*. *Advanced Optical Materials*, 2014, **2**(2): p. 131-136.
- [65] Albe, K. and A. Klein, *Density-Functional-Theory Calculations of Electronic Band Structure of Single-Crystal and Single-Layer WS₂*. *Physical Review B*, 2002, **66**(7): Art. no. 073413.
- [66] Roldán, R., et al., *Electronic Properties of Single-Layer and Multilayer Transition Metal Dichalcogenides MX₂ (M = Mo, W and X = S, Se)*. *Annalen der Physik*, 2014, **526**(9-10): p. 347-357.
- [67] Ermolaev, G.A., et al., *Spectral Ellipsometry of Monolayer Transition Metal Dichalcogenides: Analysis of Excitonic Peaks in Dispersion*. *Journal of Vacuum Science & Technology B*, 2020, **38**(1): Art. no. 014002.
- [68] Jung, G.-H., S. Yoo, and Q.-H. Park, *Measuring the Optical Permittivity of Two-Dimensional Materials without a Priori Knowledge of Electronic Transitions*. *Nanophotonics*, 2019, **8**(2): p. 263-270.
- [69] Hsu, C., et al., *Thickness-Dependent Refractive Index of 1L, 2L, and 3L MoS₂, MoSe₂, WS₂, and WSe₂*. *Advanced Optical Materials*, 2019, **7**(13): Art. no. 1900239.
- [70] Zhao, W., et al., *Evolution of Electronic Structure in Atomically Thin Sheets of WS₂ and WSe₂*. *ACS Nano*, 2013, **7**(1): p. 791-797.
- [71] van der Zande, A.M., et al., *Grains and Grain Boundaries in Highly Crystalline Monolayer Molybdenum Disulphide*. *Nature Materials*, 2013, **12**(6): p. 554-561.
- [72] Trolle, M.L., G. Seifert, and T.G. Pedersen, *Theory of Excitonic Second-Harmonic Generation in Monolayer MoS₂*. *Physical Review B*, 2014, **89**(23): Art. no. 235410.
- [73] Malard, L.M., et al., *Observation of Intense Second Harmonic Generation from MoS₂ Atomic Crystals*. *Physical Review B*, 2013, **87**(20): Art. no. 201401.
- [74] Simon, H.J. and N. Bloembergen, *Second-Harmonic Light Generation in Crystals with Natural Optical Activity*. *Physical Review*, 1968, **171**(3): p. 1104-1114.
- [75] Seyler, K.L., et al., *Electrical Control of Second-Harmonic Generation in a WSe₂ Monolayer Transistor*. *Nature Nanotechnology*, 2015, **10**(5): p. 407-411.
- [76] Ye, W., et al., *Spin and Wavelength Multiplexed Nonlinear Metasurface Holography*. *Nature Communications*, 2016, **7**(1): Art. no. 11930.

-
- [77] Chen, S.M., et al., *Symmetry-Selective Third-Harmonic Generation from Plasmonic Metacrystals*. Physical Review Letters, 2014, **113**(3), Art. no. 033901.
- [78] Czaplicki, R., et al., *Second-Harmonic Generation from Metal Nanoparticles: Resonance Enhancement Versus Particle Geometry*. Nano Letters, 2015, **15**(1): p. 530-534.
- [79] Raygoza-Sánchez, K.Y., et al., *Polarization Dependence of Second Harmonic Generation from Plasmonic Nanoprism Arrays*. Scientific Reports, 2019, **9**(1): Art. no. 11514.
- [80] Spreyer, F., et al., *Influence of Plasmon Resonances and Symmetry Effects on Second Harmonic Generation in Ws₂-Plasmonic Hybrid Metasurfaces*. ACS Nano, 2021, **15**(10), p. 16719-16728.
- [81] Liu, W.J., et al., *Strong Exciton-Plasmon Coupling in MoS₂ Coupled with Plasmonic Lattice*. Nano Letters, 2016, **16**(2): p. 1262-1269.
- [82] Kleemann, M.E., et al., *Strong-Coupling of WSe₂ in Ultra-Compact Plasmonic Nanocavities at Room Temperature*. Nature Communications, 2017, **8**: Art. no. 1296.
- [83] Wang, Z., et al., *Selectively Plasmon-Enhanced Second-Harmonic Generation from Monolayer Tungsten Diselenide on Flexible Substrates*. ACS Nano, 2018, **12**(2): p. 1859-1867.
- [84] Shi, J.W., et al., *Plasmonic Enhancement and Manipulation of Optical Nonlinearity in Monolayer Tungsten Disulfide*. Laser & Photonics Reviews, 2018, **12**(10): Art. no. 1800188.
- [85] Li, Y., et al., *Transversely Divergent Second Harmonic Generation by Surface Plasmon Polaritons on Single Metallic Nanowires*. Nano Letters, 2017, **17**(12): p. 7803-7808.
- [86] Castellanos-Gomez, A., et al., *Deterministic Transfer of Two-Dimensional Materials by All-Dry Viscoelastic Stamping*. 2D Materials, 2014, **1**(1): Art. no. 011002.
- [87] Wang, X., et al., *Near- and Far-Field Effects on the Plasmon Coupling in Gold Nanoparticle Arrays*. The Journal of Physical Chemistry C, 2012, **116**(46): p. 24741-24747.

References

- [88] Xu, T., et al., *Second-Harmonic Emission from Sub-Wavelength Apertures: Effects of Aperture Symmetry and Lattice Arrangement*. Optics Express, 2007, **15**(21): p. 13894-13906.
- [89] Blanchard, R., et al., *Multi-Wavelength Mid-Infrared Plasmonic Antennas with Single Nanoscale Focal Point*. Optics Express, 2011, **19**(22): p. 22113-22124.
- [90] Humphrey, A.D. and W.L. Barnes, *Plasmonic Surface Lattice Resonances on Arrays of Different Lattice Symmetry*. Physical Review B, 2014, **90**(7): Art. no. 075404.
- [91] Xiao, J., et al., *Nonlinear Optical Selection Rule Based on Valley-Exciton Locking in Monolayer WS₂*. Light-Science & Applications, 2015, **4**: Art. no. e366.
- [92] Diaspro, A., et al., *Multi-Photon Excitation Microscopy*. BioMedical Engineering OnLine, 2006, **5**(1): Art. no. 36.
- [93] Denk, W., J.H. Strickler, and W.W. Webb, *Two-Photon Laser Scanning Fluorescence Microscopy*. Science, 1990, **248**(4951): p. 73-76.
- [94] Bar-Elli, O., et al., *Enhanced Third-Harmonic Generation from a Metal/Semiconductor Core/Shell Hybrid Nanostructure*. ACS Nano, 2015, **9**(8): p. 8064-8069.
- [95] Hecht, E., *Optik*. 2018: De Gruyter.
- [96] Chen, W.T., A.Y. Zhu, and F. Capasso, *Flat Optics with Dispersion-Engineered Metasurfaces*. Nature Reviews Materials, 2020, **5**(8): p. 604-620.
- [97] Schlickriede, C., et al., *Imaging through Nonlinear Metalens Using Second Harmonic Generation*. Advanced Materials, 2018, **30**(8): Art. no. 1703843.
- [98] Meinzer, N., W.L. Barnes, and I.R. Hooper, *Plasmonic Meta-Atoms and Metasurfaces*. Nature Photonics, 2014, **8**(12): p. 889-898.
- [99] Chen, S., et al., *Controlling the Phase of Optical Nonlinearity with Plasmonic Metasurfaces*. Nanophotonics, 2018, **7**(6): p. 1013-1024.
- [100] Huang, L., S. Zhang, and T. Zentgraf, *Metasurface Holography: From Fundamentals to Applications*. Nanophotonics, 2018, **7**(6): p. 1169-1190.
- [101] Chen, X.Z., et al., *Dual-Polarity Plasmonic Metalens for Visible Light*. Nature Communications, 2012, **3**: Art. no. 1198.

-
- [102] Spreyer, F., et al., *Second Harmonic Imaging of Plasmonic Pancharatnam-Berry Phase Metasurfaces Coupled to Monolayers of WS₂*. *Nanophotonics*, 2020, **9**(2): p. 351-360.
- [103] Pancharatnam, S., *Generalized Theory of Interference and Its Applications*. *Proceedings of the Indian Academy of Sciences - Section A*, 1956, **44**(6): p. 398-417.
- [104] Mukherjee, B., et al., *Exciton Emission Intensity Modulation of Monolayer MoS₂ Via Au Plasmon Coupling*. *Scientific Reports*, 2017, **7**, Art. no. 41175.
- [105] Pu, Y., et al., *Nonlinear Optical Properties of Core-Shell Nanocavities for Enhanced Second-Harmonic Generation*. *Physical Review Letters*, 2010, **104**(20): Art. no. 207402.
- [106] Linnenbank, H., et al., *Second Harmonic Generation Spectroscopy on Hybrid Plasmonic/Dielectric Nanoantennas*. *Light-Science & Applications*, 2016, **5**: Art. no. 16013.
- [107] Butet, J., et al., *Optical Second Harmonic Generation of Single Metallic Nanoparticles Embedded in a Homogeneous Medium*. *Nano Letters*, 2010, **10**(5): p. 1717-1721.
- [108] Bhagavantam, S. and P. Chandrasekhar, *Harmonic Generation and Selection Rules in Nonlinear Optics*. *Proceedings of the Indian Academy of Sciences - Section A*, 1972, **76**(1): p. 13-20.
- [109] Demtröder, W., *Experimentalphysik 2 : Elektrizität Und Optik*. 6., überarb. u. akt. Aufl. 2013 ed. Springerlink : Bücher. 2013, Berlin, Heidelberg: Springer.
- [110] Trester, S., *Computer-Simulated Fresnel Diffraction Using the Fourier Transform*. *Computing in Science & Engineering*, 1999, **1**(5): p. 77-83.
- [111] Ersoy, O.K., *Diffraction, Fourier Optics and Imaging*. 2006: John Wiley & Sons, Inc.
- [112] Voelz, D.G. *Computational Fourier Optics: A Matlab Tutorial*. 2011.
- [113] Brown, B.R. and A.W. Lohmann, *Complex Spatial Filtering with Binary Masks*. *Applied Optics*, 1966, **5**(6): p. 967-969.
- [114] Jesacher, A., et al., *Near-Perfect Hologram Reconstruction with a Spatial Light Modulator*. *Optics Express*, 2008, **16**(4): p. 2597-2603.

References

- [115] Reichelt, S., et al., *Full-Range, Complex Spatial Light Modulator for Real-Time Holography*. Optics Letters, 2012, **37**(11): p. 1955-1957.
- [116] Huang, L., et al., *Three-Dimensional Optical Holography Using a Plasmonic Metasurface*. Nature Communications, 2013, **4**(1): Art. no. 2808.
- [117] Poland, S.P., et al., *Development of a Doubly Weighted Gerchberg-Saxton Algorithm for Use in Multibeam Imaging Applications*. Optics Letters, 2014, **39**(8): p. 2431-2434.
- [118] Salgado-Remacha, F.J., *Reducing the Variability in Random-Phase Initialized Gerchberg-Saxton Algorithm*. Optics & Laser Technology, 2016, **85**: p. 30-34.
- [119] Ripoll, O., V. Kettunen, and H.P. Herzig, *Review of Iterative Fourier-Transform Algorithms for Beam Shaping Applications*. Optical Engineering, 2004, **43**(11), p. 2549-2556.
- [120] Ni, X., A.V. Kildishev, and V.M. Shalaev, *Metasurface Holograms for Visible Light*. Nature Communications, 2013, **4**(1): Art. no. 2807.
- [121] Yang, Y., et al., *Dielectric Meta-Reflectarray for Broadband Linear Polarization Conversion and Optical Vortex Generation*. Nano Letters, 2014, **14**(3): p. 1394-1399.
- [122] Chantakit, T., et al., *All-Dielectric Silicon Metalens for Two-Dimensional Particle Manipulation in Optical Tweezers*. Photonics Research, 2020, **8**(9): p. 1435-1440.
- [123] Liu, B., et al., *Nonlinear Wavefront Control by Geometric-Phase Dielectric Metasurfaces: Influence of Mode Field and Rotational Symmetry*. Advanced Optical Materials, 2020, **8**(9): Art. no. 1902050.
- [124] Peng, Z., et al., *Strain Engineering of 2D Semiconductors and Graphene: From Strain Fields to Band-Structure Tuning and Photonic Applications*. Light: Science & Applications, 2020, **9**(1): Art. no. 190.

APPENDIX

Scientific Publications

(1) Influence of Plasmon Resonances and Symmetry Effects on Second Harmonic Generation in WS₂-Plasmonic Hybrid Metasurfaces

Florian Spreyer, Claudia Ruppert, Philip Georgi, and Thomas Zentgraf:
ACS Nano (2021), Vol. 15(10), pp. 16719–16728

(2) Nonlinear metasurface combining telecom-range intersubband transitions in GaN/AlN quantum wells with resonant plasmonic antenna arrays

Jan Mundry, Florian Spreyer, Valentin Jmerik, Sergey Ivanov, Thomas Zentgraf, and Markus Betz
Optical Material Express (2021), Vol. 11(7), pp. 2134-2144

(3) Dielectric travelling wave antennas for directional light emission

Till Leuteritz, Henna Farheen, Sigi Qiao, Florian Spreyer, Christian Schlickriede, Thomas Zentgraf, Viktor Myroshnychenko, Jens Förstner, and Stefan Linden
Optics Express (2021), Vol. 29(10), pp. 14694-14704

(4) Second harmonic imaging of plasmonic Pancharatnam-Berry phase metasurfaces coupled to monolayers of WS₂

Florian Spreyer, Ruizhe Zhao, Lingling Huang, and Thomas Zentgraf
Nanophotonics (2020), Vol. 9(2), pp. 351-360

- (5) Submitted and under revision at *ACS Photonics* (2021):
Second-harmonic optical circular dichroism of plasmonic chiral helicoid-III nanoparticles
Florian Spreyer, Jungho Mun, Hyeohn Kim, Ryeong Myeong Kim, Ki Tae Nam, Junsuk Rho, and Thomas Zentgraf

Conference Contributions

- (1) **Symmetry-induced coupling of plasmonic metasurfaces and WS₂**
Florian Spreyer, Feng Shun, Yu Ting, and Thomas Zentgraf
DPG Spring Meeting 2019, Poster
- (2) **Coupling of plasmonic metasurfaces to WS₂**
Florian Spreyer, Feng Shun, Yu Ting, and Thomas Zentgraf
DPG Spring Meeting 2018, Poster

Additional scientific research

As part of the scientific research I have done in the past 5 years at the Paderborn University in the group of Prof. Zentgraf, I investigated the second-harmonic generation in chiral plasmonic nanostructures additionally to the research on hybrid metasurfaces. These nanoparticles provide a different response in the linear and nonlinear regime for left- and right-circular polarized light. This property is called chirality and describes the asymmetry of an object, which is distinguishable from its mirror image. A common example of this property are the hands of a human body, where the left and right hand are distinguishable from each other. The research on these nanoparticles was an intense project, which I worked on parallel to the research on hybrid metasurfaces. However, the investigations on these particles are not part of this thesis, since they cannot be classified as metasurfaces and are further not a part of a hybrid system. Also, the results of this research are still under revision at ACS Photonics and not yet accepted. Nevertheless, the work on these nanoparticles shall be mentioned briefly at this point to honor the cooperation with the group of Prof. Ki Tae Nam from the Seoul National University and group of Prof. Junsuk Rho from the Pohang University of Science and Technology.

ACKNOWLEDGEMENTS

At this point, I would like to thank all of the people without whom this work would not have been possible.

First of all, I would like to give a lot of credits to Prof. Dr. Thomas Zentgraf. He gave me the possibility to participate in his group and do my research at Paderborn University. He supported me in every aspect of my research and gave me thoughtful advice whenever I needed it. It was a great pleasure to learn from his experience in the wide field of optics and it was impressive to observe, that he is so adept in the optics laboratory. At my start of my research, he helped me a lot and showed me the way, how to be a competent scientist. Thank you for believing in me.

I would also like to thank Prof. Dr. Donat As for acting as second reviewer.

I would further like to thank additional scientists, who contributed significantly to my research by sharing their expertise with me: First of all, I would like to thank Christian Schlickriede, Bernhard Reineke, René Geromel and Felicitas Walter for a heartwarming welcome as a new member of the group. Their expertise during the beginning of my research helped me a lot to get a good start in this complex field of research. Moreover, the working atmosphere in the group was very awesome and I enjoyed every second of it. Further, I thank Lingling Huang and Ruizhe Zhao from the Beijing Institute of Technology, who calculated the phase profiles for the implementation of the holographic images into the hybrid metasurfaces. Moreover, I thank Dr. Claudia Ruppert from the TU Dortmund, who invested a lot of time into the transfer of WS₂ monolayers onto quite a lot of plasmonic metasurfaces. In addition, I would like to thank Philip Georgi, who helped me with his great expertise and supported my research by answering my countless questions. I would also like to give him some extra credits for his detailed proof read of my thesis.

In the context of proofreading, I would also like to thank Göran Surmeier for his feedback from a different perspective on the subject.

Acknowledgements

I would also give a special thanks to Daniel Frese, who went from a great colleague to one of my most important friends during my time in the group. Not only I enjoyed the daily coffee in the morning with him, but especially the small chats about every topic in science or life. His companionship helped me through tough times during my research.

Last but not least, I would also like to thank my parents, my sister, my family and my friends, for their support in my life. Hereby, of special importance is my wife Antonia. Thank you for your unconditional love and support you give me on a daily basis. I highly appreciate the times, you stood by my side and made me smile when I needed it the most. I try my best to return the many favors you do me every day.